Results of the 2018 ATLAS sTGC Test Beam
and
Internal Strip Alignment of sTGC Detectors

by

Evan Michael Carlson
B.Sc., Pacific University, 2017

A Thesis Submitted in Partial Fulfillment of the
Requirements for the Degree of

MASTER OF SCIENCE

in the Department of Physics and Astronomy

Results of the 2018 ATLAS sTGC Test Beam
and
Internal Strip Alignment of sTGC Detectors

by

Evan Michael Carlson
B.Sc., Pacific University, 2017

Supervisory Committee

Dr. Isabel Trigger, Co-Supervisor
(Department of Physics and Astronomy & TRIUMF)

Dr. Robert Kowalewski, Co-Supervisor
(Department of Physics and Astronomy)

Dr. Richard Keeler, Departmental Member
(Department of Physics and Astronomy)

Supervisory Committee

Dr. Isabel Trigger, Co-Supervisor
(Department of Physics and Astronomy & TRIUMF)

Dr. Robert Kowalewski, Co-Supervisor
(Department of Physics and Astronomy)

Dr. Richard Keeler, Departmental Member
(Department of Physics and Astronomy)

ABSTRACT

Over the course of the next ten years, the LHC will undergo upgrades that will more than triple its current luminosity. This increase in luminosity will put greater demands on the ATLAS trigger system. To meet these demands, the Small Wheels of the muon spectrometer will be replaced with the New Small Wheels (NSWs) during Long Shutdown 2. The NSWs employ two gaseous detector technologies - small-strip Thin Gap Chambers (sTGCs) and Micromegas. To characterize the sTGCs, a series of test beams were conducted on a production sTGC module at the H8 beamline of CERN's Super Proton Synchrotron. The setup and results of the test beams are presented, and it has been found that the detector meets the performance requirements of the NSW for efficiency and multiplicity at several operating voltages.

To meet the performance requirements of the NSW, the positions of the detector elements must be precisely known. Quality control measurements were made during construction of the sTGC strip cathode boards to allow for the reconstruction of individual strip positions. A transformation from the nominal strip geometry to the as-built geometry is derived based on the QC measurements. This transformation was tested against microscope and cosmic ray misalignment measurements. The as-built predictions agree well with the misalignment measurements, demonstrating the ability to reconstruct the strip positions from the QC measurements.

Contents

List of Tables

List of Figures

STATEMENT OF ORIGINALITY AND CONTRIBUTIONS OF CO-AUTHORS

The results that are presented in this thesis were obtained in collaboration with several groups of individuals. The test beam described in Chapter 4 was carried out by members of the ATLAS sTGC group, including myself. The results presented in Chapter 5 are strictly the results of my own analysis of the data collected during the test beam. The as-built transformation derived in Chapter 6 was derived by me. The microscope measurements described in Chapter 6 were carried out by the ATLAS group at Carleton University. The cosmic ray test setup described in Chapter 7 was developed and operated by the McGill University ATLAS group, and the misalignment measurements extracted from the cosmic ray data were obtained by Benoit Lefebvre. The analysis of the misalignment data presented in Chapter 8 is my own analysis that was developed to compare my as-built misalignment predictions to the microscope and cosmic ray misalignment measurements.

ACKNOWLEDGEMENTS

The completion of this thesis wouldn't have been possible without the help of the amazing group of people that I have in my life. First and foremost, I need to thank my supervisor Dr. Isabel Trigger. She has been an unending source of advice, encouragement and support from day one. I have learned so much from her throughout the course of this program, and I look forward to continuing our work together through my PhD. I'd also like to thank my co-supervisor Dr. Bob Kowalewski. He was an incredible help in getting settled in at UVic, and he's given me excellent guidance throughout my time here.

I'd also like to extend my gratitude to the faculty and staff of the UVic Physics and Astronomy department. In particular, the UVic ATLAS group has been incredibly supportive of me and my work. Many thanks go to the TRIUMF ATLAS group for their constant support and guidance. My work has benefitted greatly from their input.

The test beam crew at CERN deserves a special thanks - Gerardo Vásquez, Dennis Pudzha, Alam Toro Salas, Yan Benhammou, Lia Formenti, Paris Franz, Matt Gareau, and many others. Thanks for being wonderful teachers and an incredible family during my time at CERN.

The ATLAS sTGC Group has consistently been a pleasure to work with. Jesse Heilman has been a huge help in understanding both the construction process and the microscope alignment pictures. The comparisons to the cosmic ray alignment measurements presented in this thesis are a result of a collaboration with Benoit Lefebvre and the sTGC group at McGill University. I can't thank Benoit enough for his guidance and insight into this project.

I am grateful for the fantastic friends that I have made both at UVic and at TRIUMF. They helped to keep me sane and always provided valuable insight on the challenges I was facing. This process would have been half as enjoyable without their company.

A heartfelt thank you goes to my family, who has given me all of the love and support that a person could ever ask for. They have been exceedingly selfless in giving me everything that I need to succeed in life. I couldn't ask for a better family, and I am truly blessed by their presence in my life.

Finally, my deepest thanks go to my fiancée, Katie Wagner. She has been an

endless source of love, joy, laughter and wisdom since the day we met. Whether it was words of encouragement at the end of a long day or spamming my phone with pictures of puppies, she always knows how to bring a smile to my face when nothing else can. Thank you for all of the blessings that you bring to my life. I can't wait to start our life together in August!

DEDICATION

For Katelyn, my wonderful fiancée.

Chapter 1

Introduction

The field of particle physics is concerned with the study of the properties of fundamental particles and their interactions. The Standard Model of particle physics, a theory developed over the last 60 years, has been incredibly successful in providing a highly accurate description of elementary particles, their properties and their interactions. It consists of 12 spin-$\frac{1}{2}$ fermions, each with a corresponding antiparticle, along with 5 integer spin bosons. The final ingredient of the Standard Model, the Higgs Boson, was discovered in 2012. With the discovery of the Higgs boson, the Standard Model is now complete. Over the years, the Standard Model has provided phenomenal predictive power for the field and has withstood rigorous precision testing.

Despite the incredible success of the Standard Model, there are questions in particle physics that remain unanswered that the theory provides no explanation for. Astronomical observations have confirmed that more than 75% of the matter in the universe must be dark matter, consisting of some type of particle that does not interact with the electromagnetic force. Although there are particles in the Standard Model that do not interact via the electromagnetic force, experimental observations have ruled out the possibility that dark matter is made up of these particles. If dark matter does consist of elementary particles, then it must be a particle that exists outside of the Standard Model. Another open question that is unanswered by the Standard Model pertains to the prevalence of matter and antimatter in the universe. Experimental evidence suggests that the visible matter of the universe is overwhelmingly composed of regular matter, not antimatter. In the Standard Model, matter and antimatter particles are almost always produced in pairs. Though a small asymmetry between matter and antimatter can be produced by charge-parity (CP) symmetry violation in the Standard Model, the amount of CP violation predicted by current

measurements in the Standard Model is insufficient to explain the observed level of asymmetry.

In an attempt to provide answers for questions such as these, experimental particle physicists around the world are employing state of the art particle detectors and accelerators to probe the conditions of the early universe. The Large Hadron Collider (LHC) at CERN is the highest energy particle accelerator in the world. It currently accelerates protons to an energy of 6.5 TeV per beam, and collides them at four locations around its roughly circular path. The ATLAS experiment is one of two general purpose detectors collecting data at the LHC. ATLAS was built with many goals in mind, but the primary goal was to discover the Higgs boson. It succeeded in this endeavor in 2012 along with the CMS collaboration. Since then, the detector has been collecting data to make precision measurements of the Standard Model and to search for new particles. In order to improve the performance of the LHC and its experiments, the collider shut down at the end of 2018 and will remain off until 2021. During this shutdown, the LHC will undergo extensive maintenance and upgrades to allow it to collide a greater number of protons. It is also possible that the beam energy will be upgraded to 7 TeV per beam following the shutdown.

Because of the huge volume of data produced inside ATLAS, it is impossible to record it all. ATLAS employs a trigger system to help filter the data down to a more manageable size. Most interactions that occur within ATLAS are common processes that have been thoroughly studied, and only a small fraction of these events need to be recorded. The trigger system works to identify rare processes by searching for particular signatures, such as decays to a pair of high-energy muons. Following the shutdown, the number of interactions occurring within ATLAS will be increasing by a factor of 2. This increase in data will put a great stress on the performance of the trigger system.

In order to cope with the increased data volume, ATLAS will undergo major upgrades during the shutdown. The primary upgrade during this period are the New Small Wheels (NSWs), a replacement for the original Small Wheels in the muon spectrometer's end-cap region. The NSWs will help to alleviate the stress placed on the trigger system from the increase in luminosity by providing fast precision tracking in the Small Wheel trigger chambers. Two technologies have been chosen to be implemented into the NSW upgrade. The primary trigger chambers of the NSWs will be composed of small-strip Thin Gap Chambers (sTGCs). These detectors are an improvement of the current ATLAS Thin Gap Chambers. An sTGC is a type

of multiwire proportional chamber consisting of a plane of high voltage wires strung between two cathode planes. One of the cathode planes is segmented into pads and the other is segmented into strips with a pitch of 3.2 mm.

Before the NSWs are installed into ATLAS, it is important to fully characterize the performance of the detectors. In particular, measurements of properties such as the efficiency, position resolution and noise of the detector are critical to understanding how the detector will perform inside ATLAS. To this end, several beam tests have been conducted on sTGCs to make these measurements. One such beam test took place at CERN from August to October of 2018. I was part of the team that conducted this beam test, and was heavily involved in the analysis of the data. Some of the results of the beam test are presented in this thesis.

Another important aspect of the NSW that is critical to its success is the detector alignment. The full NSW is approximately 10 m in diameter. In order to provide the precision tracking required by the trigger system, it is necessary to know the positions of the detector elements to a precision on the order of tens of microns. In particular, the positions of the strips of the sTGC detectors must be accurately reconstructed. Because the strip cathode boards cannot be constructed perfectly, the positions of the individual strips must be reconstructed in software. Quality control measurements of the cathode boards have been done to allow for this reconstruction.

The focus of this thesis is twofold. The first focus is on the setup and results of the fall 2018 sTGC test beam, and the second is on the software reconstruction of the sTGC strip positions based on the quality control measurements of the cathode boards. The position predictions of the software have been compared to measurements of the strip alignment taken with both microscopes and cosmic rays.

Chapter 2 provides a general description of the ATLAS detector, and Chapter 3 describes the purpose, function and performance goals of the New Small Wheel. Chapter 4 outlines the experimental setup of the beam tests, and Chapter 5 presents the results of those tests. Chapter 6 focuses on the as-built reconstruction of the sTGC strip positions and explains the microscope alignment measurements. Chapter 7 describes the cosmic ray data taking procedure and details how alignment measurements are made with cosmic rays. The results of the comparison between the as-built predictions and the microscope and cosmic ray alignment measurements are presented in Chapter 8. The final conclusions of this thesis are given in Chapter 9.

Chapter 2

The LHC and ATLAS

The European Organization for Nuclear Research, known as CERN, is a physics research organization located just outside of Geneva, Switzerland, on the French-Swiss border. It is currently the home of numerous particle and nuclear physics experiments, including the ATLAS detector. Established in 1954, the laboratory was originally created to study atomic nuclei, but its focus quickly shifted to the investigation of subatomic particles and their interactions. CERN currently has 23 member states, as well as three other nations with Observer status [1]. Over the course of its existence, CERN has made numerous discoveries and contributions to particle physics, including the discovery of weak neutral currents in 1973 by the Gargamelle collaboration, as well as the discovery of the $W^{\pm}$ and Z bosons in 1983. Researchers at CERN are also credited with the discovery of direct charge-parity (CP) violation in 1999 [2]. More recently, the ATLAS and CMS collaborations at CERN discovered a particle of mass 125 GeV in 2012 that has properties consistent with the Higgs boson, first theorized in 1964 by Peter Higgs. Peter Higgs and François Englert were awarded the 2013 Nobel Prize in Physics for this discovery. Current physics goals for CERN include searches for physics beyond the Standard Model, precision measurements of Standard Model parameters, and development of new accelerator techniques [2].

2.1 The Large Hadron Collider

CERN currently operates an accelerator complex consisting of ten accelerators and one decelerator, providing numerous experiments with different particles of varying energies. The highest energy provided is in the Large Hadron Collider (LHC), a 27 km

synchrotron accelerator that straddles the border between France and Switzerland. The LHC occupies the tunnel that previously housed the Large Electron-Positron Collider (LEP). It produces two 6.5 TeV proton beams and delivers them to seven experiments - ATLAS, CMS, ALICE, LHCb, MoEDAL, TOTEM and LHCf. These experiments are located at four interaction points around the ring of the accelerator. The LHC is the end of a chain of proton accelerators. The full accelerator complex at CERN is shown in Figure 2.1. The accelerator chain for the LHC consists of:

1. **Linac 2**, a linear accelerator that takes ionized hydrogen (protons) from rest to an energy of 50 MeV. Linac 2 will be replaced by Linac 4 in 2021.

2. The **Proton Synchrotron Booster**, which takes the protons from Linac 2 and accelerates them up to an energy of 1.4 GeV with a velocity of 89.8% of the speed of light.

3. The **Proton Synchrotron**, which accepts beams from the Proton Synchrotron Booster and accelerates them to an energy of 25 GeV.

4. The **Super Proton Synchrotron (SPS)**, a 7 km accelerator that pushes beams from the Proton Synchrotron up to an energy of 450 GeV. Aside from feeding the LHC, beams from the SPS serve many experiments, including the NA62, COMPASS and AWAKE experiments. Beams from the SPS also service the test beam areas located in CERN's North Area.

The LHC is fed proton bunches from this chain of accelerators [3]. Upon entering the accelerator, the proton bunches are accelerated by strong electric fields in a radiofrequency cavity. Each time the protons pass through one of the eight cavities, they pick up more energy. The beams are kept in their roughly circular path by superconducting dipole electromagnets made of niobium-titanium (Nb-Ti). With a current of 11.08 kA, the magnets have a maximum field of 8.3 Tesla, but do not operate at their maximum field until the beam reaches its maximum energy [4]. When the protons are originally injected from the SPS, the currents in the magnets tune the magnetic field to a much smaller value, in order to keep the particles on their precise path. As the protons pick up energy from the electric fields, the magnets increase their current so that the magnetic fields provide the precise amount of bending needed for the beam to maintain its path.

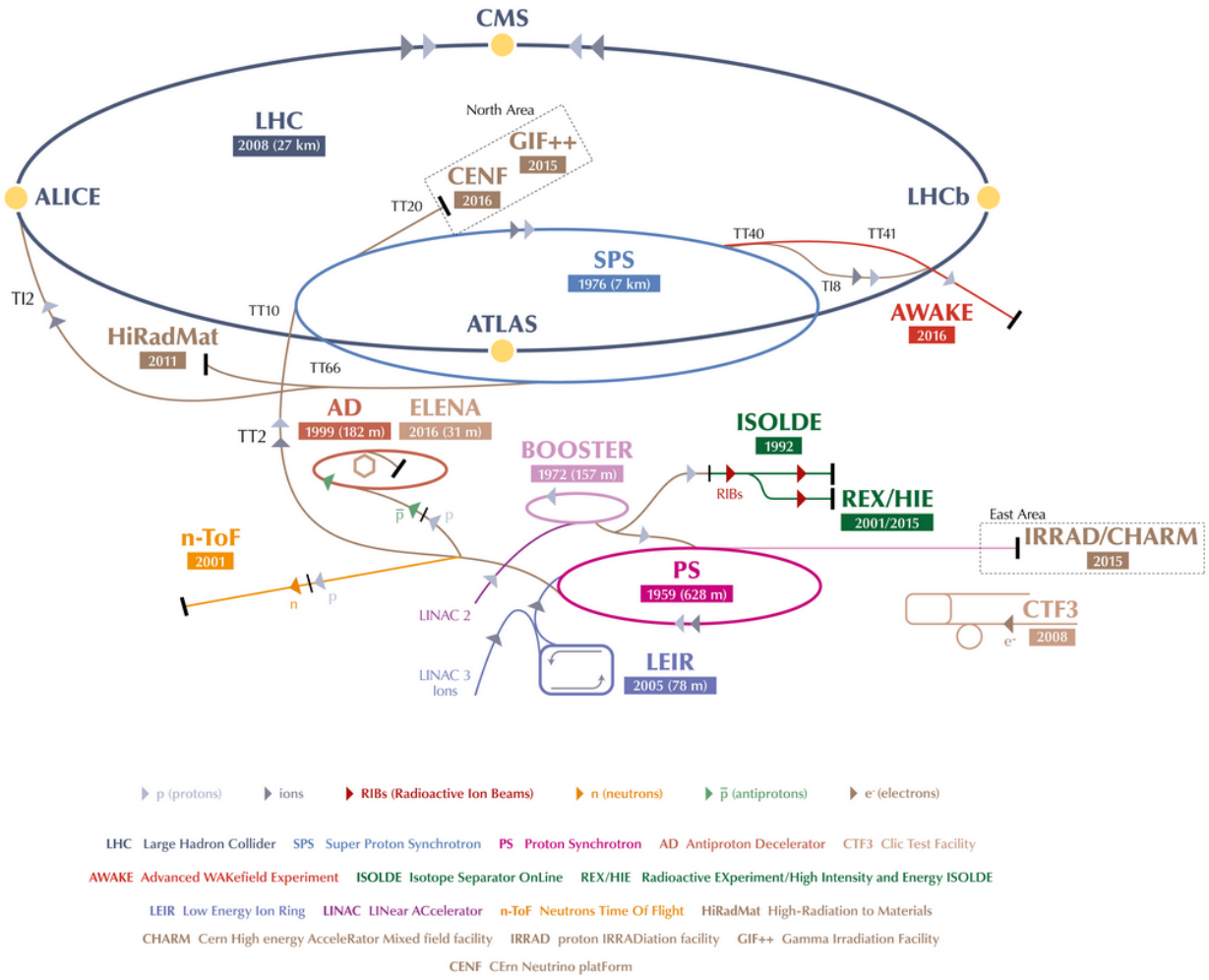

Figure 2.1: The accelerator complex at CERN [5]. The path for protons entering the LHC starts with Linac 2 (magenta) and moves through the Proton Synchrotron Booster (light pink), the Proton Synchrotron (dark pink), and the Super Proton Synchrotron (light blue).

2.2 The ATLAS Detector

The ATLAS detector is a multipurpose particle detector located at Point 1 of the LHC. ATLAS was designed to detect and reconstruct the particle collisions that the LHC produces. To do this, it needs to be able to quickly and accurately measure the energies, momenta, and trajectories of the particles produced in the interactions. Several different detector components are used to accomplish this goal, each specializing in different particle types or aspects of the measurement process. The main components of ATLAS are the inner detector, the calorimeters, the magnet system, and the muon spectrometer. A cross section of the detector illustrated in Figure 2.2 shows how different portions of the detector are specialized to detect specific particles. Through the cooperation of these components, ATLAS is able to pursue a wide variety of physics goals, such as searches for Supersymmetry, dark matter, and new exotic particles, as well as performing precision measurements of existing Standard Model particles and parameters [6].

Located in a cavern nearly 100 m underground, ATLAS is a massive detector weighing approximately 7000 tonnes with a length of 44 m and a diameter of 25 m. The detector is assembled in roughly cylindrical layers around the interaction point (IP) in the center. ATLAS is generally divided into two regions known as the barrel and the end-caps. The barrel consists of cylindrical layers of detectors with the beam running along the axis of the cylinder, and the end-caps are the disk shaped structures on the ends of the barrel that detect particles at smaller angles from the beamline. For each component of the detector, there are both barrel and end-cap stations such that ATLAS has complete coverage for all stable particle types except neutrinos [6]. A diagram showing the layout of the ATLAS detector and its components is shown in Figure 2.3.

The IP serves as the origin of the ATLAS coordinate systems. A cylindrical coordinate system is used to describe the geometry of the detector and a spherical coordinate system is used in the analysis of ATLAS data. For the cylindrical coordinate system, the z-axis is defined by the beamline. Perpendicular to the beamline is the xy-plane, also known as the transverse plane, with the positive x-axis pointing towards the center of the LHC ring and the positive y-axis pointing upward towards the surface of the Earth. The radius of a point from the IP is defined in cylindrical coordinates as $R = \sqrt{x^2 + y^2}$. The azimuthal angle, ϕ, is measured from the x-axis. It measures the angle in the transverse plane. This cylindrical coordinate system is

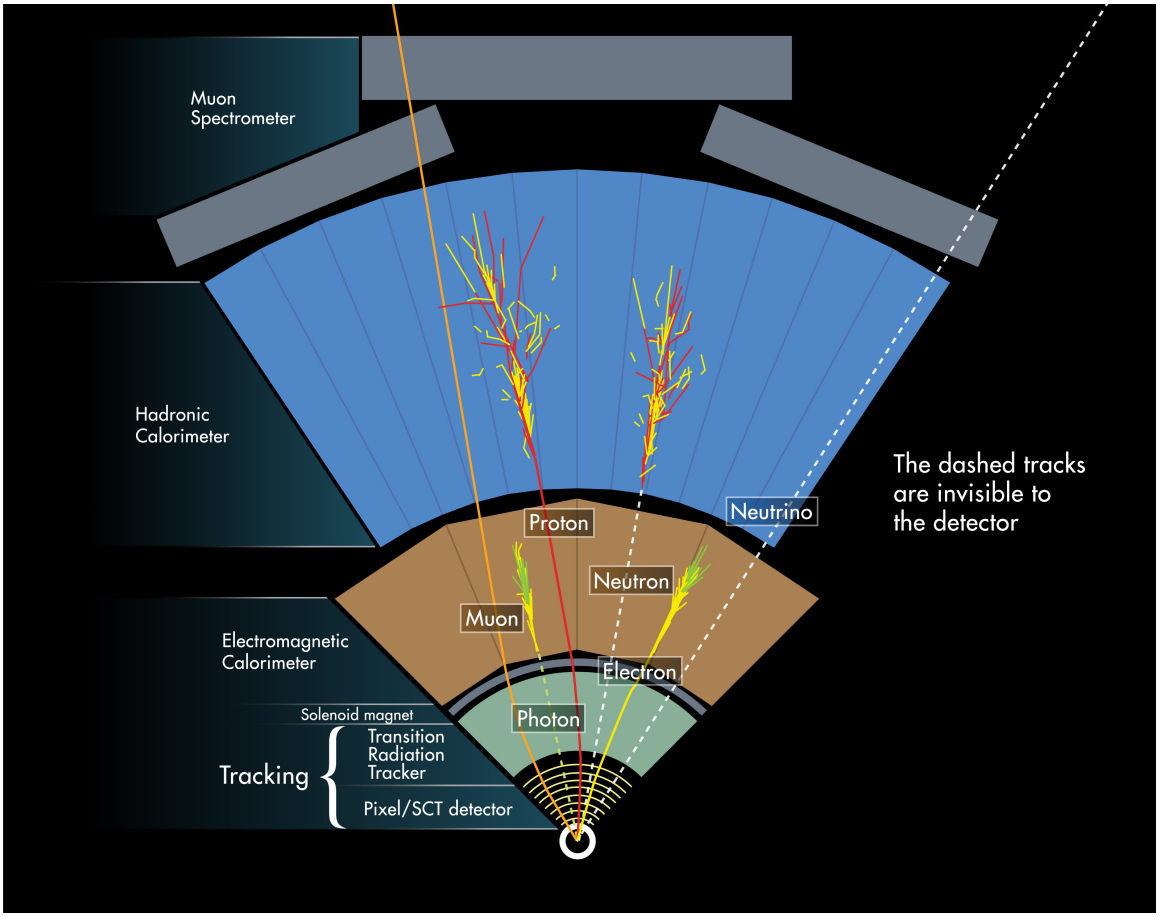

Figure 2.2: A diagram of the ATLAS barrel cross-section showing how different particles are detected [7]. Each component of the detector is uniquely designed to be proficient in detecting and measuring certain types of particles.

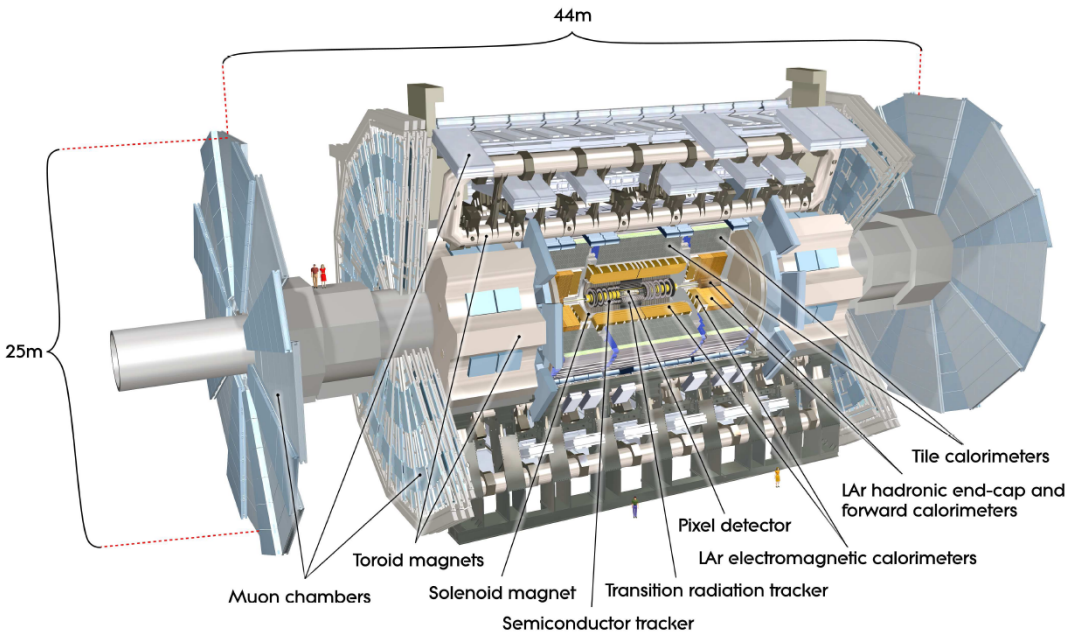

Figure 2.3: A cutaway diagram of the ATLAS detector [6]. The different components of the detector are labeled.

used to describe the positions of detector elements within ATLAS.

The spherical coordinates that ATLAS employs in analyses utilize two angles, θ and ϕ. The azimuthal angle ϕ is defined in the same way as for the cylindrical coordinate system. The polar angle θ measures the angle from the beam axis. In practice, however, another parameter called the pseudorapidity η is used instead of θ, with η defined as

$$\eta \equiv -\ln[\tan\frac{\theta}{2}]. \tag{2.1}$$

By this definition η is zero when the polar angle is 90°, and tends to $+\infty$ as θ goes to 0 and to $-\infty$ as θ goes to 180°. ATLAS utilizes η instead of the polar angle θ because particle production is approximately uniform with respect to η. Figure 2.4 shows both the cylindrical and spherical coordinate systems used by ATLAS.

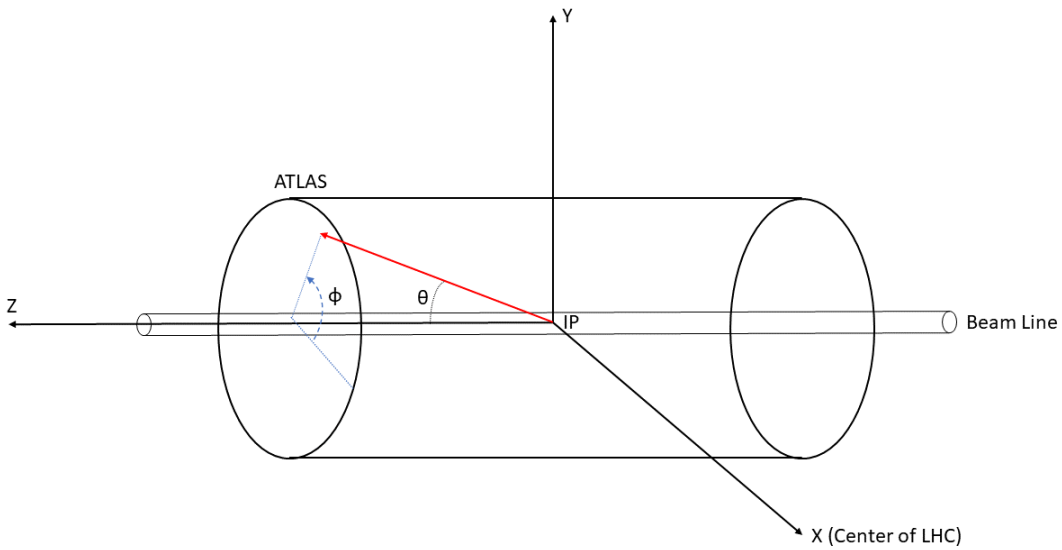

Figure 2.4: A diagram showing the coordinate systems utilized by ATLAS [8].

The collisions happening between particles at the LHC are not between elementary particles. The protons accelerated by the LHC are composite particles composed of quarks and gluons. When two protons interact inside ATLAS, it is not truly the protons interacting, but instead the constituent quarks and gluons. Because protons are composite, each particle that comprises a proton carries some fraction of the total proton momentum. This fraction is not fixed, so when two protons collide

inside ATLAS, we cannot be sure about the initial momentum along the beamline of the interacting particles. However, it is known that the colliding particles will have approximately zero momentum in the transverse plane. Knowing this, we can use this as a constraint to be able to identify missing momentum and energy in the transverse plane.

2.3 The Inner Detector

The inner detector is the innermost component of ATLAS and is the first to observe the products of the collisions generated by the LHC. It resides inside ATLAS' solenoid magnet, and has a magnetic field of 2 Tesla pointing along the beam axis. It spans a length of 6.2 m, has a diameter of 2.1 m and provides coverage in the range $|\eta|< 2.5$. The primary purpose of the inner detector is to measure tracks and determine the momenta of charged particles passing through it, as well as to locate the vertices of interactions. Tracks deposited by charged particles in the inner detector will curve due to the magnetic field, and particles of opposite charge will curve in opposite directions, allowing the particle's charge to be determined. It also provides a means of differentiating between particles with the same charge. The inner detector is divided into three sub-detectors: the Pixel Detector, the Semiconductor Tracker (SCT), and the Transition Radiation Tracker (TRT) [6]. The full structure of the inner detector is shown in Figure 2.5.

2.3.1 Pixel Detectors

The innermost component of the inner detector is the Pixel Detector. The Pixel Detector is made of silicon wafers. When a charged particle passes through the silicon, ionization occurs in the silicon and a small current is produced and measured. The Pixel Detector extends to a radius of 12 cm from the interaction point and extends 65 cm along the beam axis in both directions. It consists of four concentric barrels around the beam axis and three disks orthogonal to the beam axis on each side of the IP. Each silicon pixel has an area of 50 μm by 400 μm, with the small size of the pixel allowing for high resolution tracking in both the barrel and disk regions. The Pixel Detector has a total of 80 million channels, which when combined with the high individual resolution of the pixels, allows for the Pixel Detector system to accurately identify particle tracks and vertices. Furthermore, the precision of the Pixel Detector

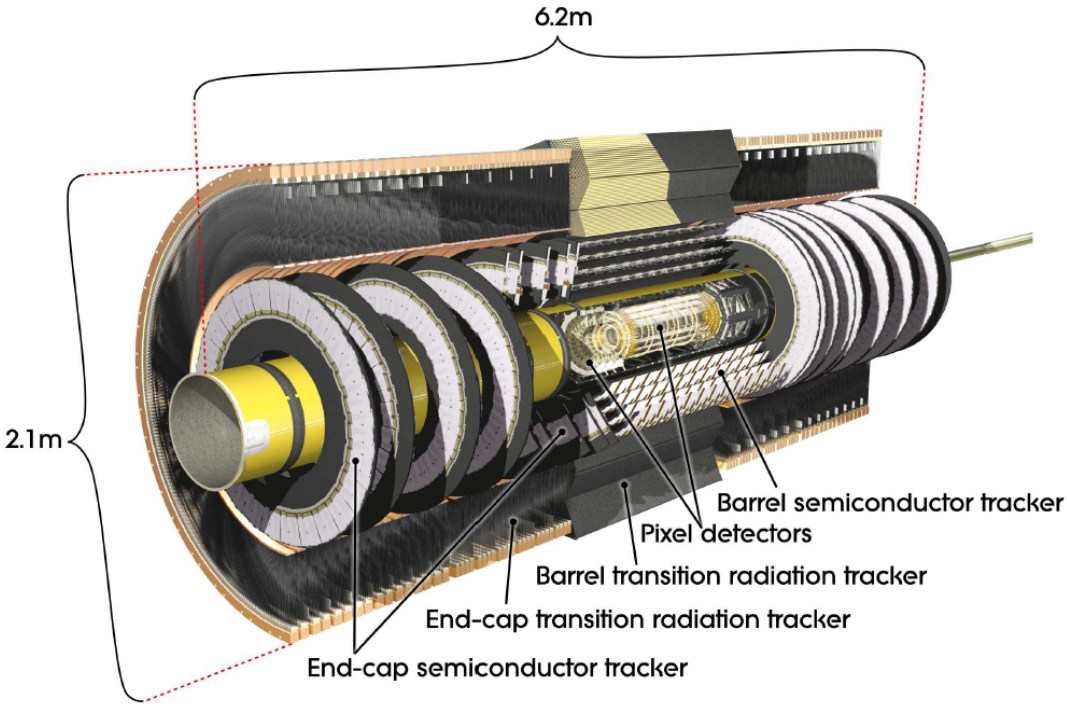

Figure 2.5: A cutaway diagram of the ATLAS inner detector showing its structure [6].

also can be used to identify secondary vertices, which are the decay points of particles produced in the primary interaction. This is very important in the identification of short-lived particles such as B-hadrons [6].

2.3.2 Semiconductor Tracker

Outside of the Pixel Detector lies the SCT. The SCT consists of 4808 two-sided silicon strip modules, with each side containing 780 silicon strips with a width of 80 μm. This combines for a total of approximately 6.3 million readout channels. This signal allows the detector to measure the position of the particle to a resolution of 17 μm in the R- and ϕ-coordinates. These strips are arranged into 4 concentric cylinders in the barrel regions, and into 9 disks for each end-cap. This can be seen in Figure 2.5. For an individual strip module there are strips on each side of the module. The strips on one side of the module are inclined at an angle of 40 mrad relative to the other side. This small angle of inclination allows the strip detector to provide a second coordinate measurement. For the barrel, this angle allows for the measurement of the z-coordinate, and in the end-caps it provides the radial measurement. An average charged particle leaving the interaction point should produce eight hits in the SCT, allowing for precision measurements of both the vertex of the particle and its momentum [6].

2.3.3 Transition Radiation Tracker

The Transition Radiation Tracker is the outermost component of the inner detector and covers the range $|\eta|< 2.0$. It consists of 320000 radial straw tubes in the end-caps and 50000 straw tubes parallel to the beamline in the barrel. Each cylindrical straw has a gold-plated tungsten wire strung along the axis that is held at 1530 V relative to the walls of the tube. These tubes are filled with a $Xe/CO_2/O_2$ gas mixture such that the charged particles passing through can ionize the gas, allowing them to function in the same manner as drift tubes. The tubes in the barrel region provide R - ϕ measurements and the end-cap tubes provide z - ϕ measurements. Transition radiation generated by the passing particles contributes to ATLAS' ability to properly identify particles, as particles of similar momenta but different masses will emit very different transition radiation that can be measured by the TRT. In particular, the ATLAS TRT provides excellent discrimination between $e^{\pm}$ and $\pi^{\pm}$ [6]. Figure 2.6 shows the path a particle will take through the barrel section of the inner detector.

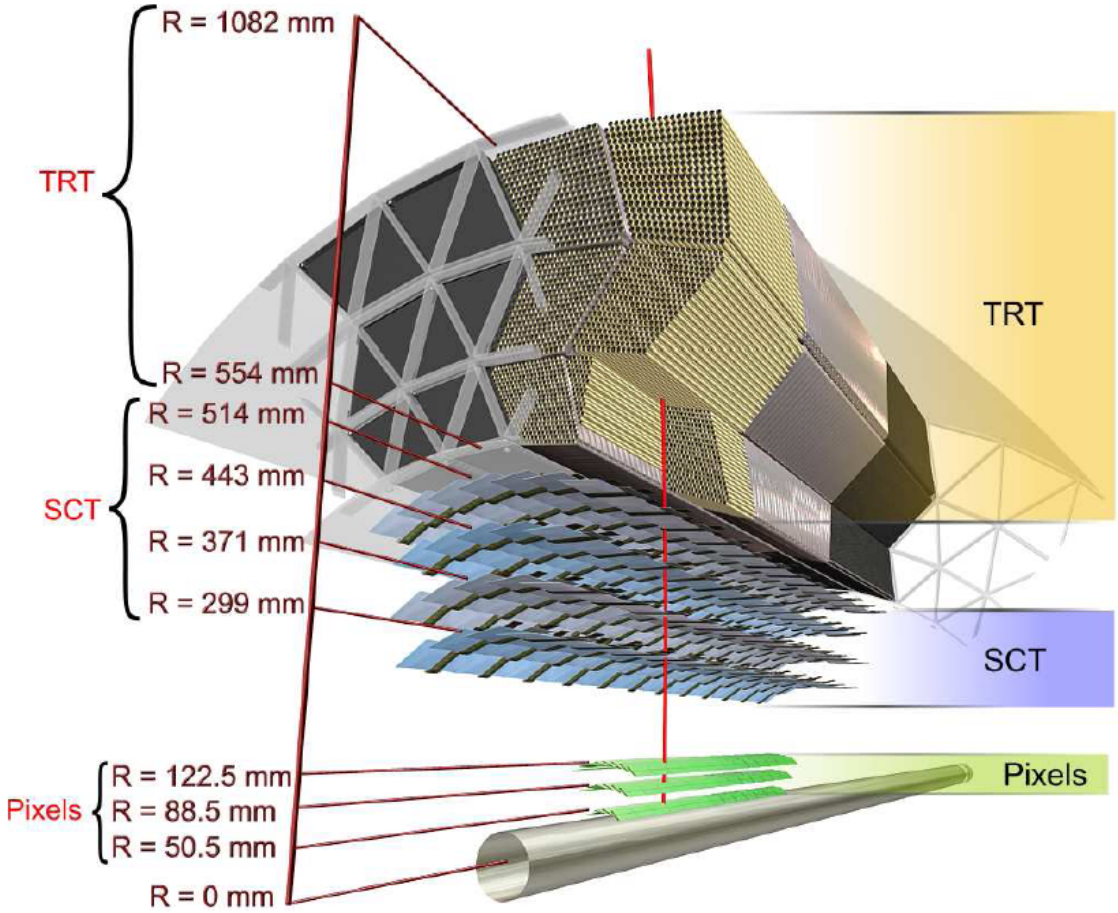

Figure 2.6: A diagram of a particle traversing the barrel region of the inner detector [6]. The particle will pass through four layers of pixels, four layers of SCT (8 strips), and the TRT. An additional layer of pixels was added in 2014 at R = 33 mm after a new smaller radius beam-pipe replaced the original beam-pipe [9].

2.4 Calorimetry

The second major component of ATLAS is the calorimetry system. Located outside of the solenoid magnet, the ATLAS calorimeters are designed to absorb and measure the energy of hadrons, electrons and photons. The calorimeter destroys the particles that it measures in the process, converting them to light, energy, and other particles. With over 22 radiation lengths of material in the electromagnetic calorimeter and more than 9 interaction lengths in the hadronic calorimeter, almost all Standard Model particles except neutrinos and muons are prevented from passing through the muon spectrometer [6].

Calorimeters work by forcing the passing particles to interact. A series of successive interactions produces a phenomenon called a shower, causing the initial particle to deposit all of its energy within the calorimeters and stop completely. The ATLAS calorimeters are what are known as "sampling" calorimeters, meaning that they do not consist entirely of the active detector elements. Instead, they consist of alternating layers of active material and dense absorbers. The active material is able to detect the deposited energy and produce a signal, but is not efficient at actually initiating and containing the showers. The dense absorber layers are interleaved with the active layers to initiate the necessary particle showers. The drawback to this system is that some of the energy of the incident particle is deposited into the absorber layers and cannot be measured. However, the total energy can be accurately estimated based on the energy detected by the active layers [6].

The ATLAS calorimeters can be classified in two ways: by purpose or by technology. Classifying by purpose, the two ATLAS calorimeters are the Electromagnetic Calorimeter (ECAL) and the Hadronic Calorimeter (HCAL). The ECAL is designed to measure the energy of particles that primarily interact through the electromagnetic force, namely photons and electrons, while the HCAL measures the energy of particles that interact through the strong force, such as protons and neutrons. However, it is perhaps easier to separate the ATLAS calorimetry system by technology. The two technologies that make up the calorimeters are the Tile Calorimeter (TileCal) and the Liquid Argon (LAr) Calorimeter [6].

The TileCal is located radially outward from the LAr calorimeter and constructed in three sections - a barrel covering the region $|\eta| < 1.0$ and two extended barrels for the region $0.8 < |\eta| < 1.7$. The active media of the TileCal is a collection of 3mm thick plastic scintillating tiles connected to wavelength shifting fibers which serve

as readout. These plastic tiles alternate layers with thick iron plates. The ratio of scintillator to iron is 1 to 4.7, which yields an appropriate thickness to prevent almost all hadrons from entering the muon system [10].

The LAr Calorimeter can be subdivided into four sections - the barrel, the electromagnetic end-cap, the hadronic end-cap, and the forward calorimeter. In all four sections, liquid argon cooled to -184.5° C serves as the active medium. In the barrel, covering the region $|\eta|< 1.475$, the liquid argon is in between layers of lead absorbers that are bent in an accordion geometry. The accordion structure ensures that there are no gaps present in the ϕ-coordinate. Electrodes on the accordion structures pick up the resulting ionization from passing particles and produce signals. In the region $1.375 < |\eta|< 3.2$, the electromagnetic end-cap measures the energies of electromagnetic particles with a similar lead accordion design to the electromagnetic barrel calorimeter. The disk-shaped hadronic end-cap is located beyond the electromagnetic end-cap, and is made up of copper absorption layers with active liquid argon layers filling the gaps between them. Each hadronic end-cap consists of two wheels, with a total of 40 liquid argon readout gaps [11].

The Forward Calorimeter (FCal) is the final component of the LAr Calorimeter. It was designed to be able to perform in the high rate environment of the forward regions of the detector, in the range $3.1 < |\eta|< 4.9$. To accomplish this, the FCal consists of three modules - one for electromagnetic calorimetry and two for hadronic calorimetry. Each module consists of a wheel of metal - copper for the electromagnetic module and tungsten for the hadronic modules - with tubes running through it. Suspended in these tubes are anode rods with a gap of liquid argon between the wall of the tube and the rod. With the rod held at high voltage, particles passing through ionize the liquid argon and the resulting charge drifts to the rod and is detected as a signal [12]. A full diagram of the ATLAS calorimetry system is shown in Figure 2.7.

2.5 Magnets

The ATLAS magnet system is a collection of superconducting magnets that provide the strong magnetic fields necessary to bend the trajectories of high energy particles. It can be divided into three parts - the central solenoid, the barrel toroid and the end-cap toroids. All three components of the system utilize thousands of coils of superconducting Nb-Ti to generate the fields. To maintain the superconducting properties of the Nb-Ti, the coils must be continuously cooled to a temperature of

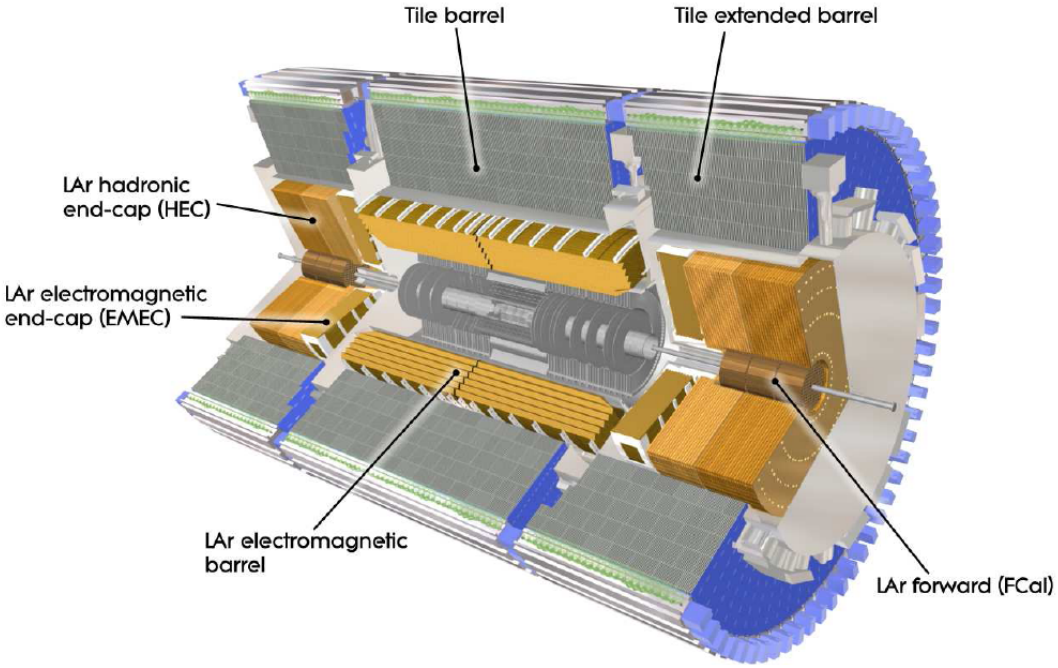

Figure 2.7: A diagram of the ATLAS calorimeter system [6].

4.5 K [6].

The central solenoid is the innermost piece of the magnet system. It fully contains the inner detector but is contained within the electromagnetic calorimeter. Because the calorimeter is outside of the solenoid, it was designed to be as transparent as possible so that the number of particles interacting with the solenoid is kept to a minimum. A particle passing through at normal incidence will traverse approximately 0.66 radiation lengths of material in the central solenoid. When operating at the nominal current of 7.73 kA, the solenoid stores 38 MJ of energy and produces an axial field of 2 T along the beamline. This field bends the tracks of charged particles in the inner detector in the R - ϕ plane [6]

ATLAS' three toroid magnets serve to bend the trajectories of muons exiting the detector. This bending makes it possible to measure the momenta of the muons with the muon spectrometer. Each of the three toroid magnets consists of eight flat coils spaced evenly around the 360° of ϕ space around the beamline, with 45° between each coil. The coils of the end-cap toroids are rotated 22.5° around the z-axis so that they lie in the gaps between the barrel toroid coils. Each of the toroid coils runs at a current of 20.5 kA and have a maximum field strength of 4 T on the coil. The centers of the barrel and end-cap coils experience a field of 0.5 T and 1.0 T respectively. These fields bend muons in the R - z plane [6]. The maximum field in the Small Wheel region of the muon spectrometer is 1.0 T, meaning that some tracks can have significant bending. However, there are some areas of the Small Wheels that have low field where the muon trajectories will experience minimal bending.

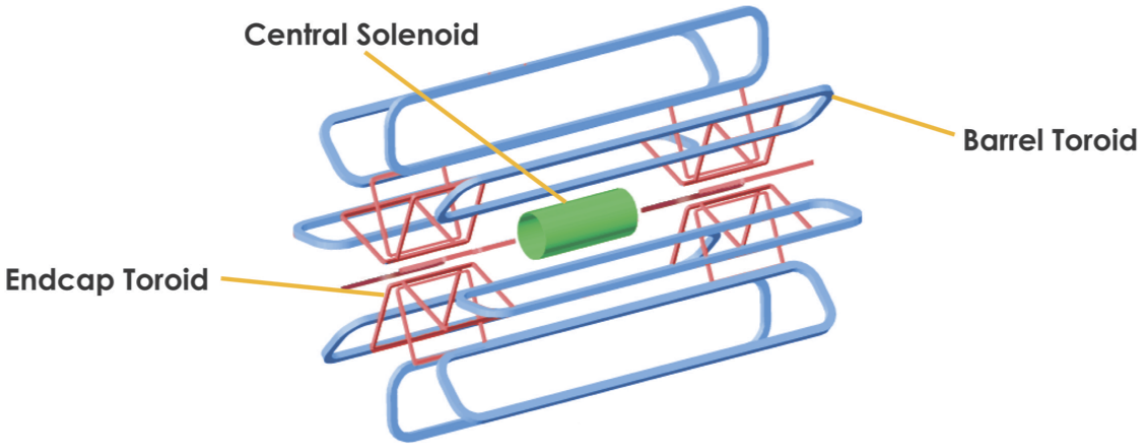

Figure 2.8: A diagram of the ATLAS magnet system. The central solenoid is shown in green, the end-cap toroids in red, and the barrel toroid in blue [13].

2.6 The Muon Spectrometer

The outermost component of ATLAS is the muon spectrometer. Muons interact minimally with the calorimeters, and thus need a dedicated system to accurately measure their momentum. The three toroid magnets of ATLAS are contained within the muon system, and provide strong magnetic fields to bend the passing particles. The bending in the R - z plane by the toroid magnets allows for the measurement of the sagitta of their trajectory, which can be used to measure their momentum. Four different detector technologies have been implemented into the current spectrometer to provide precision position measurements and trigger capabilites: Monitored Drift Tubes (MDTs), Cathode Strip Chambers (CSCs), Resistive Plate Chambers (RPCs), and Thin Gap Chambers (TGCs). The MDTs and CSCs primary function is precision measurement of momenta while the RPCs and TGCs are implemented in the ATLAS trigger system [14]. These technologies will be described in detail in sections 2.6.1 - 2.6.4.

Like the calorimeters, the muon spectrometer is arranged into barrel and end-cap regions. The barrels consists of three cylindrical shells centered around the beamline. The end-caps consist of three wheel stations, known as the Small Wheel, the Big Wheel, and the Outer Wheel, which are located at $|z| \approx$ 7.4 m, 14 m and 21.5 m respectively. The barrel toroid magnets are located between the inner and outer layers of the barrel detectors, labeled Barrel Inner Layer (BIL) and Barrel Outer Layer (BOL) respectively. The end-cap toroid resides between the Small Wheel and the Big Wheel. The overall layout of the muon spectrometer provides excellent coverage in the range $|\eta| <$ 2.7. The detector is arranged such that any muon exiting the system should pass through three layers of the spectrometer [14]. An extra layer of MDTs, labeled EEL (End-cap Extra Layer) in Figure 2.10, was added to fill a gap where muons could pass while only encountering two layers. The layout of the muon detectors can be seen in Figure 2.9, and a detailed schematic of a quadrant is shown in Figure 2.10.

2.6.1 Monitored Drift Tubes

Monitored Drift Tubes provide the large majority of the precision tracking capability of the muon spectrometer. They are in all three layers of the barrel section, as well as in all stations of the end-cap. The only region where they are not responsible for the precision tracking is in the most forward regions of the Small Wheels in the range

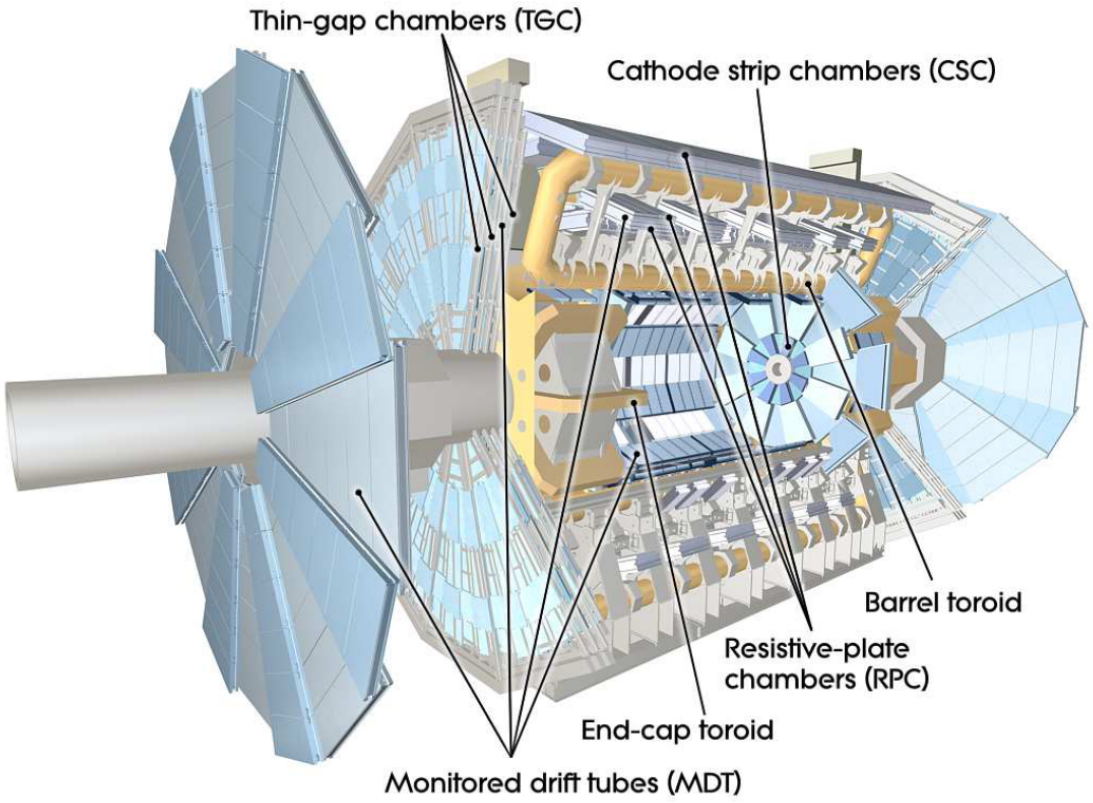

Figure 2.9: A cut-away diagram of the ATLAS muon system [6].

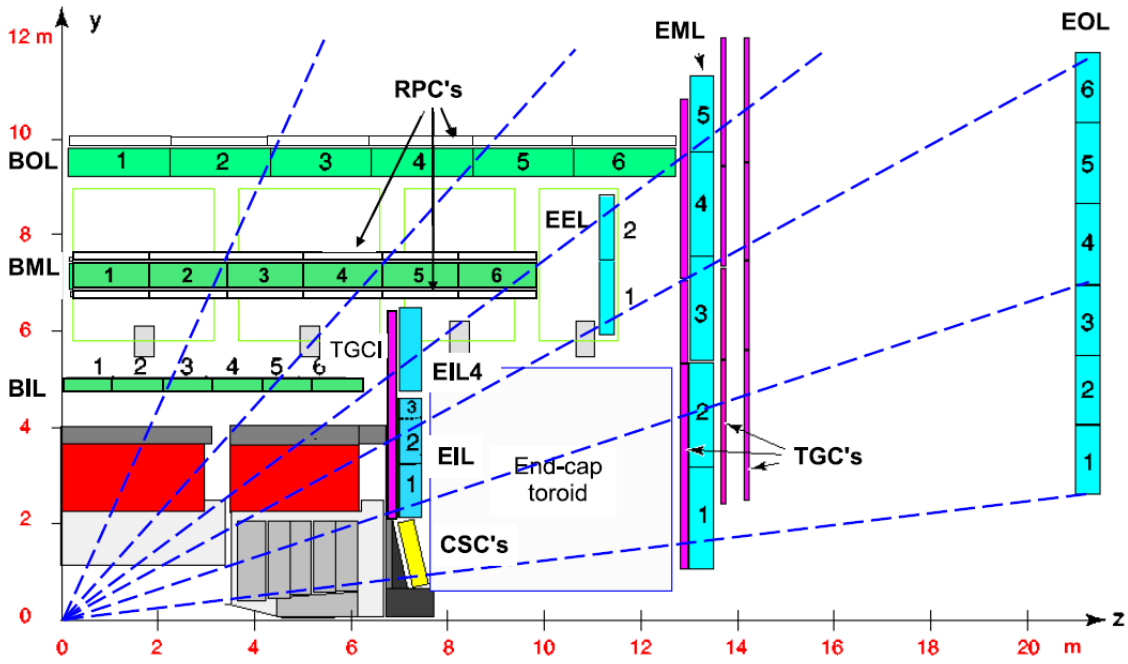

Figure 2.10: A schematic of a quadrant of the ATLAS muon system [6]. The MDTs in the barrel are shown in green, and the MDTs in the end-caps are shown in blue. TGCs are shown in purple, CSCs in yellow, and the RPCs are shown as white boxes.

$2.0 < |\eta|$. An individual MDT consists of a 30 mm diameter aluminum tube with a 50 μm tungsten-rhenium cathode wire strung down the axis. The tube is filled with an Ar/CO_2 gas mixture and the cathode wire is held at a potential of 3080 V relative to the wall of the tube [6]. Particles that pass through the tube ionize the gas and the resulting electrons drift to the wire and produce a signal. The tubes in the barrel are arranged in planes of fixed R and point in the ϕ-direction, while the tubes in the end-caps are in planes of fixed z and point in the ϕ-direction. An individual MDT hit has a precision of 80 μm in the bending coordinate (R for the end-cap and z for the barrel), but due to long drift times of up to 700 ns, they are a relatively slow detector compared to the rest of the muon spectrometer [6].

Individual tubes are assembled into monolayers, which are then assembled into multilayers of three or four monolayers each. Finally, two multilayers are then glued to each other with a spacer in between them to create a chamber. For a muon leaving the interaction point, it will pass through 8 MDTs in the inner layer, 6 MDTs in the middle layer and 6 MDTs in the outer layer, for a total of 20 MDT hits. This is true of both the barrel and the end-cap regions [14].

2.6.2 Cathode Strip Chambers

Cathode Strip Chambers are used for precision tracking in the forward regions of the spectrometer that experience high particle flux ($2.0 < |\eta| < 2.7$). CSCs are a type of multiwire proportional chamber with the two cathode planes segmented into strips. A layer of anode wires is strung between them and the gap between the cathode layers is filled with an Ar/CO_2 gas mixture. One layer of strips runs parallel to the wires and the other layer is oriented perpendicular to the wires. This allows for the measurement of both the radial and transverse coordinate of the passing particle. CSCs were chosen for the forward detector because of their excellent time resolution ($\approx$ 7 ns) and their ability to operate safely and efficiently in very high rate environments [6].

2.6.3 Resistive Plate Chambers

Resistive Plate Chambers provide the primary trigger signal in the barrel region of the muon spectrometer ($|\eta| < 1.05$). RPCs are a type of gaseous parallel plate detector with the plates segmented into strips. The two planes of strips are separated by 2 mm spacers and have strips oriented orthogonal to each other. The orthogonality of the strips allows for measurements of both the z- and ϕ-coordinates in the barrel.

The ϕ-coordinate is measured with a higher precision than the z-coordinate as the MDTs in the barrel already provide an excellent z measurement. An electric field of approximately 5 kV/mm fills the gap between the parallel plates and allows for quick detection of ionization. RPCs exhibit a fast signal development time and a time resolution on the order of 1 ns, and are thus excellent for use in the trigger system, which requires prompt input for its decisions [14].

2.6.4 Thin Gap Chambers

The final type of detector in the muon spectrometer is the Thin Gap Chamber. TGCs are a type of multiwire proportional chamber filled with a mix of n-pentane and CO_2. The thin gas gap has high voltage anode wires strung between the cathode planes. One of the cathode planes is segmented into strips that run radially and provide for the measurement of the ϕ-coordinate of a track. A schematic of a TGC layer is shown in Figure 2.11, and a diagram of the electric equipotential lines near the TGC wires is shown in Figure 2.12. Each TGC consists of multiple gas gaps and are referred to as doublets (2 layers) or triplets (3 layers). Excellent time resolution allow the TGCs to serve as the trigger chambers in the end-cap region of the spectrometer. TGCs are implemented on both the Small Wheel and the Big Wheel, with a single doublet used on the Small Wheel to provide the ϕ measurement of the tracks to complement the MDTs. In the later part of Run 2, this doublet was also implemented into the trigger to search for hit coincidences with the Big Wheel. The Big Wheel has a total of seven TGC layers (one triplet on the inside and two doublets on the outside) that are used to produce trigger signals for the end-cap. TGCs are not used in the Outer Wheel because there is no magnetic field to bend the muon paths between the Big and Outer Wheels. Thus, the ϕ-coordinate can be extrapolated from the previous measurements [14].

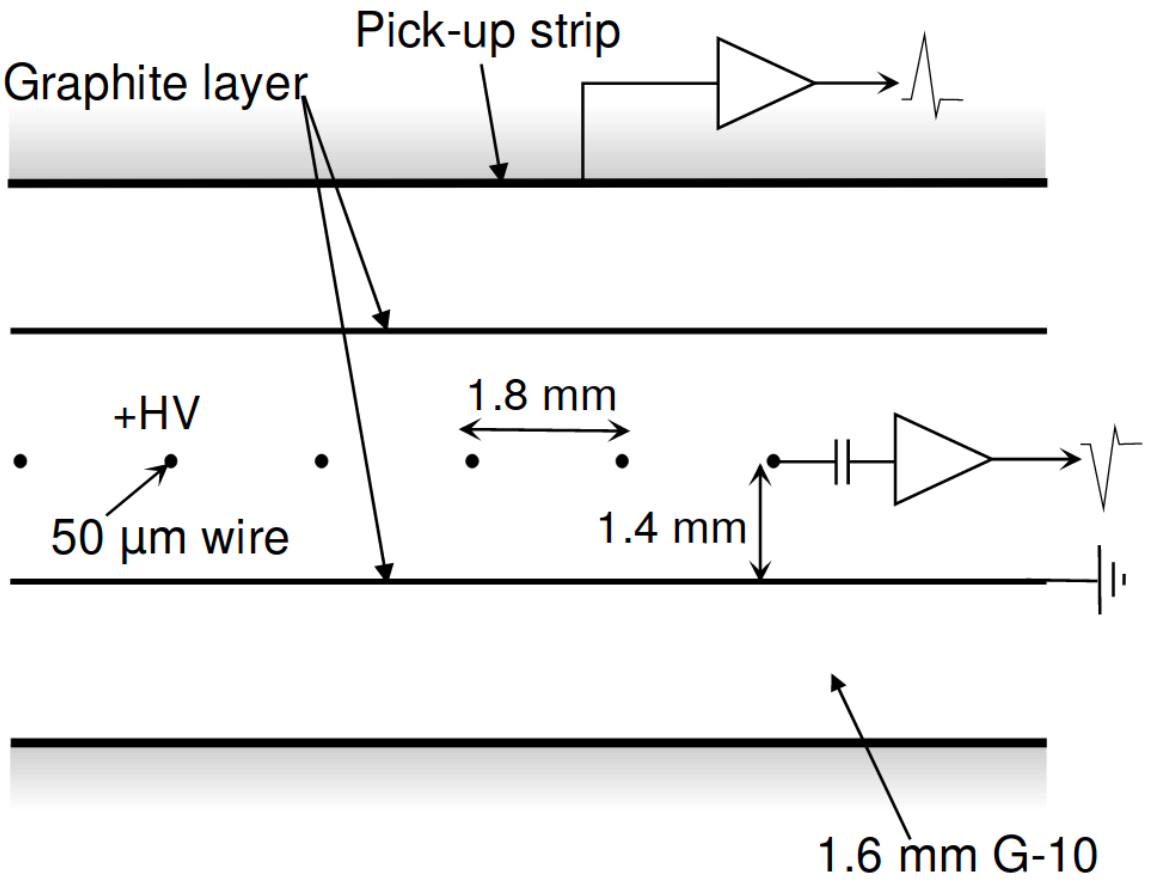

Figure 2.11: A schematic of an ATLAS TGC [14].

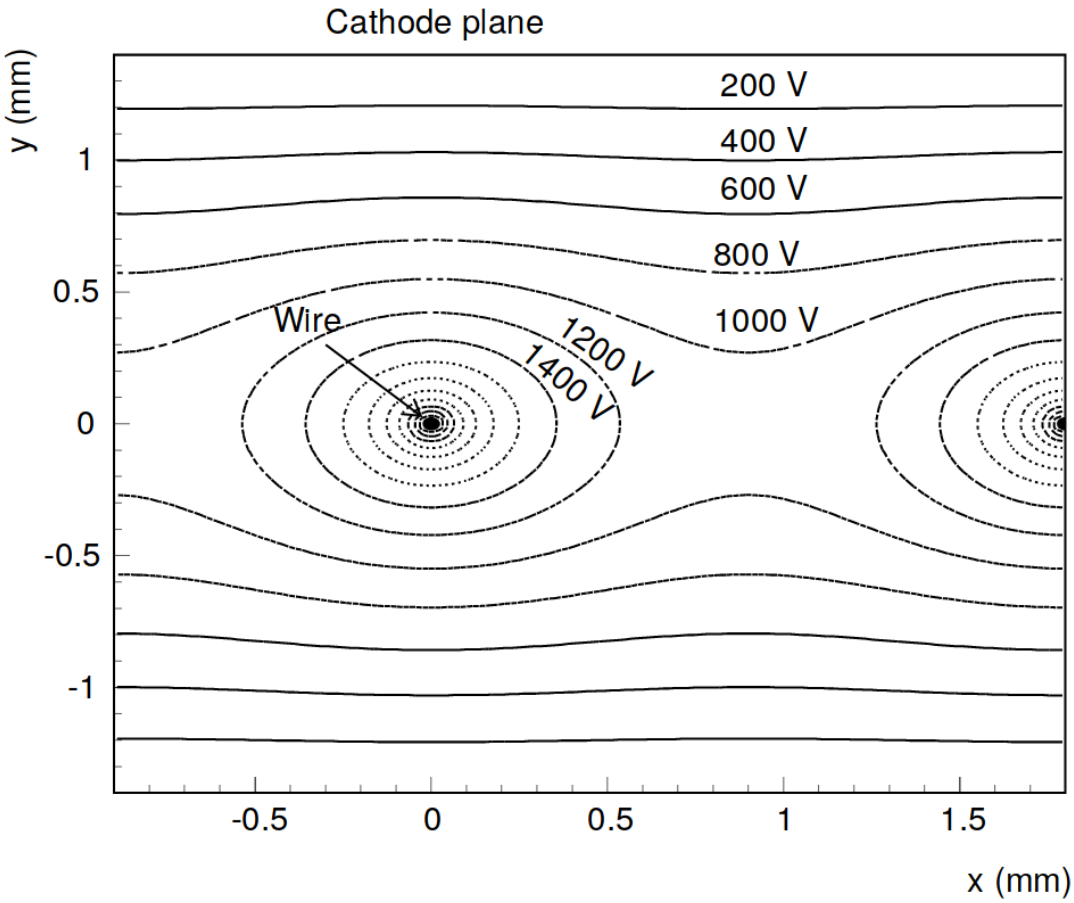

Figure 2.12: A diagram of the equipotential lines near the anode wires of a TGC [14]. The closely spaced equipotential lines near the wires imply a strong electric field that can initiate electron avalanches.

Chapter 3

The New Small Wheel

In December of 2018, the Large Hadron Collider stopped colliding and circulating beams and entered Long Shutdown 2 (LS2). It will remain off until 2021 when it will return to operation with an increase in luminosity and a potential increase in beam energy up to 7 TeV per beam. During this shutdown, each LHC experiment will be constructing and implementing upgrade projects. The major upgrade for ATLAS is the New Small Wheels (NSWs) project, a cross-institutional endeavor to replace the current Small Wheels of the ATLAS muon spectrometer.

3.1 Motivation

The importance of the NSW upgrade is due to the increase in luminosity that will come after LS2. The luminosity will increase even further after Long Shutdown 3, after which the LHC will enter its High-Luminosity LHC phase. This increase in luminosity brings many technical challenges with it to ATLAS. Two of these issues will be addressed by the NSW upgrade: the degraded tracking and decreased efficiency of the Small Wheels, and the effectiveness of the Level 1 muon trigger.

First, the muon tracking performance of the Small Wheels has been shown to degrade with the previous LHC luminosity increases. Both the efficiency of the detectors and the position resolution is severely impacted by these increases in rate. If the Small Wheels were to continue operation, ATLAS' ability to accurately measure muon momenta in the end-cap regions would be significantly degraded [15]. The New Small Wheels will aim to fix this through the use of novel detector technologies that can operate at high efficiency and resolution in spite of the high rate.

3.1.1 The Level 1 Muon Trigger

Proton bunch crossings occur in ATLAS every 25 ns, or at a frequency of 40 MHz. Each bunch contains approximately $1.15 \cdot 10^{11}$ protons. Every time bunches cross inside ATLAS, an average of 40 proton-proton interactions occur. If ATLAS were to record all of this data, it would fill over 50 TB of data each second. This isn't physically plausible, so ATLAS applies a trigger system to select events that the collaboration believes are a part of interesting physics processes or are applicable to measurements of interest.

The ATLAS trigger system is separated into levels. The first level, known as the Level 1 trigger, does a quick analysis using information from the calorimeters and the muon spectrometer to identify potential events of interest. It looks for high-p_t muons, electrons, photons, jets, and taus and uses these signatures to decide on whether an event may be worth keeping. This information is used to identify possible regions of interest and trim the bunch crossing acceptance rate from 40 MHz down to 100 kHz. All bunch crossings that pass the Level 1 trigger are then analyzed in more detail by the High Level Trigger (HLT). The Level 1 trigger passes the regions of interest to the HLT, which uses them for reconstruction of the events. If an event is accepted by the HLT, the event is written to disk storage. In total, the trigger system accepts bunch crossings at a rate of 1 kHz and records those events to disk [16].

The muon portion of the Level 1 trigger works by searching for hit coincidences across multiple layers of trigger chambers (RPCs in the barrel and TGCs in the end-cap). They require that the coincidences point towards the interaction point. The trigger chambers are sorted into two categories in both the barrel and end-cap regions - pivot and confirm. For each region of interest in the pivot plane, there are identified regions of the confirm plane where a muon of a certain p_T is able to also register a hit. These regions are determined by factors such as the magnetic field in the region and account for effects such as Coulomb scattering. The trigger in the end-cap region works by first registering a hit in the pivot plane of the TGCs. Then, based upon the region hit in the pivot plane, the corresponding regions of the confirm plane are searched for hits that could match to the hit in the pivot plane [17]. If it identifies matching hits in both the pivot and confirm regions that point to the interaction point, it is a candidate event and could be accepted. A diagram of a muon spectrometer quadrant with the trigger chambers highlighted is shown in Figure 3.1.

The New Small Wheels will help to solve several issues with the Level 1 muon trigger. The original Level 1 muon trigger only used the TGCs in the Big Wheels of the end-cap. Because of this, fake muon triggers were a significant hindrance to ATLAS' trigger performance during Run-1. Protons originating in the end-cap toroids can pass through the Big Wheel at angles similar to muons originating from the interaction point. Studies of the 2012 data have shown that appoximately 90% of end-cap triggers from the muon system were fakes, a factor of eight to nine more than in the barrel region [15]. Figure 3.2 illustrates how the original muon trigger system could misidentify fake triggers. Because of this issue, the TGCs of the Small Wheel were implemented into the Level 1 muon trigger starting in Run-2. The Run-2 trigger required a track in the Big Wheel to have a coincidence hit in the Small Wheel in order to be accepted. This greatly reduced the number of fake triggers in the end-caps [18]. However, fakes still remain a problem for the trigger system, and the implementation of the NSWs will help to reduce the rate of fakes while improving the high rate capabilities of the muon trigger system.

3.2 Performance Requirements

Run-3 of the LHC from 2021 to 2023 will operate at a luminosity of 2-3 $\cdot 10^{34}$ cm^{-2}s^{-1} and will have between 55 and 80 proton-proton collisions per bunch crossing. These conditions will become even more demanding following the upgrade to the High-Luminosity LHC in 2026. Stringent performance requirements have been implemented in order to ensure that the NSWs can meet the demands of ATLAS throughout the remaining lifetime of the experiment. The NSW has been designed to be able to operate efficiently up to a luminosity of 7 $\cdot 10^{34}$ cm^{-2}s^{-1} and to a maximum of 200 interactions per bunch crossing [15].

For the NSW tracking to meet ATLAS' physics goals under these conditions, it has been determined that the detectors should have a p_t resolution of 10% for 1 TeV muons across the full η coverage of the NSW. This amounts to a position resolution of 50 μm in the R - ϕ plane, or a resolution of 100 μm per plane of a detector with four layers. The NSW should also exhibit a segment finding efficiency greater than 97%. Very high momentum muons can free δ rays inside the detector and initiate showers. The efficiency and tracking resolution of the detectors should not suffer even in this high momentum regime. The trigger demands of the NSW require that the detectors should provide an angular resolution of 1 mrad or less for track segment

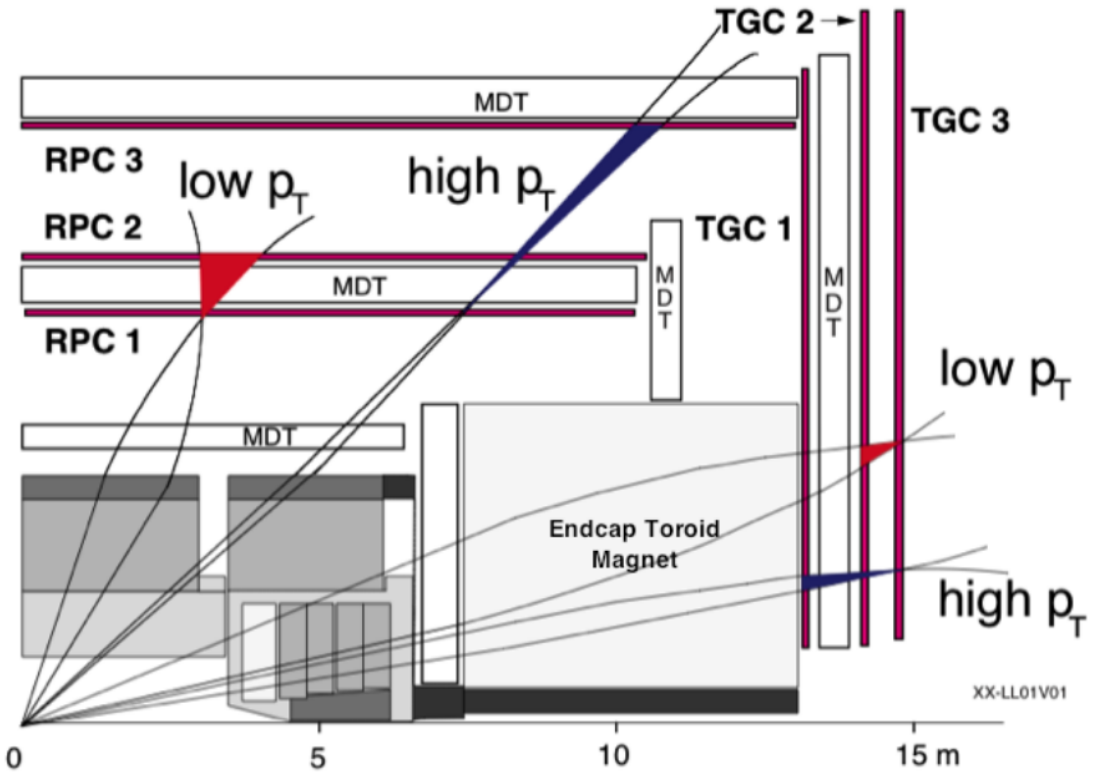

Figure 3.1: A diagram showing the trigger chambers used in the original Level 1 muon trigger [17]. The trigger chambers are highlighted in red.

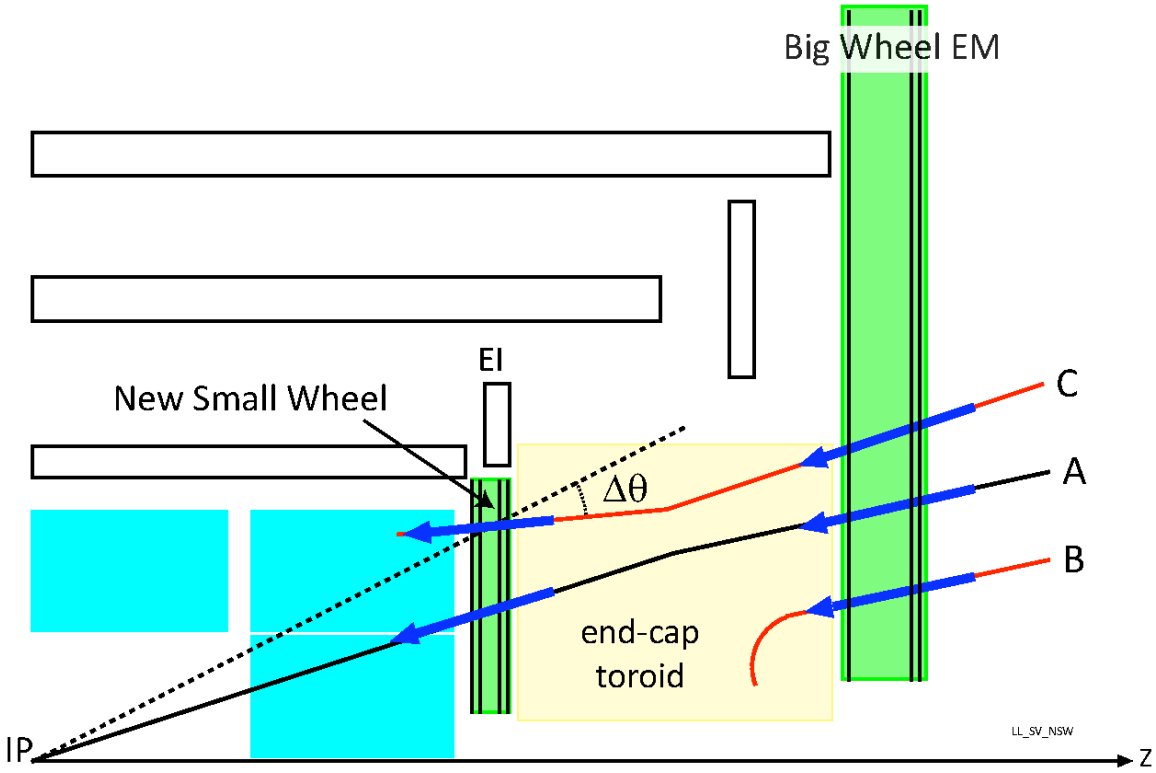

Figure 3.2: A diagram showing possible fake trigger candidates [15]. The original trigger system using only the Big Wheel would accept all three tracks, even though only track A is caused by a particle from the interaction point. The implementation of the NSWs will allow the trigger to properly reject tracks B and C in the high rate environment of Run-3.

reconstruction. In order to bring the trigger rate down to the desired level, the track segments should also have "a granularity better than 0.04 $\times$ 0.04 in the η - ϕ plane to match the one of the current muon trigger system [15]." A full list of the performance requirements for both the tracking and trigger systems of the NSW can be found in the New Small Wheel Technical Design Report [15].

To meet these requirements, two technologies have been chosen to replace the current MDTs, CSCs, and TGCs of the Small Wheels. The first is the small-strip Thin Gap Chamber (sTGC), an upgrade of the existing ATLAS TGCs, and the second is the micro mesh gaseous structure detector, which are commonly referred to as micromegas (MM). The sTGCs will serve as the primary trigger chambers for the NSW while the micromegas provide precision tracking [15]. Both detectors will be described in the following sections.

3.3 NSW Geometry

The New Small Wheel upgrade is divided into sectors. Each wheel consists of 16 sectors, extending radially outward from the center of the disk. All sectors will incorporate both technologies. Of the 16 sectors, 8 of them are large sectors and 8 are small sectors. Each sector is subdivided into modules that are then assembled radially outward in the R-direction. Each module consists of four layers of detector elements. There are a total of six modules for the sTGCs - three for the large and three for the small sectors - and there are four for micromegas - two for each size sector. Rotating about the beam axis in ϕ, the sectors will alternate between large and small, with the small sectors forming a plane closer to the interaction point and the large sectors forming a plane further away from the interaction point [15]. The sector structure of the NSW can be seen in Figure 3.4, with large and small sTGC wedges shown as well. A small amount of overlap is present between adjacent sectors, ensuring full coverage. The overlap can be seen in Figure 3.3.

Each individual sector will consist of 4 wedges - an sTGC pivot wedge, two MM wedges, and an sTGC confirm wedge. The pivot and confirm chambers will be used in a similar way as they are in the current Level 1 muon trigger. A hit in a pivot chamber will then prompt a search of regions of the confirm chambers for corresponding hits. For both large and small sectors, the MM wedges will be located between the two sTGC wedges. For small sectors, the confirm sTGC wedge is located on the side of the interaction point with the pivot wedge on the side away from the interaction

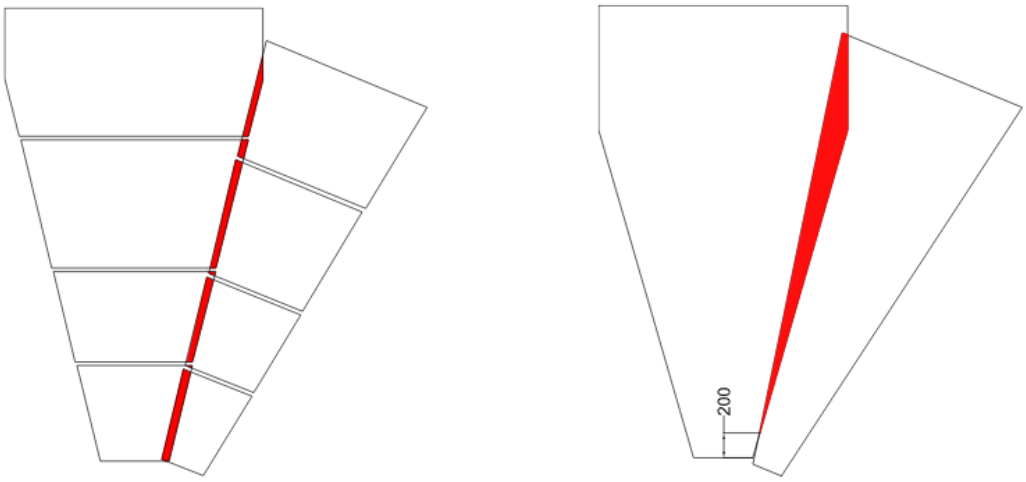

(a) sTGC detectors.

(b) MM detectors.

Figure 3.3: A diagram showing the overlap between large and small wedges in the NSW [15]. The QS1 and QL1 modules, the modules closest to the beam-pipe, are divided into two chambers.

point. Large sectors have the confirm wedge away from the interaction point and the pivot wedge on the side of the interaction point, which is the opposite of small sectors. [15]. Thus, a muon leaving the interaction point and passing through the New Small Wheel may encounter wedges in the following order: small confirm sTGC → small MM → small MM → small pivot sTGC → large pivot sTGC → large MM → large MM → large confirm sTGC. Since each module is four layers and each sector consists of four wedges, a muon passing through a single sector will traverse 16 total layers of detector.

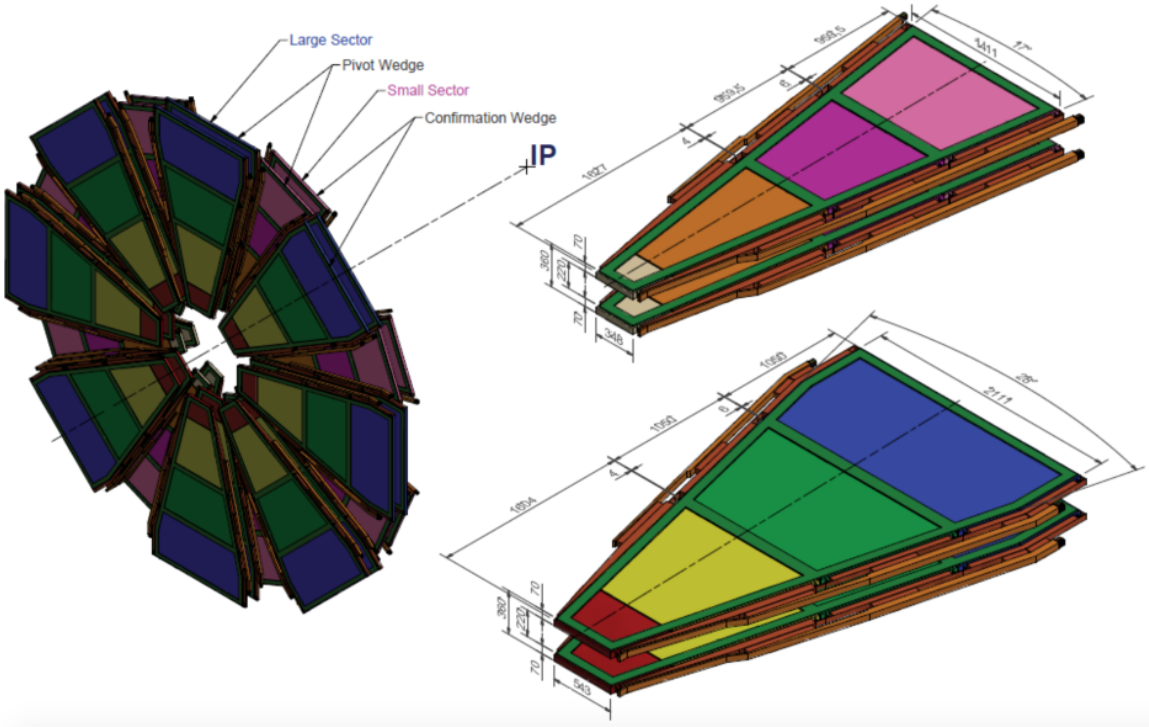

Figure 3.4: A diagram of the New Small Wheel and the sTGC wedges [15]. The QS3 (pink) pivot modules and QL2 (green) modules are produced in Canada at TRIUMF and Carleton University.

3.4 Micromegas

The micromegas detectors have been chosen to provide precision tracking in the NSW because of their ability to provide excellent spatial resolution under high rates, such as those that will be observed in the end-caps during the high luminosity runs of the LHC. Developed in the 1990s, a single micromegas layer consists of a drift cathode, a

metallic micromesh and a strip anode board. The mesh is separated from the readout electrodes by a very short distance (128 μm in ATLAS). The drift cathode is held at a negative high voltage, the mesh is grounded, and the anode strips are held at a positive high voltage. The region between the drift cathode and the mesh is known as the conversion region, while the gap between the mesh and the anode is called the amplification region. The design can be seen in Figure 3.5. Passing muons ionize the Ar/CO_2 gas mixture in the detector causing electrons to drift towards the mesh and ions to move towards the drift cathode. When the electrons pass the mesh, they enter the amplification region between the mesh and the readout strips, where the electric field is between 40 and 50 kV/cm. Electrons are then quickly accelerated towards the strips, producing an avalanche of electrons in their wake. Though the drift of electrons through the conversion region can take tens of nanoseconds, the amplification between the mesh and the strips unfolds in less than a nanosecond. Fast pulses are generated due to this design. The ions created by the avalanche drift to the cathode relatively quickly, making the micromegas detector suitable to operate in high rate environments [15].

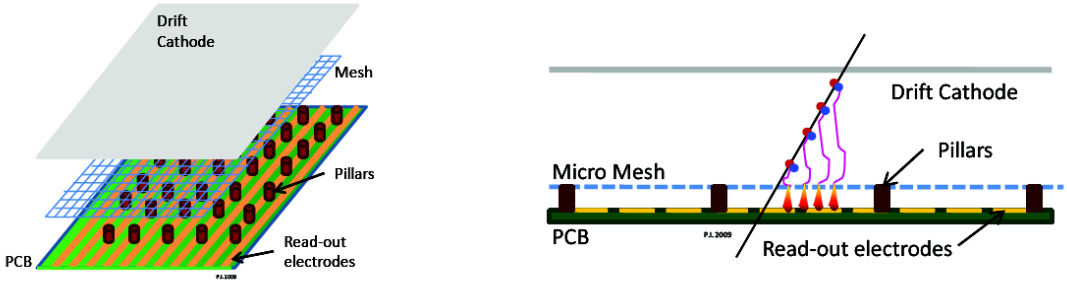

Figure 3.5: A diagram of the MM design and operating principles [15]. The micromesh layer is grounded between the negative high voltage drift cathode and the positive high voltage anode strips. These sketches are not to scale.

3.5 Small-strip Thin Gap Chambers

The other technology to complement the micromegas in the NSW is the Small-strip Thin Gap Chambers (sTGC). Designed to serve primarily as the trigger chambers of the upgrade, the sTGCs are an improvement upon the existing TGC technology currently used in ATLAS. An angular resolution of less than 1 mrad, as required by

the trigger system, will be provided by the sTGC detectors. In turn, this translates to a good online spatial resolution. sTGCs also exhibit the necessary excellent time resolution needed to serve in the trigger. This combination of characteristics allows the sTGC detectors to provide both reliable triggering as well as precision tracking. Thus, the combination of sTGCs and MM forms a fully redundant detector system.

3.5.1 Geometry and Operating Principles

A single sTGC consists of three different detector elements. Two cathode planes separated by 2.8 mm form the outside of the chamber. A plane of anode wires running radially lies 1.4 mm from the two cathode planes. The 50 μm gold-plated tungsten wires are held at a voltage of approximately 3 kV between the cathode planes, with a pitch of 1.8 mm. The cathode planes are formed out of several layers. At their base, they are a 1.1 - 1.3 mm thick PCB with a 100 - 200 μm thick layer of pre-preg over top of them. Over this, the cathode planes are sprayed with a mixture of graphite and epoxy. One of the cathode planes is segmented into rectangular pads that are used in the trigger system to identify regions of interest in the strips and wires. The other cathode plane is segmented into strips that run in the azimuthal direction. These strips have a pitch of 3.2 mm, much smaller than the strip pitch of the current ATLAS TGCs, leading to the name Small-strip Thin Gap Chamber. Figure 3.6 shows a schematic of a single sTGC layer [15]. Individual sTGC layers are then assembled into modules consisting of four sTGC layers, known as quadruplets. There are six sizes of quadruplets - QS1, QS2, QS3, QL1, QL2 and QL3. The Q in the name means quadruplet, the S or L denotes whether the module is part of a small or large wedge, and the number indicates the radial position of the module relative to the beam axis [15]. This structure is shown in Figure 3.7 [19].

The operating principles of an sTGC are analogous to those of the TGC. The gap between the cathode planes is filled with a gas mixture of n-pentane and CO_2, which is ionized by passing muons. The electric field within the chamber causes the freed electrons to drift to the wires while the ions are moved towards the pads and strips. The field strength ranges from one kV/cm to a few hundred kV/cm near the wires [20]. The acceleration of a freed electron through the electric field gives the electron enough energy to interact with and free subsequent electrons, causing an avalanche of particles close to the wire. The drift of the electrons and the resulting ions induces current signals on the different detector elements. The signal from the strips can be

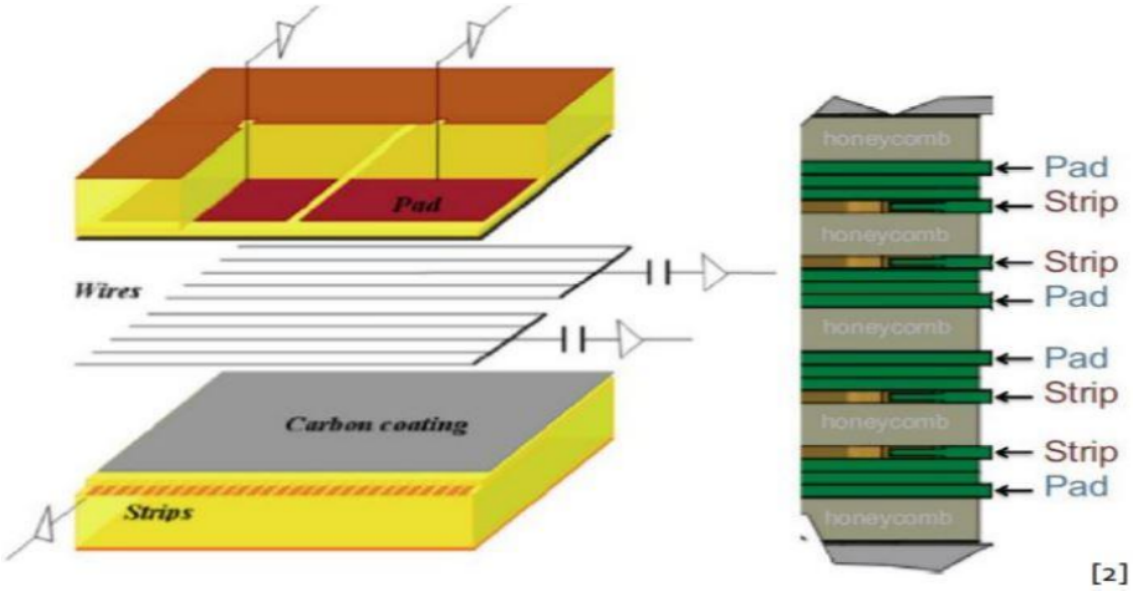

Figure 3.6: A schematic showing the structure of an sTGC detector [15]. The left depicts an individual layer of an sTGC while the diagram on the right shows a cross section of a full sTGC quadruplet.

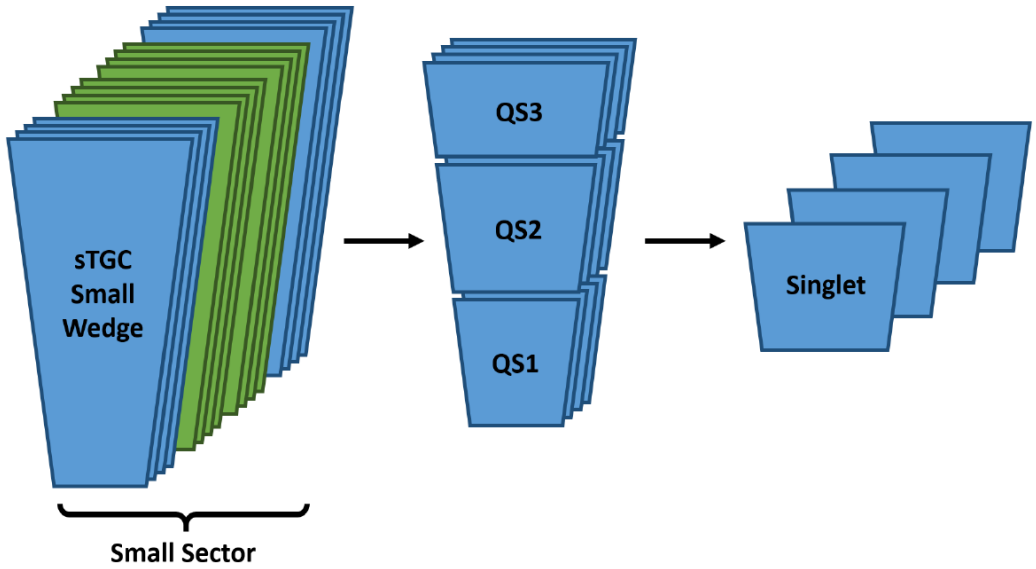

Figure 3.7: A graphic depicting the composition of a New Small Wheel sector [19]. The sTGC wedges are shown in blue and the Micromegas wedges are shown in green. Each wedge consists of three modules, with each module having four active detector layers.

used to make precision measurements of the R-coordinate of the particle, while the wires can produce coarse measurements in the ϕ-coordinate [15].

3.5.2 Construction

Each sTGC module is composed of four layers of detector elements. In order to ensure that precision alignment between layers is achieved, each board has two precision machined brass inserts on one of the angled edges. These brass inserts extend beyond the gas gap of the detector, and each one has a notch in it such that an alignment pin may be pressed against it. The notch in the brass insert near the long side of the board is V-shaped and the notch in the insert near the short edge is flat. The V-shaped insert and pin provide a fixed point for the board to rotate around, while the flat insert is pressed against the pin to fix the rotational degree of freedom. An engineering drawing of the V-shaped insert is shown in Figure 3.8. During assembly, precision 10 mm diameter alignment pins will be pressed into the notches of the brass insert in order to ensure good alignment between layers [15].

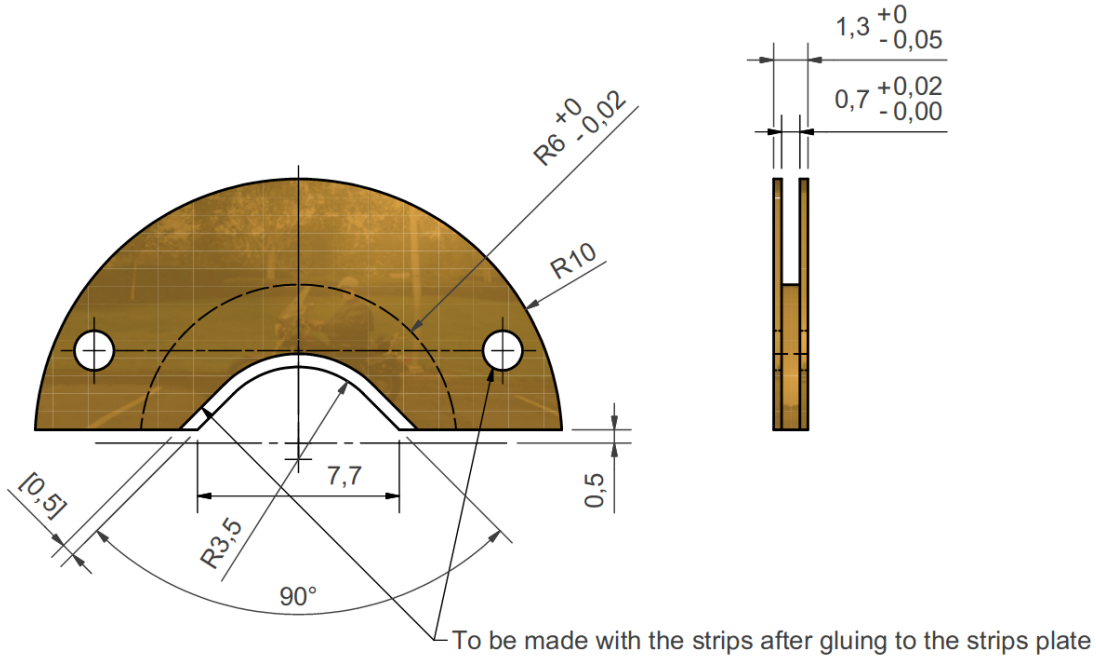

Figure 3.8: A drawing of the V-shaped brass insert used in the cathode boards of an sTGC [21].

Construction of an sTGC quadruplet starts with the reception of the cathode boards from the manufacturer. These boards are inspected and cleaned before being

sprayed with a layer of graphite. After the graphite spray, spacers are placed onto the board in order to form the gap between the cathodes. Wire supports are added at this step. The wires are then wound onto the pad cathode board. Once the wires have been wound and both the pad and strip boards have been sprayed, the sTGC layer can be glued shut. During gluing, the pad board rests on a flat granite vacuum table, and the strip board is glued on top of it. Small pins in precision slots are used to properly align the pad and strip boards. The completed layer, known as a singlet, is then gas sealed and undergoes testing [22].

Completed singlets are then assembled into pairs called doublets. A honeycomb frame spacer is used to separate the two layers. Doublets are assembled with the pads facing outward, away from the honeycomb spacer. When gluing doublets, the brass alignment inserts of the singlets are pressed up against the precision alignment pins to ensure that the two layers are well aligned. After undergoing testing for the doublet stage, the doublets are assembled into four-layered quadruplets in a similar manner. A cross-section showing the overall structure of the completed sTGC quadruplet can be seen in Figure 3.6. A total of five honeycomb spacer layers are used, with three separating the four detector layers and two separating the outer detector layers from the copper ground planes [22].

3.5.3 Performance Goals and Simulation Results

The sTGC detectors have been designed to provide precision tracking and trigger capabilities for the high-rate environment of ATLAS' muon end-caps during the runs of the High-Luminosity LHC. This includes a position resolution of less than 150 μm at rates up to 20 kHz/cm^2. The position resolution is a function of the angle of incidence of the particle. Test beam results from 2009 show that for a strip pitch of 3.2 mm, the position resolution ranges from approximately 60 μm at perpendicular incidence to 150 μm at the highest incidence experienced in the NSW. The sTGCs will also be able to measure the ϕ-coordinate of a track with a resolution of 1-2 mm. This allows for the muon spectrometer to connect tracks to those observed in the inner detector. Furthermore, the sTGC pads must be able to produce 3-out-of-4 coincidences with an efficiency of 90%. This corresponds to a single layer efficiency requirement of 96.5%. Lastly, in order to ensure that the chamber has the necessary good timing properties needed to serve in the trigger, the chamber should have a drift time of less than 25 ns (one LHC bunch crossing) for most electrons [15].

Numerous simulations of sTGC detectors have been completed to demonstrate that they meet their requirements for their role in the NSW. The time spectrum of muons arriving perpendicular to the plane of the detector was simulated and showed that 95% of events are contained within a 25 ns time window. Another simulation showed that the Lorentz angle of electrons in the chamber doesn't exceed 6.5° for the maximal 1 T magnetic field that will be present in the sTGCs[1]. Thus, their drift times will not be noticeably increased. The results of further studies can be seen in the Technical Design Report for the New Small Wheel [15].

3.6 Detector Readout

The electrons and ions produced by passing muons drift to the electrodes of the sTGC due to the electric field. The movement of these ions induces signal currents in the pads, wires and strips of the detector. The detector elements carry these signals to the edges of the board, where they are read out and interpreted by a series of electronic components. The signals are first transferred into the adapter boards, and then to the Front End Boards (FEBs). Finally, if an event is triggered on, the Data Acquisition (DAQ) system will receive the signals and is able to build events to be analyzed later.

3.6.1 Adapter Boards

When the signals in the wires, pads and strips are moved to the edges of the boards, they are spread out along the length of the board. The edges of the boards are between 1 and 2 m long. In order for the signals to be read out in a quick and efficient manner, they must be collected in a smaller area where they can be transferred to the FEBs. To do this, adapter boards are soldered onto the edges of the board to collect the signals into a smaller area. Each channel of the detector is soldered to an element on the adapter boards, where it is transferred to the readout electronics. There are multiple types of adapter boards for the different signals. Pad adapter boards collect the pad and wire signals on one end of an sTGC layer while strip adapter boards gather the strip signals on the other side. Each layer has both a pad and strip adapter board, for a total of 8 on the edges of a quadruplet [19].

[1]The Lorentz angle is the angle that a particle moving in an electric field will be deflected by due to the magnetic field.

On the parallel sides of the trapezoidal structure of an sTGC layer, wires adapter boards apply high voltage to the wires and route the signals to the readout electronics. Each wires readout channel is connected to a group of 20 wires, spanning a distance of 3.6 cm. There are three types of wires adapter boards: Wires 0, Wires 1 and Wires 2. The Wires 0 boards are only used on QS1 and QL1. These modules are divided into two halves in the R-coordinate. The segment closer to the beamline has the wires at high voltage, but does not read them out. The Wires 0 board applies the high voltage to these wires on the short edge of the quadruplet. The Wires 1 adapter boards are soldered onto the long edges of each layer of the quadruplet. The Wires 1 Boards provide high voltage to the wires and collect the signals to be delivered to the Front End Boards. On top of the Wires 1 boards, a single Wires 2 adapter board is attached to all of the Wires 1 boards. The Wires 2 board runs along the long edge of the quadruplet and extends beyond. At the tips of the Wires 2 board, four flat cables carry the wires signals into the pad adapter board. Here they can be readout by the pad Front End Boards. A fully equipped quadruplet will have four pad adapter boards, four strip adapter boards, four Wires 1 adapter boards, and a Wires 2 adapter board. QS1 and QL1 quadruplets will have an additional four Wires 0 adapter boards. [19]

3.6.2 Front End Boards

The adapter boards transfer the signals produced by the detector into small high-density connector elements, known as GFZ connectors. The GFZ connectors are used to attach the readout electronics to the adapter boards and to pass the signal between the two. Two types of front end boards are used with sTGCs: pad Front End Boards (pFEBs) and strip Front End Boards (sFEBs). The pFEBs are responsible for reading out the pad and wire signals, and the sFEBs are used to read out the signals from the strips. Numerous versions of the FEBs have been developed. The FEBs described here are Version 2.1, the version that was used in the test beam. Each FEB is operated at a voltage between 8 and 10 volts through a low voltage connection. A custom DC-DC converter made at CERN known as the FEAST distributes the low voltage power across the board. A custom 64 channel ASIC known as the VMM provides features such as charge amplification, discrimination, amplitude and timing measurements, and analog-to-digital conversions of the signals. The VMM chip is used on all of the readout electronics for the NSW. pFEBs have 3 VMM chips, while

sFEBs contain 8 VMM chips due to the high number of channels. The VMMs process the data before passing it on to a Field Programmable Gate Array (FPGA) [23]. Each FEB has several connectors, allowing the board to interface with the trigger system and the Level 1 Data Driver Card, a custom board designed to quickly communicate with many FEBs [24]. It also has a twinax cable connection to connect it to the DAQ as well as LEMO cable connectors used for analog output of signals. The analog outputs of the board are useful for diagnostic and troubleshooting purposes. An updated version of a pFEB is shown in Figure 3.9[2].

There are several versions of the FEBs. The FEBs described in the previous paragraph are Version 2.1. This version was used in the test beams that will be described in the following chapter. An upgraded version known as Version 2.3/2.3a has been produced and will be used as the final electronics for the sTGCs. It makes several changes to Version 2.1 of the FEBs, including a location change for the FEAST to help reduce noise, and the replacement of the FPGA with a Read Out Controller (ROC).

3.6.3 The π-Network

Some of the pFEBs have an additional component on them known as a π-network. It is a circuit element consisting of two resistors and a capacitor that serves to attenuate the signals that move to the VMM. A circuit diagram is shown in Figure 3.10. The VMM is implemented on the front-end electronics of both the Micromegas and sTGCs, though it was designed primarily for the Micromegas. The Micromegas have much smaller strips and pads than the sTGCs and thus the charge is distributed among more channels. Some of the muons passing through the detector deposit large amounts of charge. These large charge depositions can saturate the VMM channels for the sTGCs, leading to a loss of information on timing and pulse amplitude. The π-network has been implemented to reduce the largest pulse sizes to avoid saturation. The attenuation factor of the π-network is given by

$$\mu = \frac{C_\pi}{C_\pi + C_{Pad}}, \tag{3.1}$$

where C_π and C_{Pad} are the capacitance values of the π-network and pad respectively. Because the pads vary in size, their capacitance values span a large range.

[2]Picture courtesy of the University of Science and Technology of China.

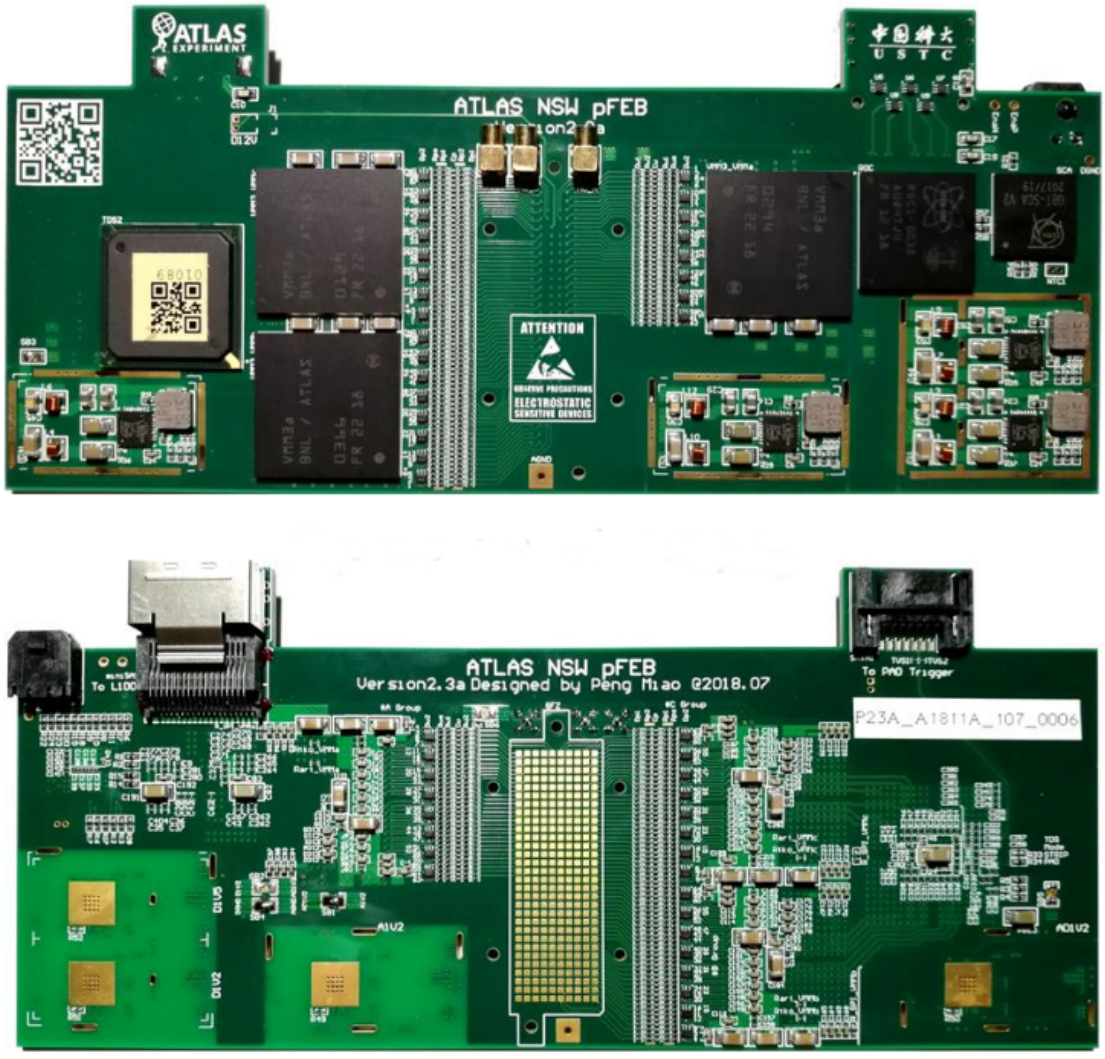

Figure 3.9: The front (top) and back (bottom) of a Version 2.3 pFEB[2].

Thus, if a pFEB has a given capacitance value for all of its pad channels, the attenuation factors will be different for each pad. If the attenuation factor is too low, the largest pulses can still saturate the channel, but if it is too high, some of the smaller pulses may be diminished below the threshold of detection and will lead to a decreased detector efficiency. Due to the large range in pad sizes, two different values of the capacitance have been chosen for use on different modules to try to avoid these potential issues.

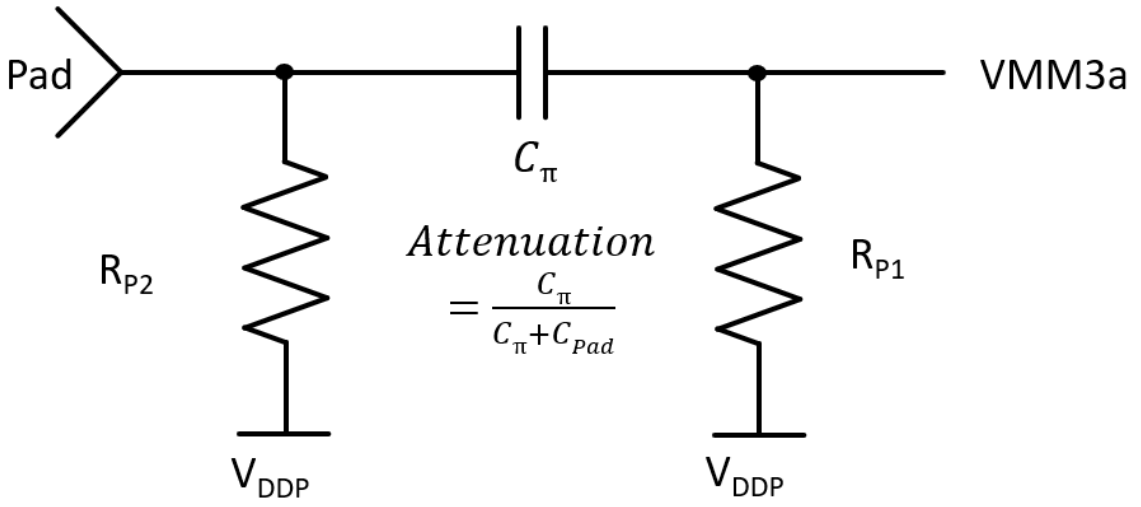

Figure 3.10: A circuit diagram of the π-network in the pFEBs. The value of the capacitor determines the attenuation factor of the circuit.

3.6.4 Timing

The VMM tracks the arrival time of pulses with two quantities. The first is called the Bunch-Crossing Identification, or BCID. The BCID serves as a coarse timer with a single BCID corresponding to a 25 ns windows. This 25 ns window corresponds to the bunch spacing between LHC proton bunch crossings. The second quantity, called the Time of Detector Output (TDO), provides fine timing information for within the window of an individual BCID. The Version 2.1 FEBs do not have synchronized BCID clocks for each VMM. Thus, for signals that arrive at the same time on different VMMs, the BCID value will not necessarily be the same. This leads to a pair of VMMs having a constant offset between their two BCID values. The value of this offset remains constant until the boards are reconfigured by the DAQ. This offset

must be measured in order to properly group signals together into individual events. A solution to this will be presented in Chapter 4.

3.6.5 Data Acquisition

The data acquisition system (DAQ) used for the sTGCs employs a KC705 FPGA board connected via an FMC connector to a custom built miniSAS-FMC board. The miniSAS-FMC board is connected to all eight of the FEBs on a quadruplet via flat miniSAS twinax cables. The collection of these components is known as the miniDAQ. The FPGA board has an ethernet port to allow data flow to and from a PC [25]. Custom software developed by the University of Science and Technology of China allows the PC to interface with the FEBs through the miniDAQ system. FEBs and individual VMMs can be configured through the miniDAQ board. The software passes commands to the FPGA on the miniDAQ via ethernet cable, which then passes the configurations to the VMMs. Parameters such as the gain and thresholds of the VMMs can be set through the miniDAQ software. The software also allows for the masking of individual channels, the delivery of test pulses, and the output of the analog signals received by the FEB, among other features. It provides a suite of helpful diagnostic and experimental tools. When collecting data, the miniDAQ delivers the data to a PC through the ethernet cable, where it can be stored for later analysis.

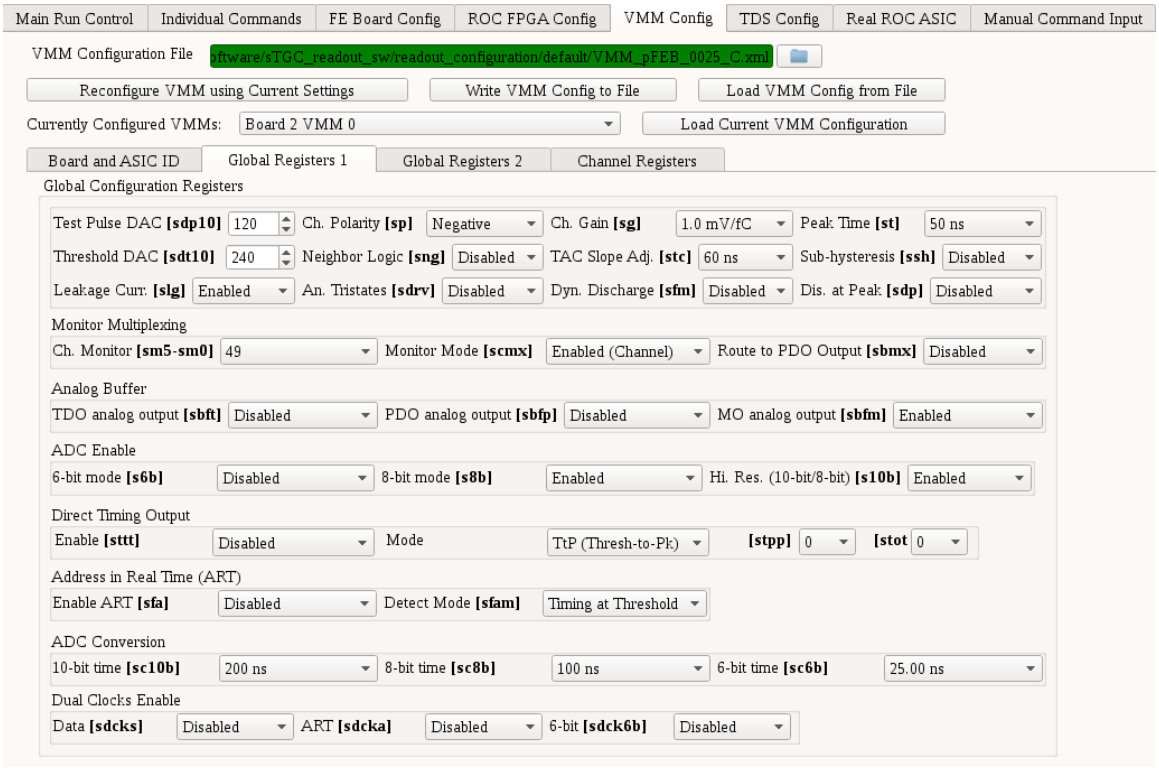

Figure 3.11: A screenshot of the DAQ software used in the test beam [19]. From this menu, the individual VMMs can be configured. This includes setting thresholds, changing analog outputs, and sending test pulses.

Chapter 4

sTGC Test Beams

In order to thoroughly understand the sTGC detectors described in Chapter 3, it is important to rigorously test the chambers in a variety of settings. During construction, the chambers pass numerous quality control tests to check for short circuits, gas leaks, and other potential issues. Once completely assembled, each quadruplet will spend time undergoing tests with cosmic rays. This process will be explained in Chapter 7.

A few select chambers have been tested in muon beams at CERN. In particular, a QS3 quadruplet was tested at CERN during the fall of 2018. The process and methods of testing the detector will be explained in this chapter. I will begin by outlining the objectives of the test beam, and will continue with a description of the specific detector used in the tests. This will be followed by a description of the experimental area and the setup employed in the tests. The chapter will conclude with a summary of the data that was collected. It is important to note that this work was carried out by a team of individuals from throughout the sTGC collaboration.

4.1 Objectives

The fall 2018 sTGC test beam of the QS3 quadruplet had a large collection of objectives that the collaboration wished to accomplish. The objectives of the tests that I personally worked on are shown below:

- Measure the efficiency and multiplicity of the pads and wires of each layer.
- Observe the Peak Detector Output (PDO) and Time of Detector Output (TDO) profiles for pads and wires.

- Observe the beam profile in the wires.
- Measure the 3-out-of-4 coincidence efficiency in the pads.

The efficiency of a detector element is defined as the percentage of particles that pass through the detector element that are detected. For example, if 1000 muons pass through a layer of pads, and 967 muons are detected by the layer, the pads have an efficiency of 96.7%. This same definition applies to the strips and wires. Multiplicity is defined as the number of channels of a detector element that produce a signal due to the passage of a single particle. If a single muon traverses an sTGC layer and four pads produce a signal, then that event has a multiplicity of four. Because the trigger system of the sTGCs uses 3-out-of-4 coincidences, it is necessary to test the 3-out-of-4 efficiency in particular. A 3-out-of-4 coincidence in the pads is defined as at least 3 layers of the pads producing a signal from the passage of a single particle.

The Peak Detector Output (PDO) is a measure of the amplitude of the pulse detected by a channel of the VMM. The PDO is proportional to the energy deposited by the passing particle. The average energy loss of a particle traversing matter is modeled by the Bethe-Bloch equation. The spectrum of energy deposited by a monochromatic particle beam traversing a gaseous layer is modeled by a Landau distribution. Thus, we expect that the PDO profile should follow a Landau distribution. Because the beam has a diameter on the order of ten centimeters, the detector should be able to observe the beam profile in the strips and wires. This should present itself as an approximately Gaussian distribution centered on one channel, with adjacent channels having decreasing numbers of events.

4.2 The QS3.P.1 Detector

The quadruplet used in the test beams was produced in Canada at TRIUMF and Carleton University. Its serial number is QS3.P.1, and it is a fully functional production quadruplet. It will be assembled into an sTGC wedge and will be implemented in the first NSW to be placed in ATLAS. The quadruplet was outfitted with a full set of Version 2.1 FEBs - four pFEBs and four sFEBs. Three of the four pFEBs had π-networks installed for the pad channels, while one did not. Each pFEB outfitted with a π-network had a 100 pF capacitor. The pFEB without the π-network was placed on layer 3 of the detector. Furthermore, each FEB had several small cooling fans mounted over them. Room temperature air was blown over the FPGA, FEAST

and VMMs of each FEB in order to prevent overheating. Several of the components on the FEBs are prone to overheating, which can lead to electronic failure and a shortened lifetime for the board. Though the fans were a necessary addition to prevent overheating during the test beam, they will not be used in ATLAS. A more sophisticated water cooling system has been developed and will more efficiently cool the FEBs during their service in the NSW. Data was collected through the miniDAQ system described in Section 3.6.5.

4.3 The H8 Beamline and the Experimental Area

The 2018 test beams of the QS3 quadruplet took place on the H8 beamline of the Super Proton Synchrotron (SPS). The SPS is the final accelerator before the LHC, accelerating protons from an initial energy of 25 GeV to a final energy of 450 GeV. These protons are either injected into the LHC to be ramped to higher energy or split off to other experimental areas. The H8 beamline resides in Building 887 of the CERN Prévessin site. The proton beam is capable of producing secondary beams from fixed targets. These secondary beams consist of muons, electrons or mixed hadrons, ranging in energy from 10 GeV to 400 GeV. The sTGC test was located at H8C, one of the downstream test stations. Two other stations were upstream of our experimental area. The most upstream user dictates the beam composition and intensity. Immediately upstream of the H8C area is a section of shielding that can be moved to prevent hadrons and electrons from reaching the H8C area [26].

H8C consists of a large concrete platform over which the beam passes. The beam passing through H8C is in open air and does not require a vacuum beam-pipe. The concrete platform is at a height such that detectors can easily be placed into the beamline. The platform is outfitted with a hydraulic stage on which detectors can be placed, which allows for precise positioning in the plane transverse to the beam axis. A plastic scintillator is placed on each end of the platform to allow for triggering. The H8C area can be seen in Figure 4.1.

4.4 Experimental Setup in H8

During the test beam, the quadruplet was placed on either the hydraulic stage or on the ground in front of it. While placed on the stage, the detector was elevated such that the beam passed through the bottom half of the detector, as seen in Figure 4.1.

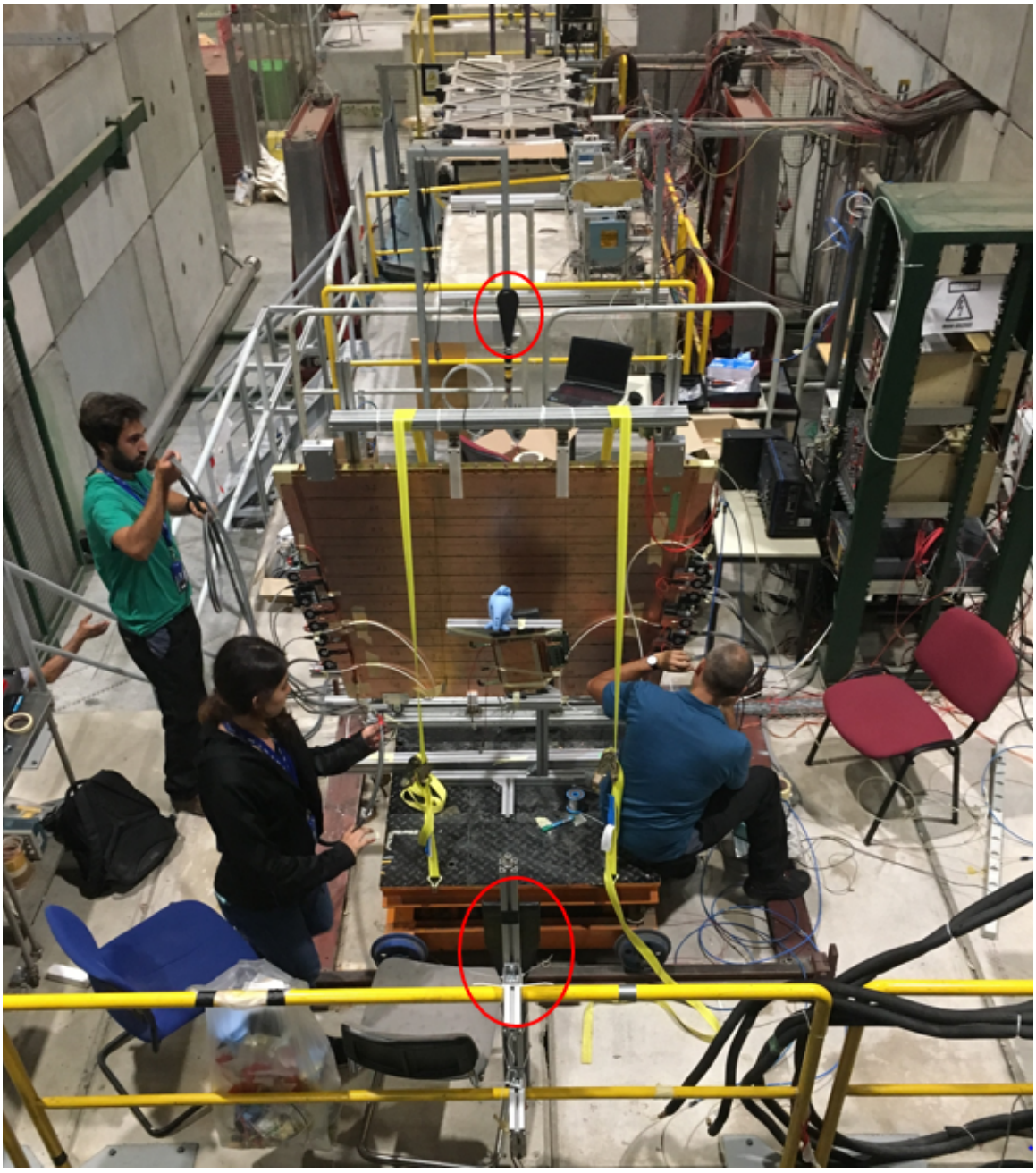

Figure 4.1: A picture of the H8C test beam area. The quadruplet is resting on the hydraulic stage (orange and black). The two scintillators are circled in red.

If placed on the ground, the beam would pass through the top half of the detector. A gas flow system located on the catwalk adjacent to the experimental area provided the proper n-pentane / CO_2 mixture to the detector. The n-pentane supply was placed in a chiller to keep it at the proper temperature and to regulate the proportions of the gas mixture. The gas is heated slightly as it moves from the supply to the detector, so that the n-pentane does not condense inside of the detector. If the temperature inside the detector falls below 17°C, there is a risk that the n-pentane in the mixture can condense into its liquid state inside of the detector, which can cause issues such as short circuits. The gas system is also capable of running purely CO_2, which can be used to flush the detector.

Five low voltage power supplies were employed in the setup. One of the power supplies was used to power the fans used to cool the FEBs, while the other four provided power to the FEBs. Each layer of the detector (one pFEB and one sFEB) was powered by a single power supply. A Nuclear Instrumentation Module (NIM) rack was placed in the area to provide the external electronics needed for the tests. NIM is an electronics standard commonly used in nuclear and particle physics experiments. A NIM rack provides power to an array of interchangeable modules through a standard power connector on the backplane of the rack. This allows for the easy movement and organization of a variety of useful modules. A CAEN N1470B 4-Channel High Voltage Power Supply module was used to provide high voltage to all four of the layers.

The trigger setup employed four plastic scintillators - the two on the ends of the H8C platform and two that were mounted immediately on each side of the detector. The four scintillators were placed in the beamline such that they could produce coincidence signals. The scintillators adjacent to the detector each had an active area of 4 cm x 12 cm. One of the scintillators was oriented horizontally while the other was oriented vertically. This provided an overlap area of 4 cm x 4 cm, giving a coincidence area of 16 cm^2. This small coincidence area was used to localize the large diameter of the beam into a small trigger area of one or two pads per layer. The signals of the four scintillators were routed into a coincidence module on the NIM rack that would detect if all four scintillators produced a signal within a given time window. If a coincidence was detected, a trigger signal would be sent to the miniDAQ system and the detector would be read out.

Prior to being sent to the miniDAQ, the trigger signal would be split, with one path leading to the miniDAQ and the other leading to an unused channel on the layer

4 strip adapter board. This connection to the strip adapter board injects a signal into the layer 4 sFEB that can be used as a timing reference. This signal will be registered by the sFEB and will be readout when the miniDAQ receives the trigger signal. Because this signal is being injected into a channel that is not connected to a strip on the detector, the trigger signal is the only possible event that can occur on that channel. Noise or cosmic muons cannot provide a signal into that channel. Thus, when analyzing the data, the events on this channel can be used as a timing reference. The timing reference is necessary because of the issues discussed in Section 3.6.4. With the BCIDs of individual VMMs being offset from each other, the trigger timing injection can be used to identify events that are associated with an individual trigger signal. The analysis to identify which events are associated with a trigger will be detailed in Chapter 5.

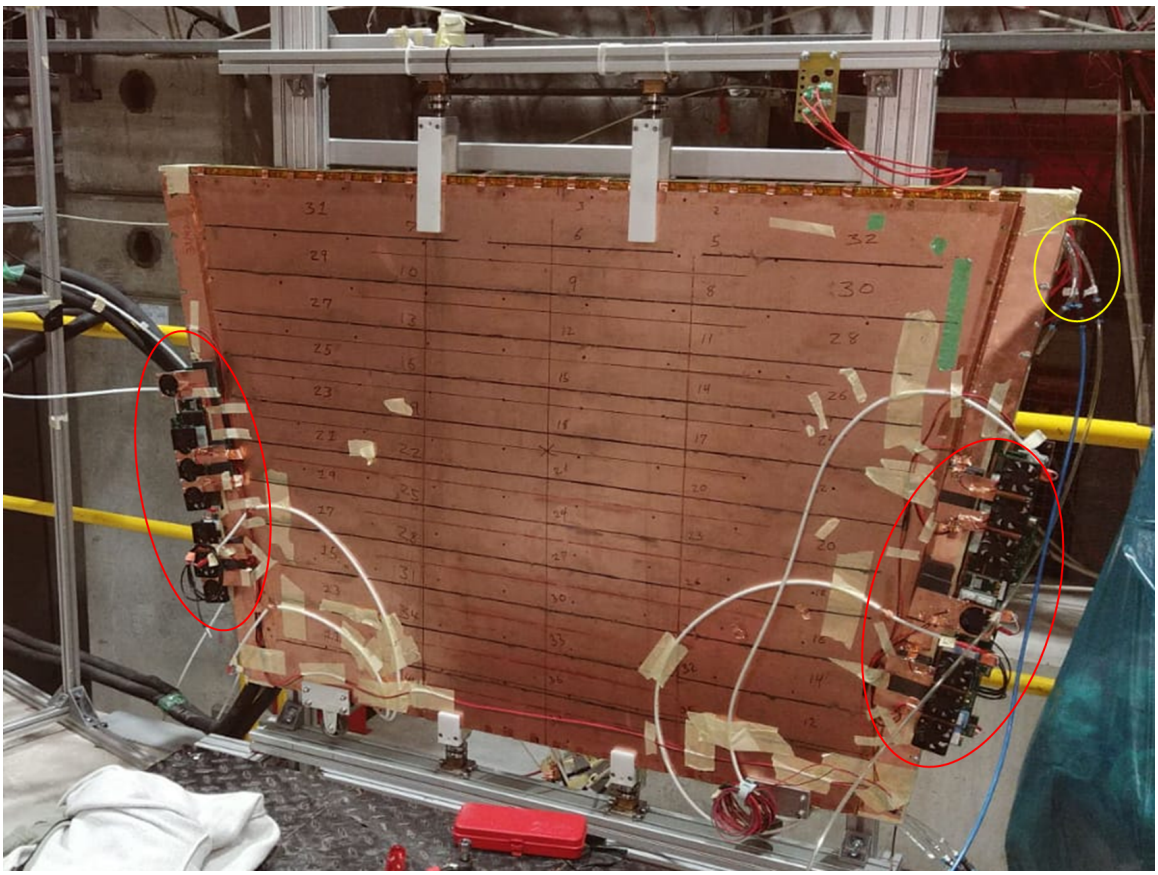

Figure 4.2: A picture of the test beam setup in the H8 beamline. The fans that cool the pFEBs and sFEBs are circled in red, and the gas connections for the detector are circled in yellow.

4.5 Data Collected

There were three main periods during which data was collected with the QS3 detector. The first was in early August, during which the detector collected data in the H8C area. Following that period, the detector spent time in the Gamma Irradiation Facility (GIF++) and collected data under a high photon background[1]. During both of these periods, the data that was collected was primarily used for diagnostic purposes. High levels of noise affected the detector and made much of the data unusable. Thresholds needed to be fine tuned to prevent noise from flooding the miniDAQ and crashing it. Furthermore, a solution to the timing issues of the VMM was not developed until late in the GIF++ test period. Improvements to the grounding scheme of the detector and the fine tuning of individual channel thresholds that were made after the GIF++ test period allowed the detector to collect data without crashing the DAQ system, and the timing injection allowed for a proper analysis of the data. The final testing period took place in H8C again with all of the stated improvements. The data taken during this period is the data that I have analyzed and will be presented in this thesis. All of the data taken has been stored on CERN's LXPLUS cluster under the file path /eos/atlas/atlascerngroupdisk/det-nsw-stgc/QS3_testbeam_GIF/QS3_data. Individual run data is stored there in subdirectories.

There are four runs that will be analyzed in Chapter 5. Each run was collected during the final beam period in H8C. During these runs, the beam provided 150 $\frac{GeV}{c}$ muons at a rate of approximately 200-400 particles per minute. The run numbers, along with their corresponding conditions, are shown in Table 4.1.

Run Number	Voltage (kV)	Strip Gain ($\frac{mV}{fC}$)	Wires Gain ($\frac{mV}{fC}$)	Pads Gain ($\frac{mV}{fC}$)	Triggers
43	2.9	1	1	3	75808
44	3.0	1	1	3	40024
45	3.1	1	1	3	60035
46	2.8	1	1	3	60019

Table 4.1: A table of the data runs that will be analyzed in Chapter 5.

[1]For more information on GIF++, please see the presentation by Roberto Guida [27].

Chapter 5

Test Beam Results

The test beam periods described in Chapter 4 produced a large amount of data that could be used to characterize the performance of the sTGC detector. In particular, the analysis focused on obtaining answers to the objectives listed in Section 4.1 through the data shown in Table 4.1. The analysis produced many successful results, including:

- A measurement of the efficiency, multiplicity, and peak detector output of the pads for layers 1 and 2.
- A measurement of the efficiency, multiplicity and peak detector output of the wires for layers 1 and 2.
- A measurement of the efficiency, multiplicity and peak detector output of the strips.
- Observation of the beam profile in the strips and wires.

This chapter will present the results of the measurements for the pads and wires, as these are the results that were produced from my analysis.

The chapter will begin with an explanation of the usage of the timing injection method described in Chapter 4. This will be followed by a description of the code structure and the analysis methods. Finally, the results of the test beam measurements will be presented and discussed, with the final section detailing the uncertainties involved in the analysis.

5.1 Timing

As described in Sections 3.6.4, the FEBs used in these tests did not have synchronized bunch crossing identification (BCID) clocks. This lack of synchronization means that there is no way to group hits across many VMMs together without the use of an external reference. To overcome this issue, the trigger timing injection discussed in Section 4.4 was implemented. This trigger timing injection is a coincidence signal from the trigger scintillators that is injected directly into an unused channel of the layer 4 strip adapter board. This signal is registered by the layer 4 sFEB, which records the BCID of the trigger.

The BCID of the trigger injection was used as a reference time for each event. Because the BCID clock on each VMM runs at the same rate, although unsynchronized, the BCID clock of a VMM has a constant offset relative to another VMM. In order to determine this constant offset, an analysis was run with the following steps:

1. For each trigger, identify the BCID value of the trigger injection.
2. For each signal that occurs during this trigger window, calculate the difference in BCID between the signal and the trigger injection. This value will be known as dBCID[1].
3. For each VMM, place the values of dBCID into a histogram. An example is shown in Figure 5.1.

This analysis was run using a Python script that looped through every trigger signal. The result of this analysis is a histogram for each VMM showing the dBCID value of every signal that occurred on that VMM relative to the corresponding trigger signal. Any signal that corresponds to a trigger particle should occur in a short time window after the trigger signal was detected. Because the trigger signal is only generated by particles traversing the trigger scintillators, and the BCID offset between VMMs is constant, it should be the case that the histogram has a large peak at the offset value corresponding to the events from the trigger particle. Any signals that have a dBCID value far from the peak must be generated by something other than the particle that caused the trigger. Figure 5.1 shows a histogram of the number of

[1]It is important to note that the values of BCID range from 0 to 4095. The values repeat themselves, so once the BCID clock reaches 4095, the next value of BCID will be zero. To ensure that the values of dBCID are always positive, negative values of dBCID have 4096 added to them.

signals that occurred for each value of the dBCID for the pads of layer 1. A sharp peak can be seen in the top plot of Figure 5.1 at a dBCID value of approximately 3800. Zooming in on this peak in Figure 5.1, it can be seen that the peak rises quickly to a maximum at a dBCID value of 3828 before falling off drastically. From this, it can be determined that the offset of this VMM relative to the timing injection is 3828 BCIDs. Almost all events that are not within ±1 BCID of this peak are not related to the particle that caused the trigger and can thus be disregarded. Knowing the dBCID offset provides a useful cut to apply to the data. If the analysis requires that the dBCID value of a signal be within 1 BCID of the peak, it removes many signals caused by sources other than the trigger particle from the sample. This criterion will serve as the primary way to separate trigger particle signals from signals caused by other sources in this analysis.

5.2 Analysis Methods

The analysis of the data presented in this thesis was done through numerous Python scripts. These Python scripts implement the PyROOT module for accessing the data and for creating histograms. ROOT is a data analysis framework developed at CERN for particle physics analyses. It is a collection of C++ libraries and classes. PyROOT is an extension to Python that allows this collection of libraries and classes to be used with Python [28]. Each analysis script operates in a similar fashion. They each begin by accessing the data for a given run. This data is stored in a ROOT TTree object. The script then proceeds to loop through every event in the data, with each event corresponding to an individual trigger signal. Each trigger event contains many different signals that were read out during the trigger window. Each of these signals will be referred to as a "hit". For each event, arrays are created that store the FEB number, VMM number, channel number, PDO, TDO, and BCID of the individual hits. After populating these arrays, the script loops through the hits to find the signal that belongs to the trigger injection[2]. It records the BCID of the injection signal before moving on.

Once the trigger BCID has been identified. All of the hits are looped through again. In this loop, the script checks to see if the dBCID value of each hit is within 1 BCID of the offset determined by the timing analysis. If the hit does not meet this

[2]The injection was always on the same channel - sFEB layer 4, VMM 7, Channel 62.

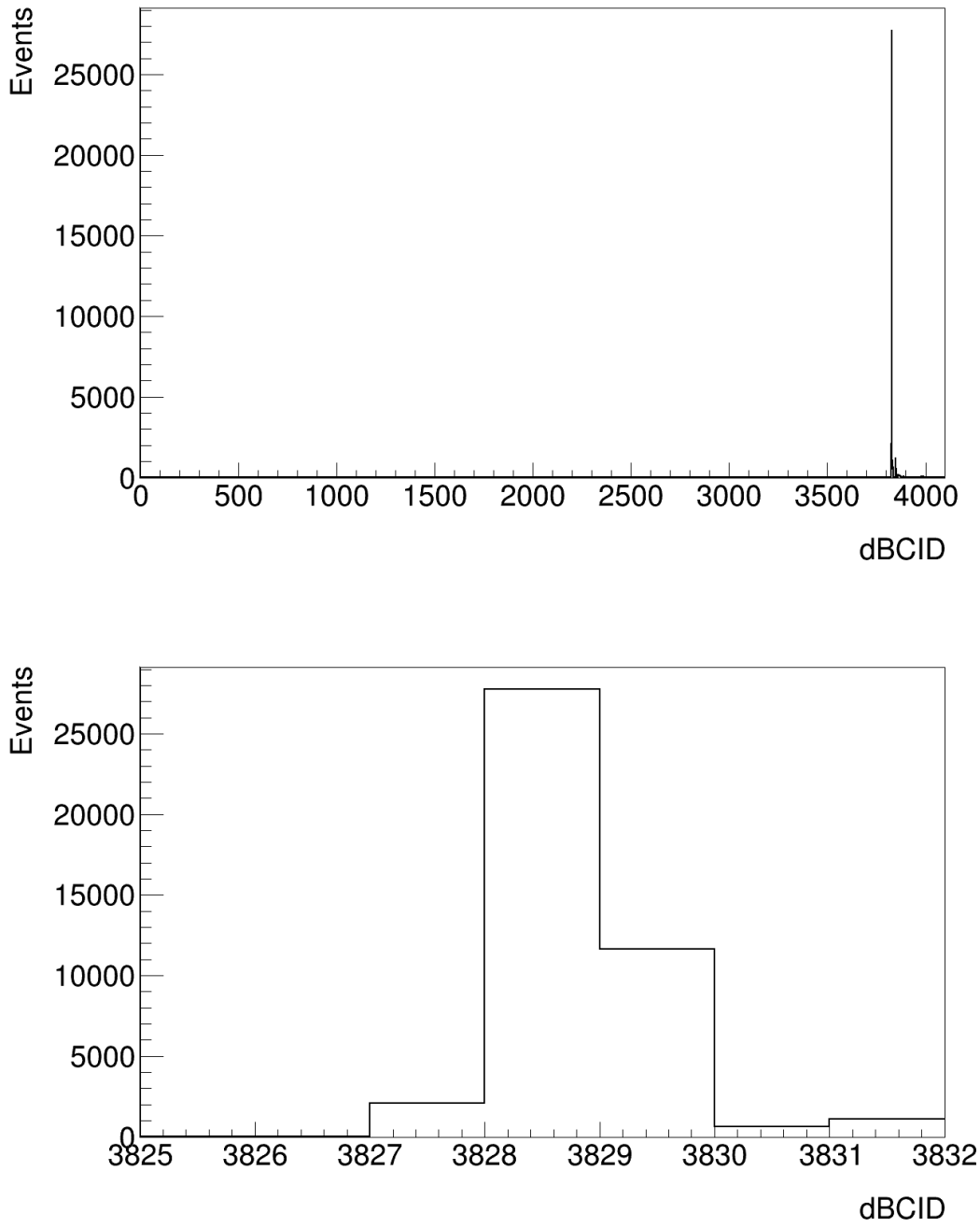

Figure 5.1: The top plot shows the distribution of the difference of the BCID of the pad signal and the BCID of the trigger time injection. The bottom plot shows a zoomed in view of the peak of the distribution.

criteria, then it is ignored and not included in the analysis. If the hit did occur in the proper time window, the point is then analyzed according to the particular analysis.

5.3 Pad Measurements

Three measurements were successfully made regarding the performance of the pads. Efficiency and multiplicity values were determined for four potential operating voltages of the detector, and the peak detector output distribution was measured for the same four voltages.

The data that was collected only includes readout from three layers of pads. Layer 3 was not read out during the beam test due to high noise levels. The level of noise present on layer 3 made it impossible to collect meaningful signals because the individual thresholds of the channels had to be raised significantly in order to not be exceeded by the noise fluctuations. With the thresholds set so high, most signals would not be measured, so the decision was made to not read out layer 3. Similar noise issues affected layer 4, but data was collected for the layer 4 pads. An analysis of the effects of the electronic noise is presented in Section 5.5. Because layer 3 was not used and layer 4 was severely limited, the data was unable to provide a measurement of the 3-out-of-4 efficiency mentioned in Section 4.1. There was also not enough time to change out the capacitors on the boards with the π-network, so a comparison of different π-network capacitance values did not take place[3].

5.3.1 Efficiency

The efficiency of a layer of pads is defined as the number of muons detected by the layer divided by the number of muons that passed through that layer. The efficiency results shown here are calculated with respect to the trigger signal, meaning that the number of particles that pass through the detector is determined by the number of trigger signals produced from the coincidence between the trigger scintillators. The efficiency of a layer is calculated according to the equation

$$\epsilon = \frac{T_{Detected}}{T}, \tag{5.1}$$

[3]The capacitors on the board had to be changed by hand, and required many hours of time in the electronics shop to change.

Voltage (kV)	Layer 1 ϵ	Layer 2 ϵ	Layer 3 ϵ	Layer 4 ϵ
2.8	81.9% ± 0.1%	83.0% ± 0.1%	-	5.9% ± 0.1%
2.9	94.3% ± 0.1%	97.2% ± 0.1%	-	10.2% ± 0.1%
3.0	96.8% ± 0.1%	98.4% ± 0.1%	-	18.0% ± 0.1%
3.1	96.7% ± 0.1%	97.6% ± 0.1%	-	33.7% ± 0.1%

Table 5.1: A table of pad efficiency measurements for the tested operating voltages. The uncertainties come from the electronic noise analysis presented in Section 5.5.

where T is the number of triggers for the run and $T_{Detected}$ is the number of triggers on which one or more signals were detected for the given layer.

The efficiencies of each layer at the four different voltages are shown in Table 5.1. Overall, the efficiency of each layer tends to increase as the voltage increases from 2.8 kV to 3.0 kV. The efficiency continues to increase for layer 4 at 3.1 kV, while layer 1 and 2 experience slight drops in efficiency. The difference between the efficiency at 3.0 and 3.1 kV for layer 1 is zero within uncertainty, but the layer 2 efficiency does decrease by a noticeable amount. Recalling the performance requirements laid out in Chapter 3, an efficiency of 96.5% is desired in each individual layer. Layers 1 and 2 meet this goal at operating voltages of 3.0 and 3.1 kV. Although the desired operating voltage is 2.8 kV, it is possible to operate the detectors at 3.0 kV in ATLAS. This increase may lead to a decreased lifetime of the detector.

5.3.2 Multiplicity

The multiplicity of an event is defined as the number of channels in a single layer that produce a signal due to the passage of a single particle. If a muon traverses layer 1 of the detector, and four pads register a signal, that event has a multiplicity of 4. Events with high multiplicity are not ideal for the trigger system of the detector. The pad sizes of the different layers of an sTGC are not identical. They are offset from each other such that their intersections form smaller "logical pads." These logical pads are important in the trigger, as they localize the regions of interest for the detector to readout. If an event triggers multiple pads, the trigger cannot localize the region of interest as well and the detector is forced to read out more channels than necessary. Thus, it is ideal for the pads of the detector to have high efficiency but low multiplicity. The average multiplicity of the detector is given by

Voltage (kV)	Layer 1 Average	Layer 2 Average	Layer 3 Average	Layer 4 Average
2.8	1.06 ± <.01	1.06 ± <.01	-	1.21 ± <.01
2.9	1.06 ± <.01	1.06 ± <.01	-	1.21 ± <.01
3.0	1.06 ± <.01	1.06 ± <.01	-	1.13 ± <.01
3.1	1.06 ± <.01	1.05 ± <.01	-	1.08 ± <.01

Table 5.2: A table of the average pad multiplicity for the tested operating voltages. The uncertainties come from the electronic noise analysis presented in Section 5.5.

Voltage (kV)	Layer 1 % > 1	Layer 2 % > 1	Layer 3 % > 1	Layer 4 % > 1
2.8	6.0%	5.9%	-	19.6%
2.9	5.9%	5.9%	-	18.7%
3.0	5.7%	5.7%	-	11.6%
3.1	5.5%	5.4%	-	7.8%

Table 5.3: A table of the percentage of events with a multiplicity greater than 1 for the tested operating voltages.

$$M_{Ave} = \frac{1}{T_{Detected}} \sum_{M=1}^{M_{Max}} M \cdot N_M = \frac{N_{Total}}{T_{Detected}}, \tag{5.2}$$

where $T_{Detected}$ is the number of triggers with one or more signals detected by the layer, M is the multiplicity, M_{Max} is the maximum observed multiplicity, and N_M is the number of events with multiplicity M. The summation term amounts to the total number of signals detected by the layer during the run, N_{Total}.

A sample plot of the multiplicity is shown in Figure 5.2, and the results of the analysis are shown in Tables 5.2 and 5.3. Table 5.2 shows the average multiplicity of events for each layer at a given voltage, and Table 5.3 shows the percentage of events that have a multiplicity greater than 1 for each tested voltage. For layers 1 and 2, Table 5.2 shows that the average value of the multiplicity did not change significantly as the voltage of the detector was increased. However, the average value of layer 4 decreased noticeably as the operating voltage was increased. This is also reflected in Table 5.3, where the percentage of events with a multiplicity greater than 1 was reduced by more than half by the increase from 2.8 to 3.1 kV. Layers 1 and 2 both exhibit an acceptable level of multiplicity at all operating voltages, with no more than 6% of events causing multiple pad signals.

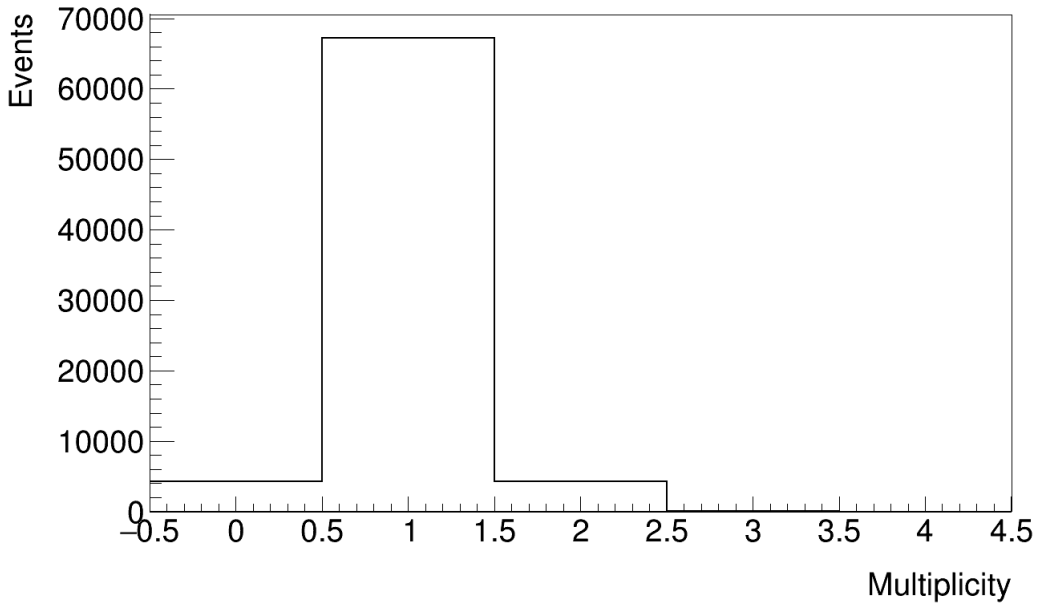

Figure 5.2: A plot showing the multiplicity of the layer 1 pads at 2.9 kV.

Voltage (kV)	Layer 1 MPV	Layer 2 MPV	Layer 3 MPV	Layer 4 MPV
2.8	122.2 ± 0.1	109.6 ± 0.1	-	164.7 ± 1.2
2.9	143 ± 0.2	128.4 ± 0.1	-	159.6 ± 0.9
3.0	179.1 ± 0.3	163.1 ± 0.3	-	145.7 ± 0.5
3.1	227.3 ± 0.4	207.2 ± 0.3	-	142.8 ± 0.3

Table 5.4: A table showing the most probable value (MPV) of the pads PDO for each layer for the tested voltages in ADC units. The uncertainties come from the Landau fit of the data.

5.3.3 PDO

The peak detector output (PDO) is a measurement of the amplitude of a signal received by the FEBs. When the signal reaches the VMM, its amplitude is measured and then digitized on a scale from 0 to 1023. The PDO is effectively a measurement of the energy deposited by the passing particle. As discussed in Chapter 4, the distribution of energy deposited by a monoenergetic beam of particles should follow a Landau distribution. It is thus expected that the PDO profile of the pads should follow a Landau distribution. Landau distributions have long high-energy tails, which will cause some muons to deposit very large amounts of energy into the detector. Because the PDO value is digitized and has a maximum value of 1023, some particles will deposit energy beyond this range. The VMM will interpret these saturated events as having a PDO of 1023. Because the long tail of the distribution extends past 1023, all of the events with a PDO greater than 1023 should accumulate at 1023, leaving a saturation peak at a PDO value of 1023.

Figure 5.3 shows the PDO distribution of a pad in layer 1 at a voltage of 2.9 kV. The plot is fit with a Landau distribution. This plot exhibits all of the expected characteristics. The long high-energy tail is present, as well as the expected saturation peak. The results of the analysis are summarized in Table 5.4, where the most probable values (MPVs) of the fit are listed. For layers 1 and 2, the MPV increased as the voltage was increased, effectively shifting the distribution to the right on Figure 5.3. This behavior is also expected, as the increase in voltage causes larger electron avalanches, thus producing larger signals on average.

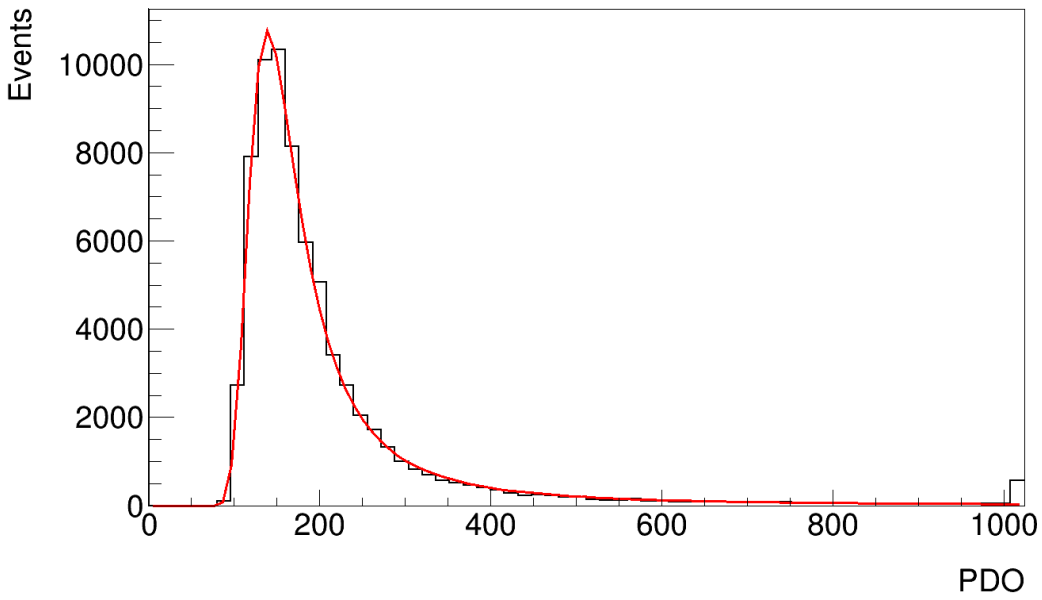

Figure 5.3: A plot showing the peak detector output of a layer 1 pad at 2.9 kV.

Voltage (kV)	Layer 1 ϵ	Layer 2 ϵ
2.8	96.6% ± 0.1%	98.1% ± 0.1%
2.9	98.3% ± 0.1%	99.8% ± 0.1%
3.0	98.7% ± 0.1%	99.9% ± 0.1%
3.1	98.7% ± 0.1%	99.8% ± 0.1%

Table 5.5: A table of wire efficiency measurements for the tested operating voltages. The uncertainties come from the electronic noise analysis presented in Section 5.5.

5.4 Wire Measurements

Measurements of the efficiency, multiplicity and PDO profile of the layer 1 and 2 wires were successfully completed with the data from the test beam. The beam profile was also observed by the wires of layers 1 and 2. The data produced by layer 3 and 4 was unable to be analyzed due to an issue with the firmware on the layer 3 and 4 pFEBs. On those pFEBs, the VMMs responsible for reading out the wires data were version VMM3a. However, the firmware that was installed on those VMMs was for VMM3. When the raw data output by the VMMs is decoded by the decoding software, it must interpret the bits in a particular predefined order. The VMM3 firmware outputs those bits in the reverse order from VMM3a. Thus, the data from layers 3 and 4 was unable to be decoded with the current decoding software. The raw data does exist however, and could potentially be decoded and analyzed at a later date. In order to avoid high levels of noise, only five wire channels were read out on both layer 1 and layer 2. The remaining channels were masked.

5.4.1 Efficiency

The efficiency of a layer of wires is defined in the same manner as the efficiency of a layer of pads; the efficiency is the fraction of trigger signals that have at least one wires channel producing a signal in the layer.

The results of the efficiency analysis are shown in Table 5.5. The data in Table 5.5 shows that both layers exhibit efficiencies greater than 96% for all of the tested operating voltages. The increase in operating voltage from 2.8 kV to 2.9 kV results in a significant increase in wire efficiency, but no further major increases are observed with increases in wire potential. The efficiencies observed by the wires at 2.9 kV are excellent for both layers and meet the requirements of the NSW.

5.4.2 Multiplicity and Beam Profile

The multiplicity of the wires is defined in an identical manner as it is for the pads. For this data, the maximum possible multiplicity is five, because only five wire channels were open during the run. If the multiplicity of an event is five, then all of the channels are producing a signal. Figure 5.4 shows a plot of the multiplicity for the layer 1 wires at 2.9 kV, and Table 5.6 summarizes the results of the test. In general, it is seen that the multiplicity tends to increase as the operating voltage of the chamber is increased. This is the expected behavior, as the number of electrons freed should increase with the operating voltage. This in turn leads to more channels producing signals over the threshold. These increases in multiplicity are small overall, and the overall level of multiplicity is reasonable. Each wire group of 20 wires covers 3.6 cm, so it is expected that the average muon would only produce a signal on one or two channels.

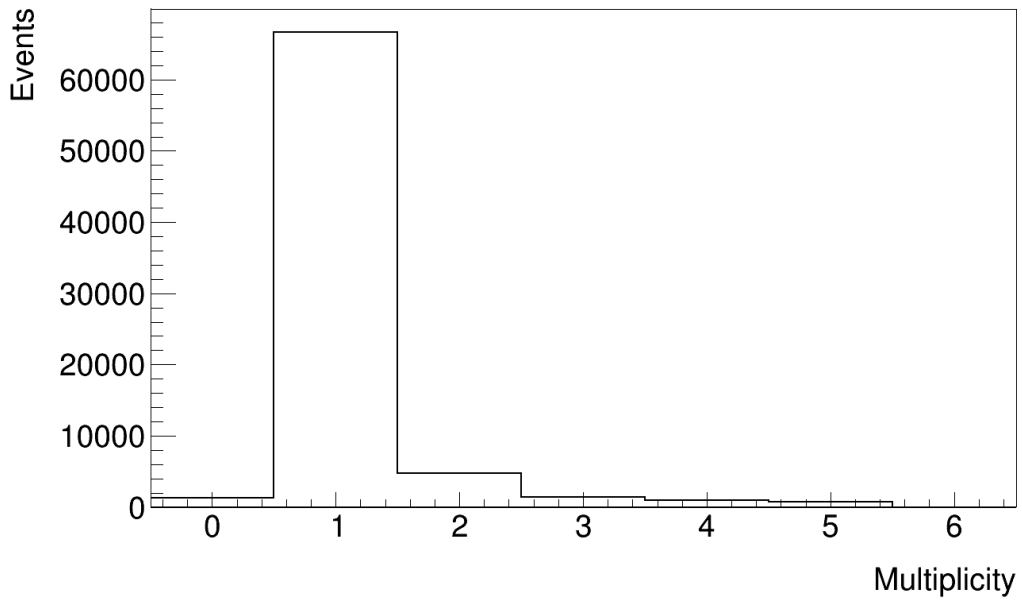

Figure 5.4: A plot showing the multiplicity of the layer 1 wires at 2.9 kV.

The beam profile observed by the layer 1 wires at 2.9 kV is shown in Figure 5.5. The beam profile did not change significantly with the operating voltage, and the profiles seen by layers 1 and 2 match well. This beam profile is also consistent with the results of the multiplicity analysis. The highest multiplicity observed was five, and the beam profile spans five channels. It is possible that both the beam profile

Voltage (kV)	Layer 1 Average	Layer 2 Average	Layer 1 % > 1	Layer 2 % > 1
2.8	1.161 ± <.001	1.154 ± <.001	9.8%	9.5%
2.9	1.181 ± <.001	1.167 ± <.001	10.6%	10.0%
3.0	1.184 ± <.001	1.163 ± <.001	11.0%	10.0%
3.1	1.213 ± <.001	1.179 ± <.001	12.3%	10.6%

Table 5.6: A table of the average wire multiplicities and the percentage of events with a multiplicity greater than 1 for layers 1 and 2. The uncertainties come from the electronic noise analysis presented in Section 5.5.

and multiplicity could have covered more channels because only five channels were open.

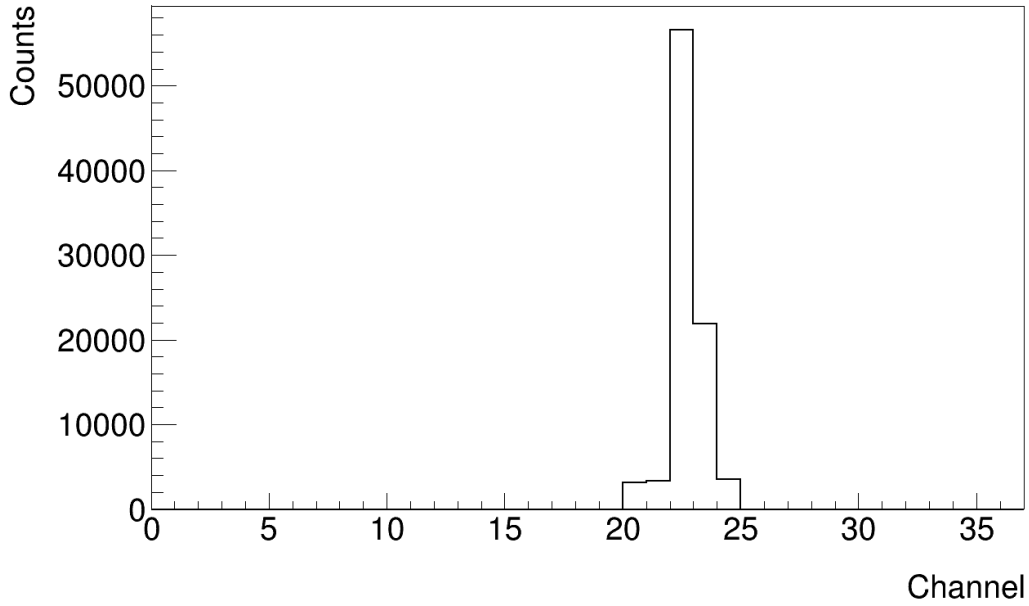

Figure 5.5: A plot showing the beam profile observed by the layer 1 wires at 2.9 kV.

5.4.3 PDO

The PDO of the wires has the same expected Landau distribution as the pads. Figure 5.6 shows a plot of the PDO distribution of a layer 1 wires group operating at 2.9 kV, and Table 5.7 summarizes the most probable values of each layer at the tested operating voltages. The PDO distribution in Figure 5.6 exhibits all of the expected characteristics, including the long tail and the saturation peak at the PDO value of

Voltage (kV)	Layer 1 MPV	Layer 2 MPV
2.8	84.3 ± 0.1	83.1 ± 0.1
2.9	104.8 ± 0.1	102.2 ± 0.1
3.0	134.7 ± 0.3	131.5 ± 0.2
3.1	169.4 ± 0.3	166.4 ± 0.3

Table 5.7: A table showing the most probable value (MPV) of the wires PDO for each layer for the tested voltages in ADC units. The uncertainties come from the Landau fit of the data.

1023. The MPVs for the wires increase with respect to operating voltage, just as the MPVs for the pads did.

An additional characteristic that can be observed in the wires PDO distribution is the two distinct peaks which arise from impurities in the beam composition. The beam used for these tests was not a 100% pure muon beam. Instead, it carried different secondary particles with it that leave a second distinct PDO distribution. As the voltage is raised, the separation between the primary and secondary PDO distributions increases and the peak of the secondary distribution can be seen, as shown in Figure 5.7. This is due to the MPV of the distributions being increased with the voltage.

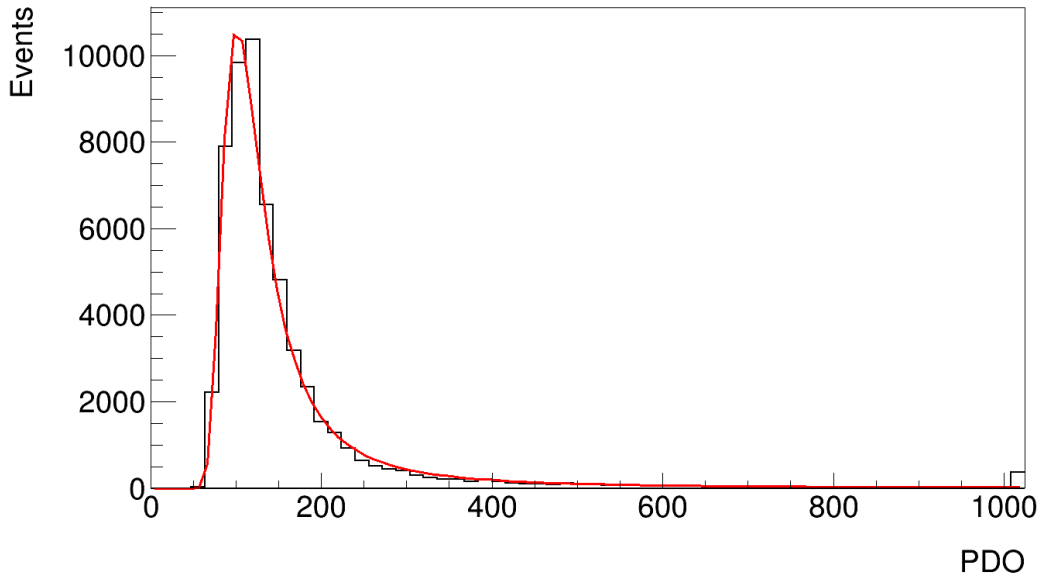

Figure 5.6: A plot showing the peak detector output of a layer 1 wire group at 2.9 kV.

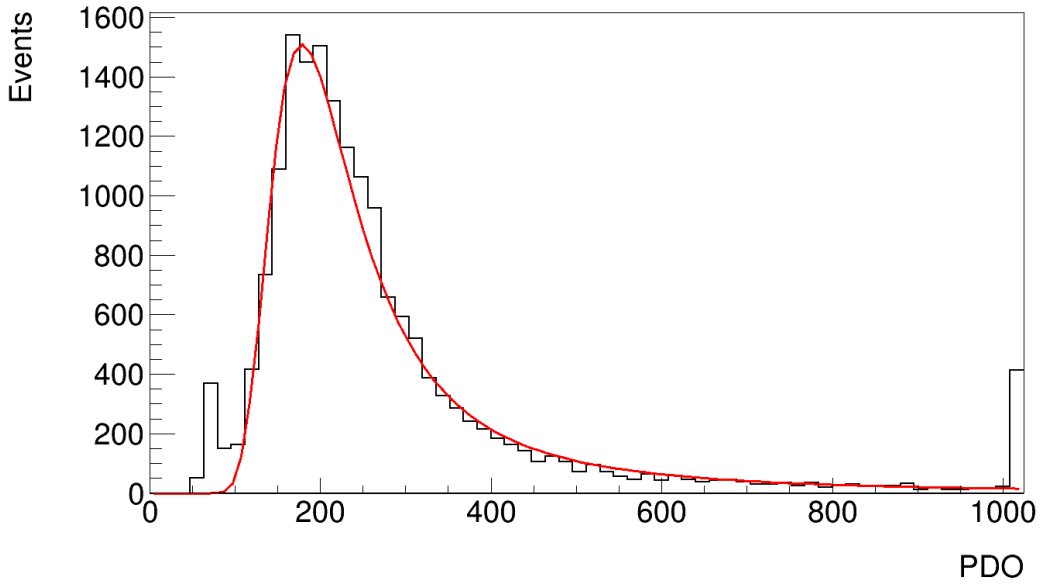

Figure 5.7: A plot demonstrating the two separate distributions of the beam constituents. The small peak on the left side of the distribution is a result of the beam impurities, where the secondary particles produce a secondary energy distribution.

5.5 Uncertainties

The primary uncertainties present in this data should arise from the presence of noise in the electronics of the detector. A spectral analysis of the noise across numerous channels showed that the dominant noise frequencies were 2 GHz, 4 GHz and 6 GHz. These correspond to the frequency of the FEAST DC-DC converter and its harmonics. For the runs that have been analyzed, the individual channel thresholds had been finely tuned to reduce the amount of events registered due to noise. To get an estimate on the number of events in each data set that come from detector noise, an analysis of the out-of-time data in the dBCID plots (Figure 5.1) was done. Because the dBCID cut only keeps the events from a window of three dBCIDs centered around the dBCID peak, the rest of the events on the plot can be considered out-of-time events resulting from noise and other background. If the average value of the remaining bins is taken, it can be used as an estimate for the number of background events that occurred during the in-time bins. Tables of those average values for the pads and wires are shown in Tables 5.8 and 5.9 respectively. Overall, the average number of background events per bin are very low for all layers. This is a result of the fine tuning of the thresholds. Because the dBCID cut window is three BCIDs wide, the number of background events present in the signal region should be approximately three times the average number of events. This value was used to calculate the uncertainty measurements for the efficiency and multiplicity.

For the efficiency measurements, if all of the background events correspond to triggers without a physical signal, then the uncertainty on the efficiency induced by the background is equal to

$$\Delta\epsilon = \frac{\Delta N_{Total}}{T}, \tag{5.3}$$

where ΔN_{Total} is the estimated number of background events and T is the total number of triggers. Similarly, the uncertainty in the average multiplicity is given by

$$\Delta M_{ave} = \frac{\Delta N_{Total}}{T_{Detected}}, \tag{5.4}$$

where $T_{Detected}$ is the number of triggers with a signal that was detected. The uncertainty on the most probable value of the PDO distributions comes from the fit of the Landau, where the uncertainty in the fit dominates the potential uncertainty from background events. The uncertainties are presented in their respective tables.

Voltage (kV)	Layer 1 Average	Layer 2 Average	Layer 3 Average	Layer 4 Average
2.8	8.8	3.5	-	3.7
2.9	13.6	4.6	-	5.0
3.0	7.7	3.2	-	2.9
3.1	13.7	6.4	-	5.2

Table 5.8: A table showing the average number of background events per dBCID bin for the pads at the tested voltages. The amount of events resulting from noise is very small compared to the number of events that were analyzed.

Voltage (kV)	Layer 1 Average Background	Layer 2 Average Background
2.8	2.9	3.9
2.9	4.0	5.6
3.0	2.3	3.4
3.1	4.2	5.8

Table 5.9: A table showing the average number of background events per dBCID bin for the wires at the tested voltages. The amount of events resulting from noise is very small compared to the number of events that were analyzed.

Chapter 6

sTGC Strip Alignment

The performance requirements for the New Small Wheel's tracking and triggering capabilities outlined in Chapter 3 require the sTGC detectors to provide precision measurements of particle positions and trajectories. While the sTGC technology is capable of providing the required position resolution, it is also necessary to precisely locate the individual detector elements relative to the ATLAS coordinate system. As such, a precision reconstruction of the individual strips in an sTGC cathode board is necessary to provide the desired functionality of the sTGC chambers. In order to do this, quality control (QC) measurements of each cathode board were taken. These QC measurements will be used to predict the as-built strip geometry of the strip boards. As a test of the relative alignment of layers, microscope pictures of the edges of doublets and quadruplets were taken at the construction sites.

This chapter will provide details of the sTGC detector geometry and lay out the quality control measurements that were taken of the sTGC cathode boards. It will then present a derivation of a function that will transform the nominal strip geometry of a cathode board to the as-built geometry based on the quality control measurements of the board. The procedure of the microscope pictures taken at the Carleton University construction site will also be detailed in this chapter, and a Python script that uses the as-built transformation function to construct predictions of as-built quadruplets will be outlined. This Python script will be used to compare the predicted relative misalignments of layers to the misalignments measured with the microscope pictures.

6.1 Detector Geometry

As detailed in Chapter 3, an individual sTGC layer consists of a layer of wires strung between two cathode boards, one of which is segmented into pads while the other is segmented into strips. Layers are then assembled into modules consisting of two and four layers, known as doublets and quadruplets, respectively. Each type of quadruplet is trapezoidal in shape except for the QL3 quadruplets, which resemble a trapezoid with a rectangle attached to the long end. That structure can be seen in Figures 3.3 and 3.4.

The strip cathode boards consist of hundreds of strips with a 3.2 mm pitch oriented in the ϕ-direction, nominally parallel to the parallel edges of the trapezoids. Each cathode board includes a single half-strip near either the long or short edge of the trapezoid. This is because the strip patterns of layer 1 and 3 cathode boards are offset from the patterns of layer 2 and 4 cathode boards by one half of a strip pitch[1]. This offset ensures that a muon passing orthogonal to the plane of the detector encounters no gaps in coverage.

Each cathode board has two machined brass alignment inserts that two precision alignment pins will rest against. The brass insert near the long edge of the trapezoid has a V-shaped notch for the pin, shown in Figure 3.8, while the insert near the short edge of the trapezoid has a flatter notch. The pin in the V-shaped notch provides a fixed point for the chamber to rotate about, while the pin in the flat notch blocks the rotation at a fixed point, constraining the rotational degree of freedom. These pins will be the only points referenceable by ATLAS' alignment system. With the short edge of the detector on top, the alignment inserts are on the right for 13 boards and on the left for 24 boards. When the layers are assembled into doublets, one of the layers is flipped over and stacked on top of the other, leaving the alignment features on the same side. In addition to the strips and brass inserts, the cathode boards also have small fiducial markers to be used as references. Some of the cathode boards also have additional blind holes that were added to simplify the QC measurement process.

[1]The layer 1 and 3 boards will be referred to from here on as 13 boards, and the layer 2 and 4 boards will be referred to as 24 boards.

6.2 Quality Control Measurements

Quality control measurements taken at the cathode board manufacturer can be used to reconstruct the positions of individual strips on each cathode board. The measurements taken by the manufacturer must be within certain tolerances for the cathode board to be accepted. If the board does not meet these tolerances, it will lead to degraded performance in the detector. The original tolerances for the strip boards were stringent. Due to manufacturing constraints and production deadlines, the original tolerances were relaxed so as to accept boards that were further from their nominal design. A table of the final tolerances is shown in Table 6.1. The decision to relax the tolerances was made with the understanding that the QC measurements would be used to correct for these nonconformities in software.

Board Type	QS1	QS2	QS3	QL1	QL2	QL3
Angle Tolerance	± 0.01°	± 0.005°	± 0.005°	± 0.01°	± 0.005°	± 0.005°
Offset Tolerance (μm)	± 300	± 300	± 300	± 300	± 300	± 300
Scale Tolerance (μm)	± 400	± 400	± 400	± 400	± 400	± 400
Nonparallelism Tolerance (μm)	± 400	± 400	± 400	± 400	± 400	± 400

Table 6.1: A table of the tolerances for the strip cathode board quality control measurements.

For each strip board, four QC measurements have been taken - scale, nonparallelism, angle and offset. These are shown in Figures 6.1, 6.2 and 6.3. The scale provides a measurement of the overall spreading or compression of the strip pattern. The nonparallelism quantifies how much the strips are diverging or converging relative to each other. The angle measurement shows how the strip pattern as a whole is inclined relative to the alignment pins. Finally, the offset measures the global shift in the strip pattern relative to the alignment pin in the V-notched brass.

6.2.1 Triangle Labs QC Measurements

The cathode boards used to produce the QS3 modules built at TRIUMF and Carleton were manufactured by Triangle Labs in Carson City, Nevada. The quality control measurements were done at Triangle Labs by TRIUMF personnel with a coordinate measuring machine (CMM). The CMM takes measurements of the board using a mechanical probe and provides a 3D coordinate for each measured point. Individual point measurements made with the CMM are accurate to approximately 20 μm.

The measurements made at Triangle Labs were made using five references - the center of the two alignment pins, and three strips. The first strip used in the QC measurements is the 6th full strip from the long edge of the detector, meaning that if the first strip is a half-strip then it is not counted. The 6th full strip is used because it is the strip closest to the edge that can be guaranteed to not intersect the brass alignment inserts for each size of strip board. The second strip used in the QC measurements is the 6th full strip from the short edge of the detector. The middle strip, located halfway between the other two strips, is used as the third reference strip[2]. For each of the three reference strips, the CMM takes a total of 20 measurements in order to properly reconstruct the centerline of the strip. 10 points are taken on the left edge of the board, with 5 points on the top side of the strip and 5 points on the bottom side of the strip. The same is done on the right edge of the board. A line of best fit is then drawn through the 20 points, and this line is used to make measurements. This method can be seen in the red points of Figure 6.1[3]. The other line used to make the QC measurements is a line drawn between the centers of the two alignment pins.

The offset measurement of the board is used to determine the global shift of the strip pattern relative to the center of the pin in the V-notched brass. This is done by extending the best fit line of the middle strip over the edge of the board and measuring the perpendicular distance between the best fit line and the center of the alignment pin. A diagram of the measurement method is shown in Figure 6.1[3].

For the angle measurement, the CMM calculates a line that goes between the center points of the two alignment pins. It then calculates the angle between the alignment pin line and the centerline of the Long Strip. That measurement can be seen in Figure 6.2[3].

The scale and nonparallelism measurements are each composed of two measurements that should nominally be the same. These two measurements, labeled d_1 and d_2 in Figure 6.3[3], are used to determine both the slope of the strips relative to each other, and the amount that the strip pattern as a whole has spread out. d_1 is a measurement of the perpendicular distance from the centerline of the Long Strip to the centerline of the Short Strip on the left side of the board, while d_2 does the same measurement on the right side of the board. The scale and nonparallelism parameters

[2]The 6th full strip from the long edge will be referred to as the "Long Strip" and the 6th full strip from the short edge will be referred to as the "Short Strip."

[3]Figures 6.1, 6.2 and 6.3 have been reproduced with the permission of Sergey Issinski.

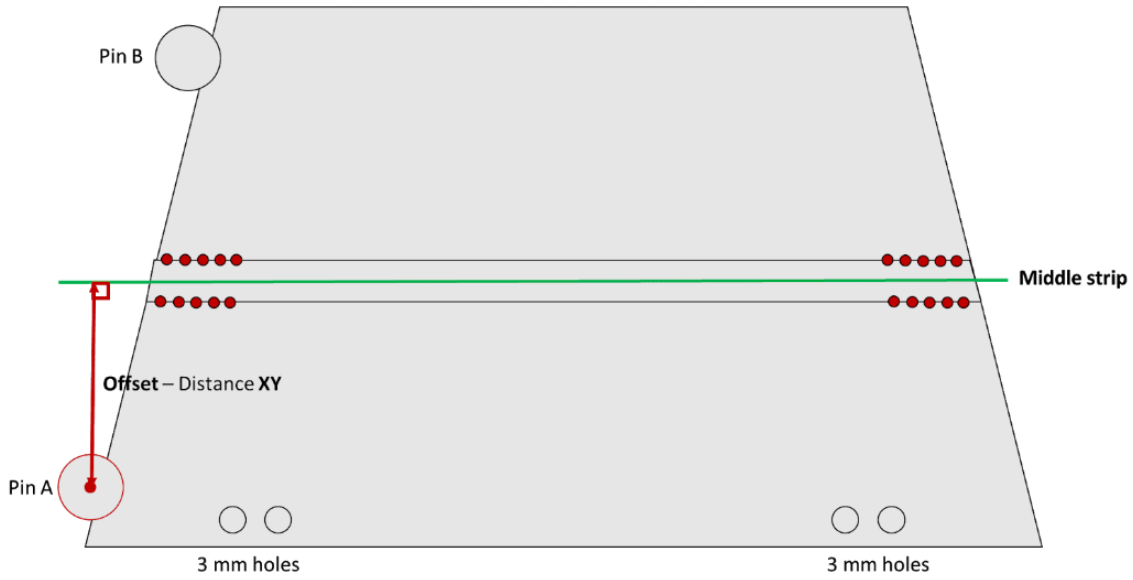

Figure 6.1: A diagram showing how the offset measurement was taken at Triangle Labs. A 24 board is depicted in this diagram, as the alignment features are on the left[3].

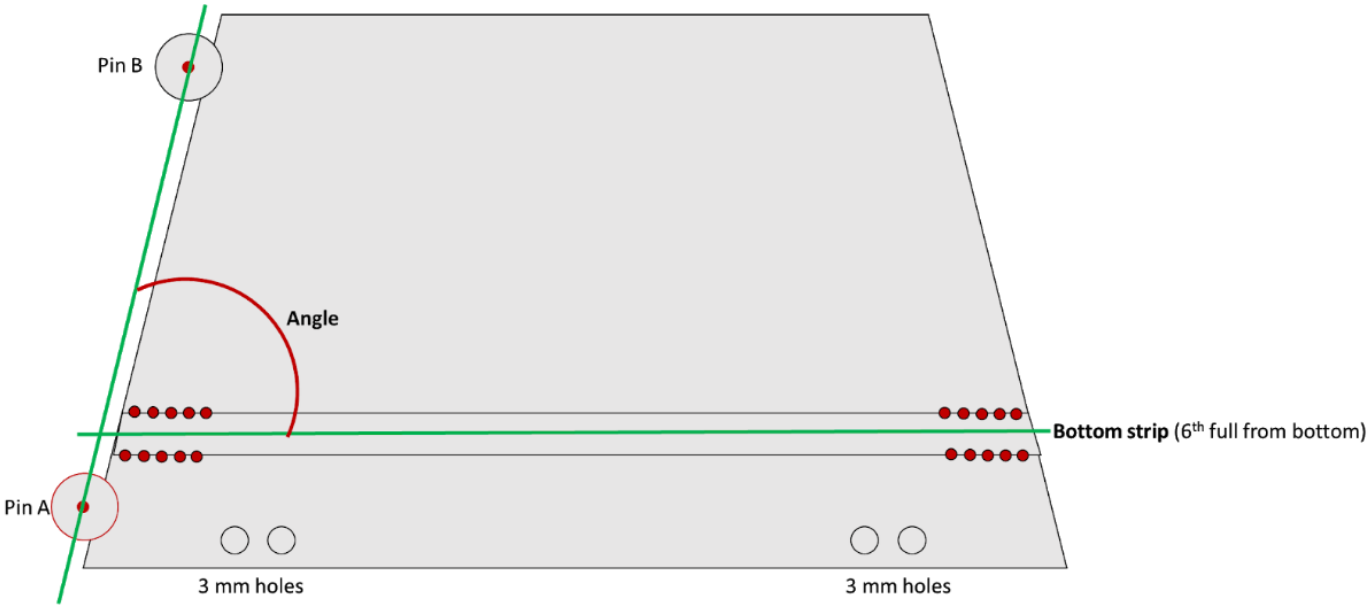

Figure 6.2: A diagram showing how the angle measurement was taken at Triangle Labs. A 24 board is depicted in this diagram, as the alignment features are on the left[3].

are defined as

$$s = \frac{d_1 + d_2}{2} - h \tag{6.1}$$

$$\Delta P = d_1 - d_2 \tag{6.2}$$

respectively, where h is the nominal value of d_1 and d_2. It is important to note that d_1 is always measured on the left and d_2 is always measured on the right, with the small end upward. This is true for both 13 and 24 boards, which have the alignment pins on opposite sides. A positive nonparallelism for a 13 board implies that the Short Strip and Long Strip are diverging as they get farther from the alignment pins. This is different for the 24 boards, where a positive nonparallelism means that the Short Strip and Long Strip are converging as they get farther from the alignment pins. Because the pins will serve as the origin of the coordinate system for the as-built transformations, it must be noted that there is a relative negative between the nonparallelism values of 13 and 24 boards.

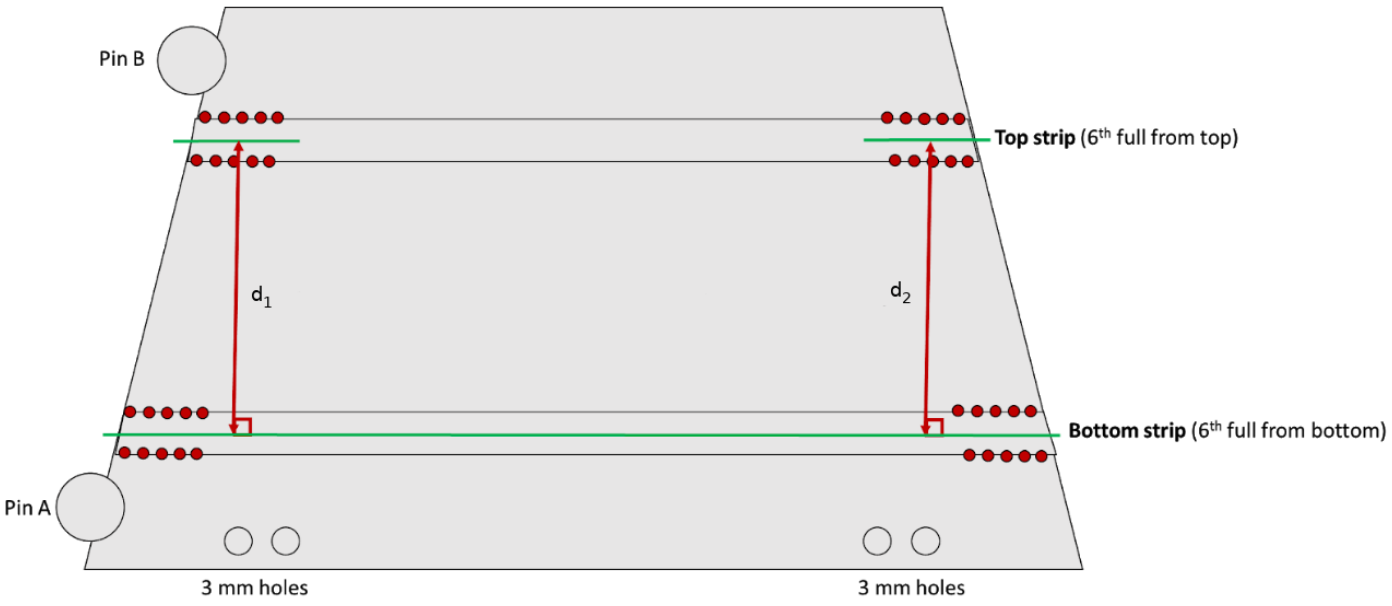

Figure 6.3: A diagram showing how the scale and nonparallelism measurements were taken at Triangle Labs. A 24 board is depicted in this diagram, as the alignment features are on the left[3].

There are a few exceptions to how these measurements were done. For example, the QL3 strip boards were measured in this fashion for the 13 boards, but the 24

boards were done differently. Instead of the angle being measured between the pin axis and the Long Strip, it was measured between the pin axis and the middle strip. Due to this difference, the transformation function derived for this specific case differs slightly from the general transformation that will be derived in Section 6.3. However, no data from QL3 boards will be analyzed in this thesis, so I will not discuss these differences further. Another exception to the measurement methodology is the QS1 boards produced in the first production run. The QS1 boards initially had their scale measured from the first strips at the long edge and short edge, as opposed to the 6th full strip from the long and short edge. Furthermore, because the QS1 boards are very long, they originally had to have their strips etched in two steps - one half of the strip pattern at a time. This means that the points used for the d_1 and d_2 measurements were etched separately, and it could remove the assumed linearity of the spreading and inclination of the strips that is inherent in the other cases. Those QS1 boards present a special case that will not be addressed in this thesis.

The cathode boards for the sTGC detectors are manufactured by three companies - Triangle Labs, Dagesh Electronics, and MDT Italia. The quality control measurements of the Dagesh and MDT boards is being carried out at the Weizmann Institute of Science in Israel. These measurements have been done in a different manner than those done at Triangle Labs, and will therefore require a different as-built transformation than the boards from Triangle Labs. This transformation is currently under development and will not be presented in this thesis.

6.3 Transformation for Triangle Labs Boards

In order to use the QC measurements of Section 6.2 to reconstruct the strip positions of the boards, a function must be established that transforms the nominal strip geometry into the as-built strip geometry. This function must use the QC measurements as parameters to determine the magnitude and direction of shifts to the nominal strip geometry. The approach used for this derivation was to study the effects of each QC measurement on the strip geometry individually and derive a transform based on that individual parameter. It should be the case that after applying an individual transform to the nominal strip geometry, if the CMM were to measure that nonconformity, it would measure the correct value. For example, if a scale of 300 μm was measured, and the scale transformation was applied to the nominal strip geometry, the value of $s = \frac{d_1+d_2}{2} - h$ as measured *after* the transformation would be 300 μm.

Once these transformations have been derived, they must be applied in an order such that they do not disturb the previous transforms. As an example, consider a board that has had the offset transformation applied to it. If the angle transformation were applied following the offset transformation, the point used for the offset measurement would have shifted, causing a different value of the offset to be measured. Thus, it is important to understand the interplay of the different measurements. These correlations are summarized below.

- The scale measurements are not affected by any of the other transformations. Nonparallelism will affect d_1 and d_2 in an equal and opposite fashion, and thus will not change the average of the two.

- The nonparallelism will only be affected by the scale transformation. Both the angle and the offset are applied equally to all strips, and because d_1 and d_2 are measured between two strips they will remain unaffected.

- The angle measurement will be affected only by the nonparallelism transformation. The nonparallelism provides an angle to the strips that could affect the measurement.

- The offset measurement is affected by all the other transformations. The scale, nonparallelism and angle all provide shifts or inclinations to the middle strip, affecting the measurement.

With these correlations in mind, the ideal order for the transformations is Scale $\rightarrow$ Nonparallelism $\rightarrow$ Angle $\rightarrow$ Offset.

Two coordinate systems will be employed in this derivation and transformation. One coordinate system will be used for the derivation of the transformation, and the second system will be a translation of the first such that the origin is the center of the alignment pin in the V-notched brass. The alignment pins are the only points on the chamber that can be referenced by ATLAS' optical alignment system, and thus are a logical choice for the final local coordinate system of the sTGC quadruplets.

In the first coordinate system, the x-axis resides on the nominal centerline of the 6th full strip from the long edge of the detector, with the positive direction going away from the alignment pins. The y-axis is perpendicular to the x-axis and intersects the Long Strip at its midpoint. The origin of this coordinate system is the midpoint of the centerline of the Long Strip. The second coordinate system has axes that are

parallel to the first system, but with the origin at the center of the alignment pin at the long edge of the board.

A diagram of all of the parameters used in the derivation of the transformation is shown in Figure 6.4. A list of the parameters is shown below.

- d_1 and d_2 are the scale and nonparallelism measurements defined in Section 6.2.1. Their nominal value is h.
- α is the distance from the y-axis to the points used to measure d_1 and d_2.
- d_{off} is the measured value of the offset as described in Section 6.2.1. It has a nominal value of f.
- θ is the measured value of the angle between the Long Strip and the axis between the center of the two alignment pins as defined in Section 6.2.1. The angle has a nominal value of ϕ.
- a is the distance from the center of the alignment pin to the y-axis of the first coordinate system. a will be used to translate from the first coordinate system to the second after the transformation has been derived.
- b is the distance from the center of the alignment pin to the x-axis of the first coordinate system. b will be used to translate from the first coordinate system to the second after the transformation has been derived.

The QC measurements are reported as the deviation from the nominal value. It is preferred to work in these deviations rather than the raw values as they are readily available from the manufacturer. The scale and nonparallelism deviations, s and ΔP were defined in Equations 6.1 and 6.2. In addition to those, the angle and offset deviations are given by

$$\delta = \theta - \phi \tag{6.3}$$

and

$$\gamma = d_{off} - f, \tag{6.4}$$

respectively.

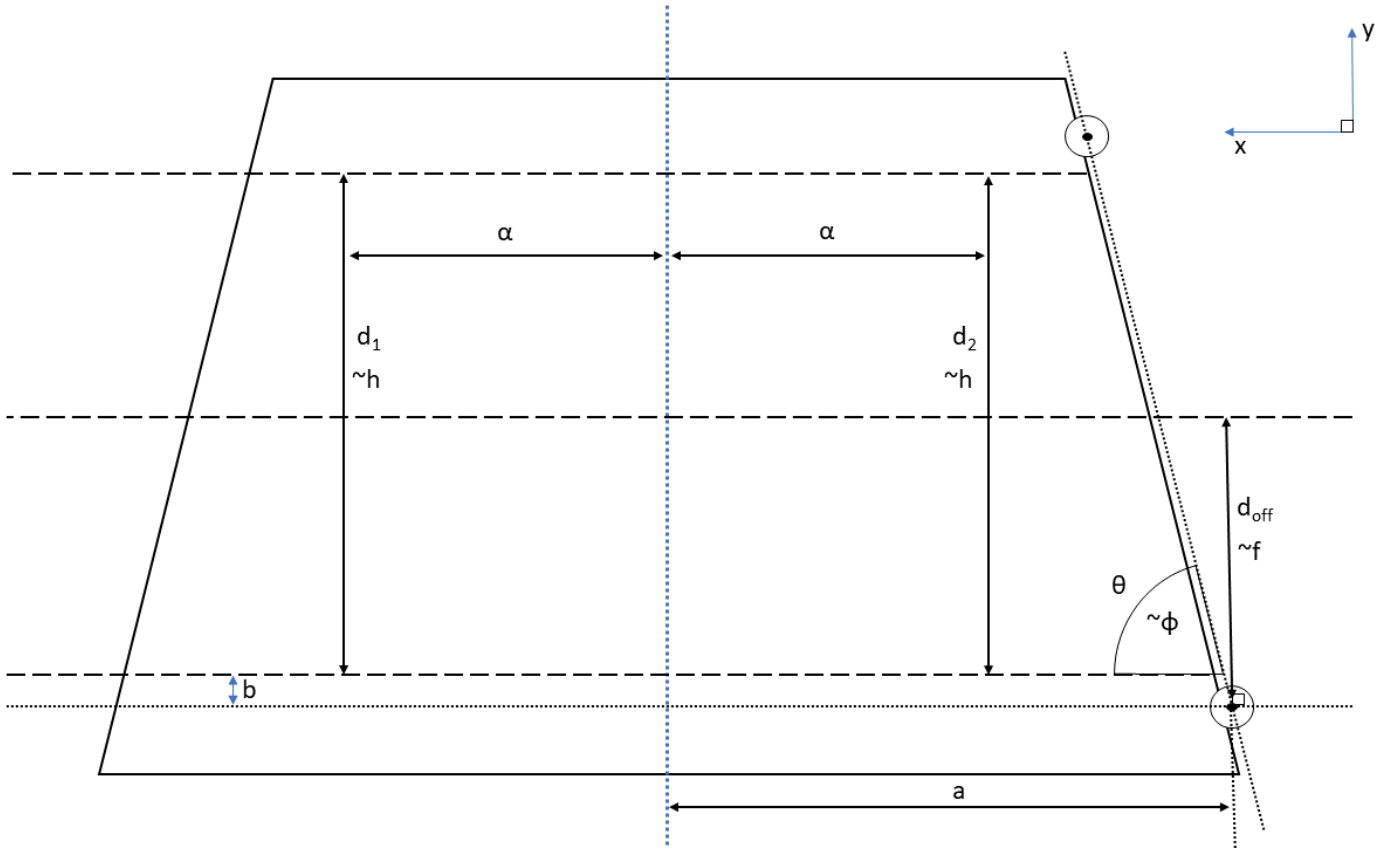

Figure 6.4: A figure labeling the different measurements and parameters employed in the transformation. A $\sim$ indicates the nominal value of a measurement. The long dashed lines are the three reference strips used by the CMM, the blue dashed line is the centerline of the board, and the small dashed black lines are the x-axis, y-axis and the pin axis. This is a diagram of a 13 board. A 24 board would have the alignment pins on the left side.

6.3.1 Derivation

This derivation will be for the case of a 13 strip board. The differences between a 13 board and a 24 board will be discussed at the end of the section. It is important to note that this derivation will take place in the coordinate system with the origin at the midpoint of the Long Strip.

The first transformation to be applied is scale. d_1 is nominally measured between the points $(\alpha, 0)$ and (α, h). Likewise, d_2 is measured between $(-\alpha, 0)$ and $(-\alpha, h)$. After the scale is applied, the y-coordinates of the two top points should increase by an amount s in order to produce the scale measurement. The transform should map $(\alpha, h) \rightarrow (\alpha, h + s)$ and (-α, h) $\rightarrow (-\alpha, h + s)$. Because the scale does not incline the Short Strip, this should apply to any x-coordinate, not just $x = \pm\alpha$. Assuming that the spreading of the strips occurs linearly between the Long and Short Strip, then the change in the y-coordinate should be linear with respect to the y-coordinate. A mapping that fits this model is

$$(x, y) \rightarrow (x, y + y \cdot \frac{s}{h}). \tag{6.5}$$

If this mapping is applied to (α, h), we see that (α, h) is mapped to $(\alpha, h + s)$, as expected.

Now that the scale has set the average of d_1 and d_2, the nonparallelism can be used to tune the difference between d_1 and d_2 and set them to their measured value. For a 13 board, a positive nonparallelism means that the Short Strip and Long Strip are diverging as they get farther from the alignment pins. A diagram of this is shown in Figure 6.5. Assuming that the Long Strip remains in its nominal position, the angle between the Short Strip and the Long Strip induced by the nonparallelism is given by

$$\beta_{max} = arctan\left(\frac{\Delta P}{2\alpha}\right). \tag{6.6}$$

The assumption that the Long Strip remains in its nominal position through the nonparallelism transformation allows the angle transform to be applied directly without needing to consider the impact of the nonparallelism on the angle measurement. Assuming that the nonparallelism scales linearly with respect to y, then it should be that the angle induced at a given y is given by

$$\beta(y) = arctan\left(\frac{y}{h} \cdot \frac{\Delta P}{2\alpha}\right), \tag{6.7}$$

where the term inside of the arctangent is the effective nonparallelism that would be measured at a strip with an initial y-coordinate of y. Evaluating $\beta(y)$ at $y = h$ yields β_{max} and $\beta(0) = 0$, which is the desired scaling.

The two points that d_1 and d_2 are measured to are (α, h) and $(-\alpha, h)$. Based on Figure 6.5, (α, h) must increase its y-coordinate by $\frac{\Delta P}{2}$ and $(-\alpha, h)$ must decrease its y-coordinate by $\frac{\Delta P}{2}$. It can be seen that $\pm\frac{\Delta P}{2} = \pm\alpha \cdot tan(\beta_{max})$. To apply this to a more general point located at (x, y), we replace α with x and β_{max} with $\beta(y)$. Thus, the resulting shift in the y-coordinate for an arbitrary point (x, y) is

$$\begin{aligned} \Delta y &= x \cdot tan\left(\beta(y)\right) \\ &= x \cdot tan\left(arctan\left(\frac{y}{h} \cdot \frac{\Delta P}{2\alpha}\right)\right) \\ &= x \cdot \frac{y}{h} \cdot \frac{\Delta P}{2\alpha}. \end{aligned} \tag{6.8}$$

The angle transformation is a simpler version of the nonparallelism, as it is applied uniformly to all of the strips on the board. A positive value of the angle parameter δ implies that the Long Strip is moving closer to the long edge of the detector as it moves away from the alignment pins. In this transformation, the angle will be applied around the y-axis such that points with an x-coordinate of zero experience no change. Figure 6.6 shows the inclination experienced by the strips. Because the angle is applied evenly to all of the strips regardless of y-coordinate, the shift induced by the angle must be solely dependent on x. Looking at Figure 6.6, it can be seen that the shift is given by

$$\Delta y = -x \cdot tan(\delta). \tag{6.9}$$

Applying the transformations for scale, nonparallelism and angle, we have that a nominal point (x, y) will be transformed according to the mapping

$$(x, y) \rightarrow \left(x, y + y \cdot \frac{s}{h} + x \cdot \frac{y}{h} \cdot \frac{\Delta P}{2\alpha} - x \cdot tan(\delta)\right). \tag{6.10}$$

The point from which the offset is nominally measured is $(-a, f - b)$. After the transformation, it should be mapped to the point $(-a, f - b + \gamma)$. Because the offset is applied uniformly to all points on the board, it can have no position dependence.

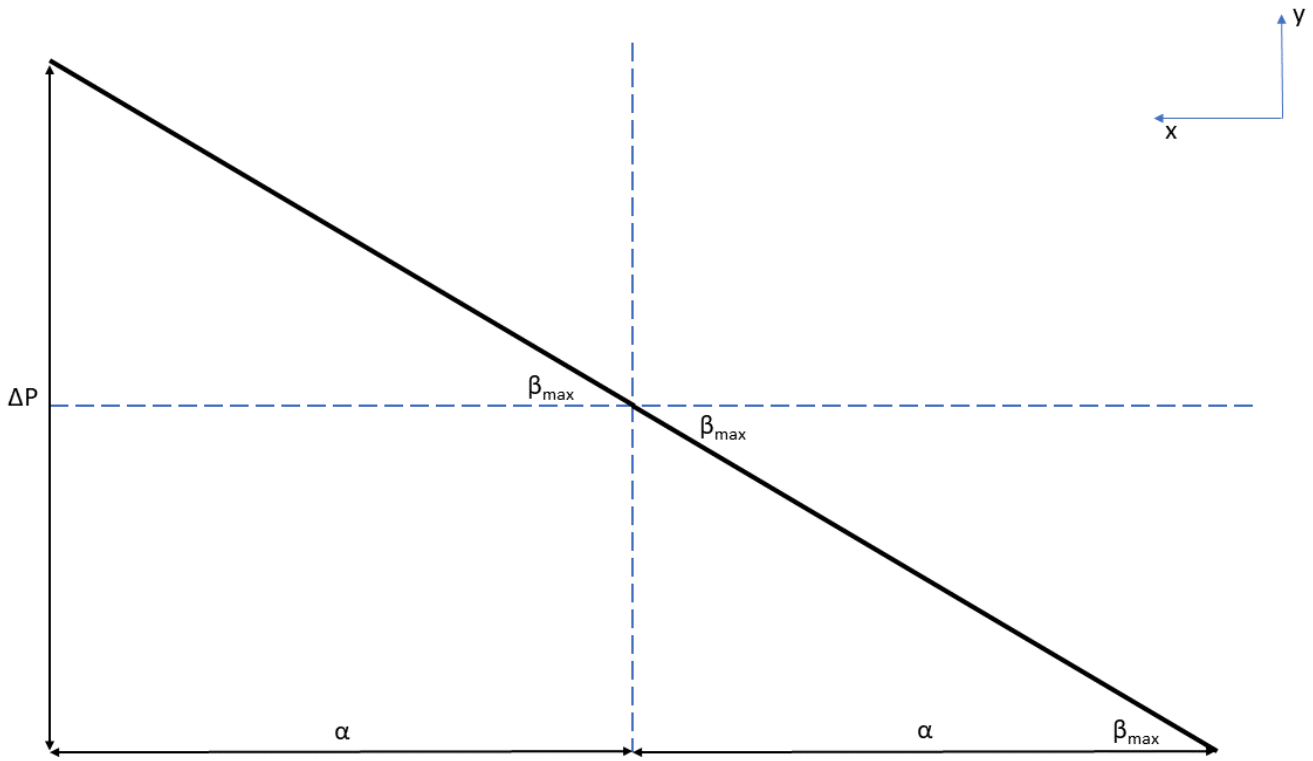

Figure 6.5: A diagram of the effects of nonparallelism on the Short Strip of a 13 board.

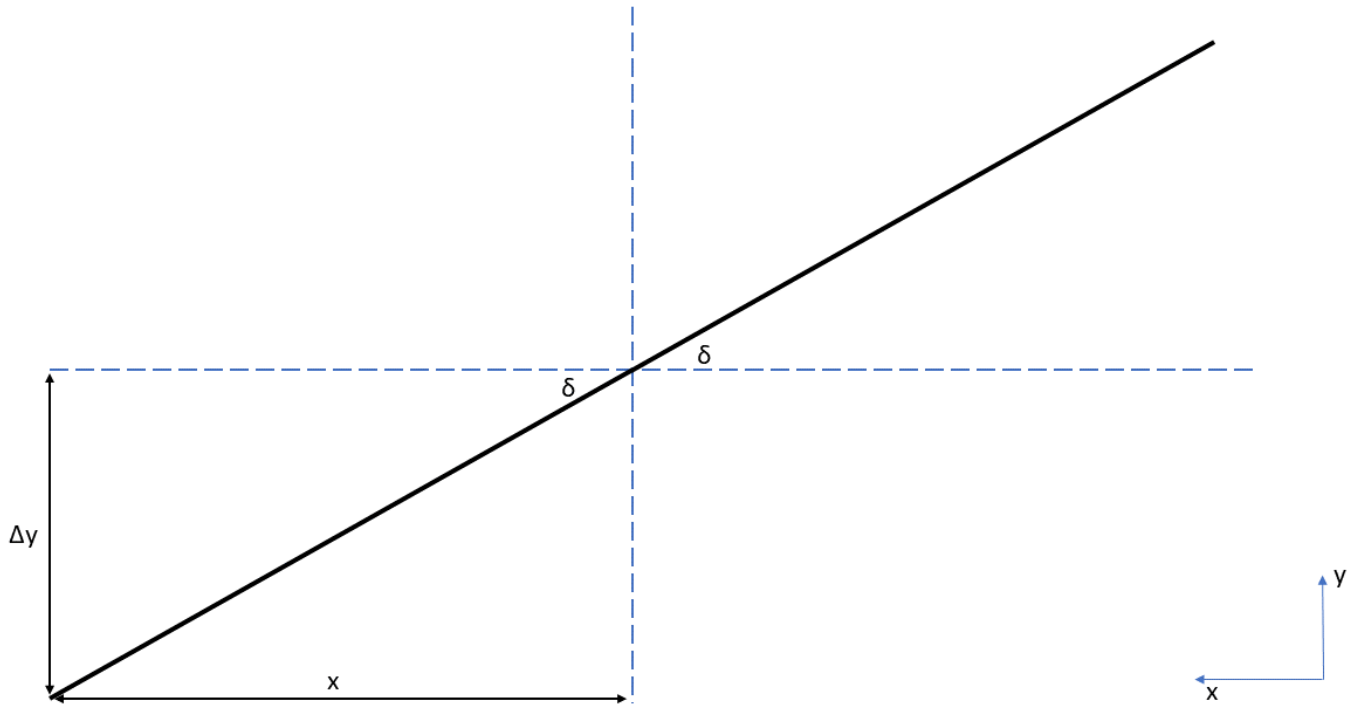

Figure 6.6: A diagram showing how the angle parameter affects the strips on a 13 board.

Thus, the offset transformation can only be done with the addition of a constant to the y-coordinate. However, the point $(-a, f-b)$ has been shifted by the three previous transformations, so it can not just be the addition of γ. If $(-a, f-b)$ is transformed with scale, nonparallelism and angle, the result is

$$(-a, f-b) = \left(-a, (f-b) + (f-b)\cdot\frac{s}{h} + a\cdot tan(\delta) - a\cdot\frac{f-b}{h}\cdot\frac{\Delta P}{2\alpha}\right). \quad (6.11)$$

After the addition of a constant for the offset transformation, the y-coordinate should be equal to $f - b + \gamma$. Let this constant be γ_{actual}. Then we have

$$f - b + \gamma = (f-b) + (f-b)\cdot\frac{s}{h} + a\cdot tan(\delta) - a\cdot\frac{f-b}{h}\cdot\frac{\Delta P}{2\alpha} + \gamma_{actual}, \quad (6.12)$$

which, when solved for γ_{actual}, reduces to

$$\gamma_{actual} = \gamma - (f-b)\frac{s}{h} - a\cdot tan(\delta) + a\cdot\frac{f-b}{h}\cdot\frac{\Delta P}{2\alpha}. \quad (6.13)$$

Therefore, the full transformation of a point (x, y) on a 13 board due to scale, nonparallelism, angle and offset nonconformities in the first coordinate system is given by

$$(x, y) \rightarrow \left(x, y + y\cdot\frac{s}{h} + x\cdot\frac{y}{h}\cdot\frac{\Delta P}{2\alpha} - x\cdot tan(\delta) + \gamma_{actual}\right), \quad (6.14)$$

where γ_{actual} is defined in Equation 6.13. In order to translate this transformation into the second coordinate system centered on the alignment pin, every instance of x in the terms generated by the transform should be replaced by $x - a$, and every instance of y should be replaced by $y - b$. The final transformation is given by

$$(x, y) \rightarrow \left(x, y + (y-b)\cdot\frac{s}{h} + (x-a)\cdot\frac{y-b}{h}\cdot\frac{\Delta P}{2\alpha} - (x-a)\cdot tan(\delta) + \gamma_{actual}\right). \quad (6.15)$$

As mentioned in Section 6.2.1, the d_1 and d_2 measurements are always taken on the left and right of the board, respectively, leading to a relative negative between the

nonparallelism of 13 and 24 boards. This causes a change in sign of all terms involving the nonparallelism in Equations 6.13, 6.14 and 6.15 when applying the transform to 24 boards.

6.4 Microscope Alignment Pictures

Canadian doublets and quadruplets are produced at Carleton University. Following assembly, pictures of the strips are taken at the four corners of the detector as a way to measure the misalignment between layers. This serves two purposes - ensuring that no major misalignments are introduced by the construction process, and serving as a comparison to the as-built strip alignment predictions. Misalignments can be introduced by the construction process in several ways. For example, if the alignment pins were not perfectly vertical and were tilted in the y-direction, an offset could be introduced during the gluing of doublets. If the V-notch pin was vertical but the other pin was slightly tilted, this would introduce a relative rotation between the two layers. By comparing the as-built predictions to the microscope measurements, we hope to be able to identify any potential systematic misalignments that have been introduced by the construction process. Microscope pictures have also been taken at other construction sites, but those pictures will not be analyzed in this thesis.

6.4.1 Carleton Picture Procedure

The alignment pictures taken at Carleton are taken with the chamber lying flat on a granite table. For doublets, the even numbered layers were placed face down on the granite table with the odd numbered layers facing up. The microscope took pictures of the doublets from the side of the detector, as shown in Figure 6.7, and measured the misalignment of the top layer relative to the bottom layer. Pictures were taken at the four corners of the detector at a specific strip number. The strip number was counted starting from the short edge of the trapezoid and included the half strip in the numbering.

The measurements produced by the team at Carleton were made using an image analysis script developed there. It works by having the user first identify the edges of the strips of the top layer, and then do the same for the bottom layer. Then the script draws a best fit line through the two sets of points. It then identifies the midpoints of the strips and the gaps between the strips on both the top and bottom layers. From

there, the script draws lines normal to the bottom layer from each of those midpoints up to the top layer. These lines are shown in red in Figure 6.7. It also draws lines from the midpoints of the bottom layer to the midpoints of the top layer as a reference, as the midpoints should be aligned. Those lines are shown in blue. Finally, it measures the misalignments between strips by calculating the distance between the midpoint of the top layer and the point where the normal intersects the best fit line. The final misalignment value output by the software is an average of the misalignment measurements. A positive value of the misalignment indicates that the top layer has shifted to the right relative to the bottom layer, and a negative value corresponds to a shift to the left. Because the sign convention of the pictures is defined through left and right, pictures taken on the alignment side have a different sign convention than pictures taken on the non-alignment side[3].

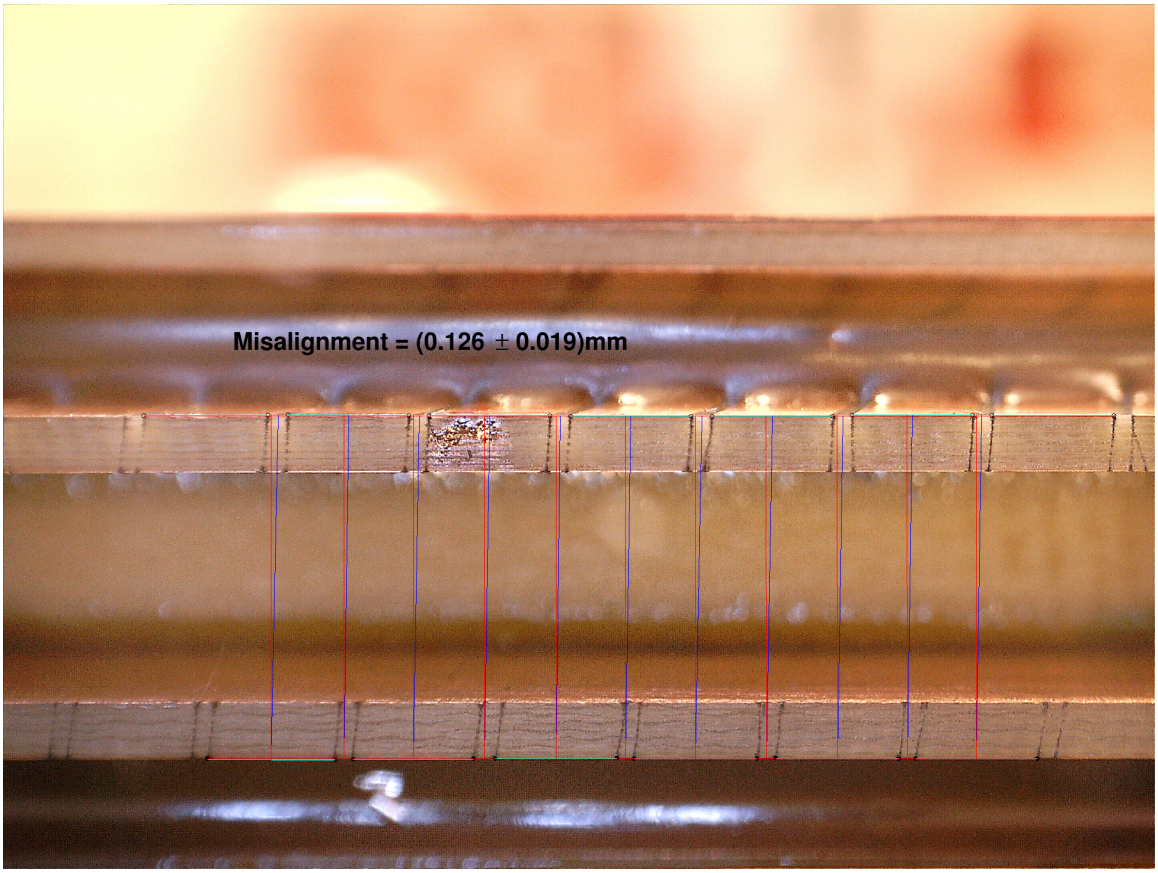

Figure 6.7: A sample microscope picture used to measure the misalignment on a QS3 doublet.

[3]The alignment side of the detector is the edge of the detector that has the brass alignment inserts, and the non-alignment side is the edge of the detector opposite the alignment side.

6.5 The Transformation Script

In order to compare the predictions of the as-built transformation to the microscope alignment measurements, a Python script that constructs perfectly built cathode boards and then transforms them according to their quality control measurements has been developed. The script is written in an object-oriented fashion with a nested class structure. The classes are:

1. Strip. Each Strip object is a collection of points in the xy-plane. These points mark the centerline of a strip on a cathode board. A Strip object is given a y-coordinate upon creation, and it inherits all of the QC measurements and nominal values from the board on which it is created. The Strip class has a function to apply the transformation to its own points.

2. Board. The Board class is a collection of strip objects of differing length that create a model of the cathode board. Each Board is created with parameters specific to which type of board it is (QS1, QL1, etc.). It is also given QC measurements and the nominal values of its board type. It has a function to display the geometry of the board, which prints out the strips that the board is composed of, and another function to apply the transform to all of the strips. The board also has a function entitled "`get_measurements`," which calculates the distances between the points in a way identical to the CMM and returns those values. This is used to ensure that the QC values are replicated by the program following the transformation.

3. Doublet. A Doublet object is a pair of Board objects - an even layer and an odd layer. It has attributes for the QC measurements and nominal measurements of both boards. It has two functions to compute the misalignment between the endpoints of strips.

4. Quadruplet. A Quadruplet object is a pair of Doublet objects. It contains all of the QC measurements for each of its four boards, as well as the nominal values. Like the Doublet class, the Quadruplet class also has functions to compute the misalignment between strip layers.

The functions used to compute the strip misalignments between layers were designed to compare to the microscope pictures done at Carleton University. The functions retrieve the endpoints of strips with the same number in two layers of a doublet

or quadruplet and calculate the distance between these points. For the Doublet class, because the strip patterns of adjacent layers are offset by 1.6 mm[4], the function subtracts off their nominal offset before returning the misalignment. For a quadruplet, the function can align any pair of layers. If the function aligns an odd layer with an even layer, it subtracts off the nominal offset like the Doublet class does. If it's aligning layers 1 and 3 or 2 and 4, it does not subtract off the nominal value as they should nominally be aligned. There are two alignment functions for each class. One of them is for the side with the alignment features, while the other is for the side without those features. This is due to the difference in sign convention of the microscope pictures between the two sides.

The script requires user input to run. It begins by prompting the user to input a board type, such as QS3 or QL2. From this input the script determines the nominal values of the boards that will be analyzed. The user is then prompted for the four digit serial number of the boards that they wish to align, as each board has unique values of the QC measurements. The script uses the serial numbers of the board to obtain the individual QC measurements from the Triangle Labs QC database on Google Sheets. Finally, the script requires the user to input which layers should be aligned. It then calculates and prints the misalignment values between the two requested layers at each of the four corners. If the user wants to look at locations other than the corners, the strip number that is being aligned can be changed within the code. The results of the comparison between the as-built predictions and the microscope measurements will be presented in Chapter 8.

[4]This is equal to half the strip pitch, as described in Section 6.1.

Chapter 7

Cosmic Ray Analysis

As part of the quality assurance process for the sTGC detectors, each sTGC quadruplet undergoes testing with cosmic rays. Cosmic rays are an abundant and useful tool for performing diagnostic tests of chambers. In particular, the sTGC cosmic ray tests aim to measure the gain uniformity, efficiency, and spatial resolution of each chamber before it is installed into the New Small Wheel. The data taken with cosmic rays can also be used as a powerful tool to measure the relative alignment between the layers of the chamber.

The cosmic ray tests for quadruplets constructed in Canada are done at McGill University in Montréal. This chapter will give an overview of the theory of cosmic rays before discussing the cosmic ray testing procedure carried out at McGill. The chapter will conclude with an outline of the analysis tools developed by the team at McGill as they pertain to measuring misalignments, with an explanation of how those misalignments can be compared to the as-built misalignment predictions described in Chapter 6.

7.1 Cosmic Ray Theory

Cosmic rays consist of numerous different particle types originating from outside of Earth. They are primarily composed initially of high-energy protons and atomic nuclei. Almost all of the cosmic rays arriving at earth come in the form of protons and neutrons. Most of these particles originate from outside the solar system, although some come from the sun, especially from events such as solar flares. These particles arriving from outer space are known as primary cosmic rays [29].

The muons used in cosmic ray tests are produced inside of Earth's atmosphere. Known as secondary cosmic rays, these muons come about from the interactions of primary cosmic rays with particles in Earth's atmosphere. As the primary cosmic rays collide with the atmosphere, they can initiate showers of secondary particles. These include hadrons such as pions and kaons. The muons that reach Earth's surface originate from the decays of these hadrons. This process is shown in Figure 7.1 [30]. Muons produced through these processes are the most abundant charged cosmic particles at sea level. Cosmic muons are on average produced at an altitude of 15 km above sea level at an energy of 6 GeV, making them minimum ionizing particles. As the muons descend through the atmosphere, they tend to lose approximately 2 GeV of energy to ionization. Though the muon has a mean lifetime of 2.2 μs, the Lorentz factor of a muon with a momentum of 6 GeV is approximately 57. Because of this dilation, these muons are easily able to reach the surface before decaying [31].

7.2 McGill Cosmic Ray Test Stand

The cosmic ray test stand at McGill University was designed to collect data with production sTGC quadruplets built in Canada. The testing facility consists of a gas system, a station for the electronics necessary to operate the detector, and a cosmic ray hodoscope. The gas system is capable of providing either an n-pentane/CO_2 gas mixture or pure CO_2 to the modules on the test stand. Though the gas system is capable of operating 10 separate gas lines, the layers of an sTGC quadruplet can be connected together to form one system serviced by a single gas line. A full set of Version 2.1 pFEBs and sFEBs installed on the detector were powered by a CAEN A2519 8-channel low voltage power supply housed in the electronics station. The readout system also employs the same miniDAQ system that was described in Chapter 3. The high voltage to each layer is supplied by a CAEN A1535D multi-channel HV power supply with each layer of the quadruplet connected to its own channel. The current of each power supply is continually monitored, with the HV power supply set to automatically shut down if the current on an individual channel exceeds 1 μA [32].

The cosmic ray hodoscope used to test quadruplets at McGill consists of two planes of scintillators, one on the top of the hodoscope and one at the bottom, with four platforms between the two planes designed to house quadruplets. The two scintillator planes consist of plastic scintillators with an optical wave guide affixed to each end. These wave guides direct the light produced through scintillation to photomultiplier

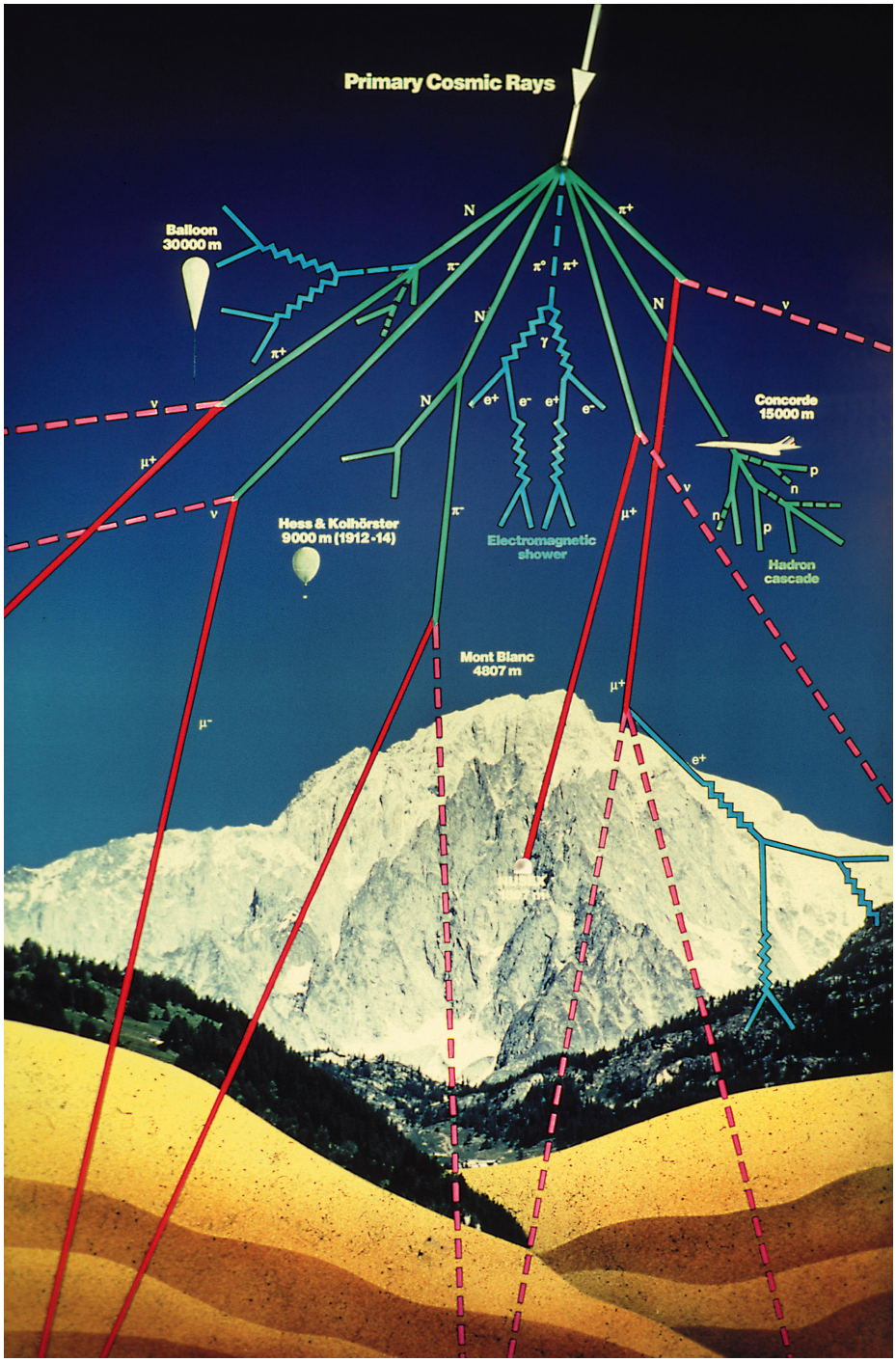

Figure 7.1: A diagram showing the production of secondary cosmic rays in Earth's atmosphere [30].

tubes connected to the end of the wave guide. Held at a negative voltage of 1.6 kV, the photomultiplier tubes amplify the signal of the scintillation light and pass it on to the hodoscope trigger system. The hodoscope trigger searches for coincidences between the top and bottom planes of scintillators. When such a coincidence is detected, the trigger system sends a signal to the readout electronics of the sTGC, which record any activity measured by the detector. The layout of the hodoscope can be seen in Figure 7.2 [32].

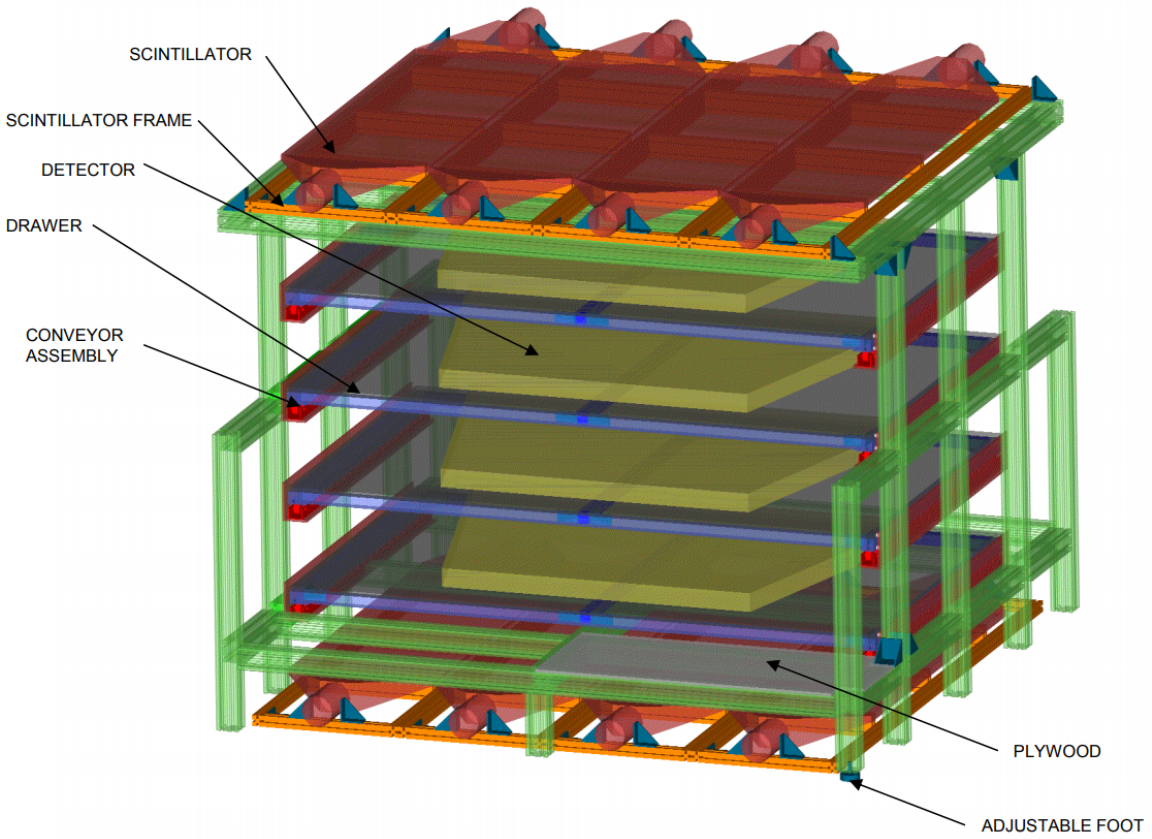

Figure 7.2: A diagram of the cosmic ray hodoscope used for testing at McGill University [32].

7.3 Misalignment Measurements from Cosmic Rays

The data collected at the cosmic ray test stand at McGill can be analyzed in order to deduce information about the relative alignment of layers in an sTGC quadruplet. Each sTGC spends two days on the cosmic test stand. On the first day, the detector

collects data at 2.9 kV and 3.1 kV for two hours each. This provides approximately one million events per run. The same tests are repeated on the second day. Because the detector is fully instrumented with readout electronics, the positions of particles can be measured through the combination of signals from the pads, wires and strips. Each of these position measurements is recorded with an associated error. This data analysis was done by Benoit Lefebvre and the rest of the sTGC group at McGill University [32].

The reconstructed positions can be used to extract the alignment information about the detector. Because the hodoscope does not provide fine position information of each event, there is no well defined external reference to which we can align the detector. This makes it necessary to designate a pair of layers of the detector as reference layers. The other layers of the detector can then be aligned relative to these two reference layers. The reference layers are assumed to be correctly aligned, such that the positions that each reference layer measured can be used to construct a track. The measured y-position of a particle is obtained by fitting a Gaussian to the strip PDO signals deposited by the particle. The centroid of this Gaussian is the measured y-position. A track line is drawn through the points measured by the two reference layers and extended to go through the two remaining layers. This line is used to predict exactly where the particle should have passed through the other layers, assuming that the reference layers are correctly aligned. The predicted position of the particle is then compared to the position measured by the remaining layers. The difference between the measured position and the predicted position is known as the residual. This method is depicted in Figure 7.3. In Figure 7.3, the reference layers are layers 1 and 2, and the residuals are labeled Δ_3 and Δ_4. To determine the misalignment between layers, the residuals are calculated for each event and are placed into a histogram corresponding to their layer. These histograms are then fitted with a Gaussian distribution. The mean value of the Gaussian provides the misalignment of the detector, and the width of the Gaussian gives an estimation of the error. A more detailed description of this method can be found in Benoit Lefebvre's PhD dissertation [32]. Iterating over every pair of reference layers provides a more complete picture of the misalignment of the quadruplet.

Due to the large number of events recorded in cosmic ray testing, the analysis is able to divide the detector into regions and measure the misalignment in each region by only analyzing tracks that pass through that particular region. By measuring the misalignment in different regions of the detector, a better picture of the global

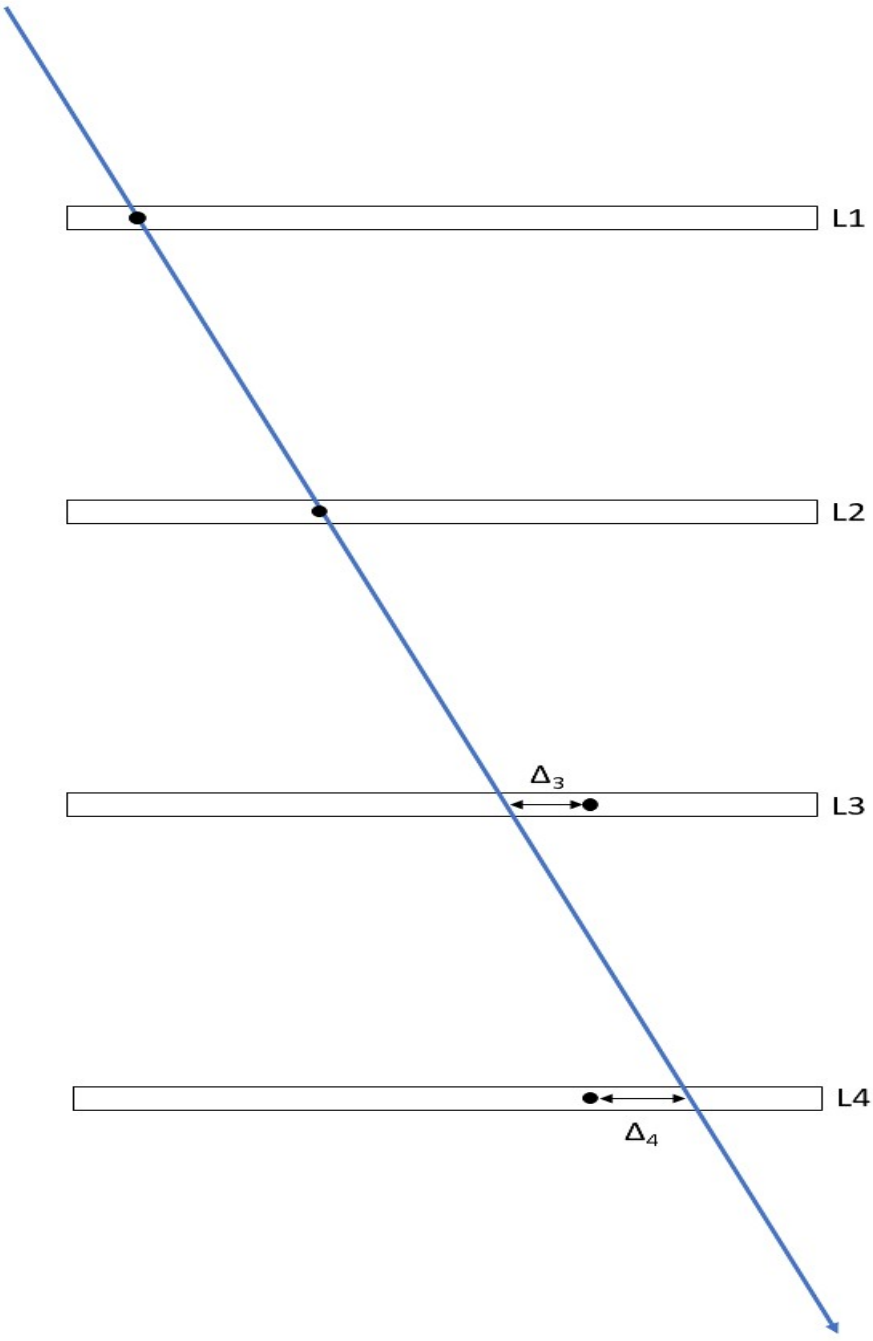

Figure 7.3: A diagram explaining the method of using reference layers and residuals to deduce the relative alignment of a detector. In this diagram, layers 1 and 2 are being used as reference layers, and layers 3 and 4 are being aligned relative to 1 and 2. The residuals are labeled Δ_3 and Δ_4. The black dots denote the position measured by the detector.

variations can be obtained. This is necessary for the cosmic misalignment data to be compared to the as-built misalignment predictions described in Chapter 6.

The code framework described in Chapter 6 has been extended to allow for a direct comparison to the measurements made using cosmic rays. The transformation function derived in Chapter 6 is implemented in a continuous function such that the transformation is decoupled from the Strip objects. The code works by generating vertical "tracks" with an array of points in the xy-plane. To construct a track, two reference layers are designated by the user. Then, for each point (x, y) in the array, the transformed positions of (x, y) are generated for the reference layers based upon their QC measurements. A line is then drawn between these transformed points, and is used to predict where the "measured" position should be on the other layers. The "measured" position for the layers being aligned is generated by passing the point (x, y) through the transformation function, using the QC measurements of the corresponding layers. This "measured" position is then compared against the position predicted by the track, and a residual is calculated. Like in the cosmic analysis, the detector is subdivided into regions, with each region having a corresponding array of points. An example of this subdivision is shown in Figure 8.5. The residuals calculated for each region of the detector are then averaged to provide an overall misalignment measurement for that bin. An average is used rather than forming a histogram out of the residuals because the continuity of the transform ensures that local variations within the region are small.

Chapter 8

Alignment Results

At the time of this writing, 12 QS3 quadruplets have been constructed in Canada. Each doublet has had microscope pictures taken to measure the relative strip alignment between layers, as described in Chapter 6. Furthermore, each complete quadruplet has undergone the cosmic ray testing described in Chapter 7. The measurements from these two methods provide a data set against which the transformation derived in Chapter 6 can be tested.

This chapter will present a comparison of the misalignments measured with the cosmic rays and the microscope pictures to the as-built predictions of the calculator described in Chapters 6 and 7. The first section of the chapter will detail the methods of comparing the predictions to the measurements. Following this, the results of the comparison between the as-built predictions and the microscope measurements will be presented, followed by the results of the cosmic ray comparison. A discussion of the uncertainties associated with each method will conclude the chapter.

8.1 Analysis Methods

The first comparison of this chapter is between the microscope pictures taken at Carleton University and the as-built predictions derived from the quality control information. The procedure for taking the pictures and extracting the alignment information from them is outlined in Section 6.4.1, and a sample image is shown in Figure 6.7. It is important to recall that the microscope analysis measures the misalignment of the top doublet layer relative to the bottom doublet layer, and that a shift of the top layer to the right of the picture defines a positive value for the

misalignment. Because right points to the short edge for pictures of the alignment side and to the long edge for pictures of the non-alignment side, there is a relative sign difference between measurements taken on opposite edges of the detector. For example, if the boards of a doublet were manufactured and constructed perfectly except for the top layer board having an offset of 100 μm, a picture on the alignment side of the doublet would measure a misalignment of 100 μm and a picture on the non-alignment side would measure a misalignment of -100 μm.

Microscope pictures are taken at the four corners of the doublet. Point 1 is on the alignment side of the detector near the short edge. Point 2 is near the long edge on the alignment side. Points 3 and 4 are on the non-alignment side, with point 3 near the long edge and point 4 near the short edge. A diagram showing the layout of the four points is shown in Figure 8.1. The as-built calculator produces misalignment measurements of the strips at each of these points. The values that it predicts have been corrected for the sign convention described in the previous paragraph. In total, 23 doublets have had their misalignment measured.

Figure 8.1: A diagram showing the layout of the points for the microscope pictures.

Plots of the predicted values versus the measured values were fit in three ways. The first method fit the data linearly, with free parameters for both the slope and intercept of the fit. The second fit was a proportional fit, with the slope free but the intercept of the fit fixed at zero. If the predictions were to perfectly match the

microscope measurements, the resulting fit would be a line with a slope of one and an intercept of zero, so the final fit calculated the χ^2 value of the data set relative to that line. Each of these fits was done for the data from each corner as well as for the cumulative data set. All of the plots have the as-built predictions on the y-axis and the measured values on the x-axis.

The second comparison of this chapter is between the as-built predictions and the cosmic ray alignment measurements done at McGill University. The methods used for measuring the alignment with cosmic rays and for predicting the misalignments with the as-built calculator were described in Section 7.3. Using this method of reference layers and alignment layers, 12 sets of misalignment data can be created from a single quadruplet by iterating over all possible combinations of the reference layers. A single quadruplet was used for this analysis, QS3.P.6, because the data for the other quadruplets tested at McGill is not available at the time of this writing.

The fits of the predicted values versus the cosmic alignment measurements were done in a similar fashion to the microscope comparison. Because the corners of the detector are where the extrema of the misalignments are expected to occur, this analysis focused on comparing the predicted values to the measured values at the corners. The linear, proportional and χ^2 fits that were done for the microscope analysis were also done for the cosmic comparison. These fits were done for the data at each of the individual corners, as well as for the cumulative data set.

8.2 Microscope Alignment Results

The results of the microscope alignment comparisons are summarized in Tables 8.1, 8.2 and 8.3. Table 8.2 shows the linear fit parameters for each point as well as for the complete data set, and Figure 8.2 shows the linear fit for the full data set. The χ^2 value of the fit is also listed in the table, along with the number of degrees of freedom (n.d.f.). This provides a measure of the overall quality of the fit to the data. It can be seen in Table 8.1 that the slopes are consistent with the expected slope of one, but none of the intercepts are consistent with the expected intercept of zero. Also, the relatively large χ^2 / n.d.f values for Point 3, Point 4 and the total data set indicate that even though the slope is consistent with one, the data deviates from the line by a large amount. This can be confirmed by inspecting Figure 8.2, where the data deviates from the best fit line significantly.

The results for the proportional fit are summarized in Table 8.2, and the propor-

	Point 1	Point 2	Point 3	Point 4	Total
Slope	1.0 ± .14	1.0 ± .13	1.0 ± .16	1.0 ± .15	1.06 ± .06
Intercept (μm)	35 ± 14	44 ± 13	-154 ± 17	-72 ± 16	-22 ± 7
χ^2 / n.d.f.	26.84 / 21	12.84 / 21	39.53 / 21	40.34 / 21	274.3 / 90

Table 8.1: A table of the linear fit parameters of the microscope comparison.

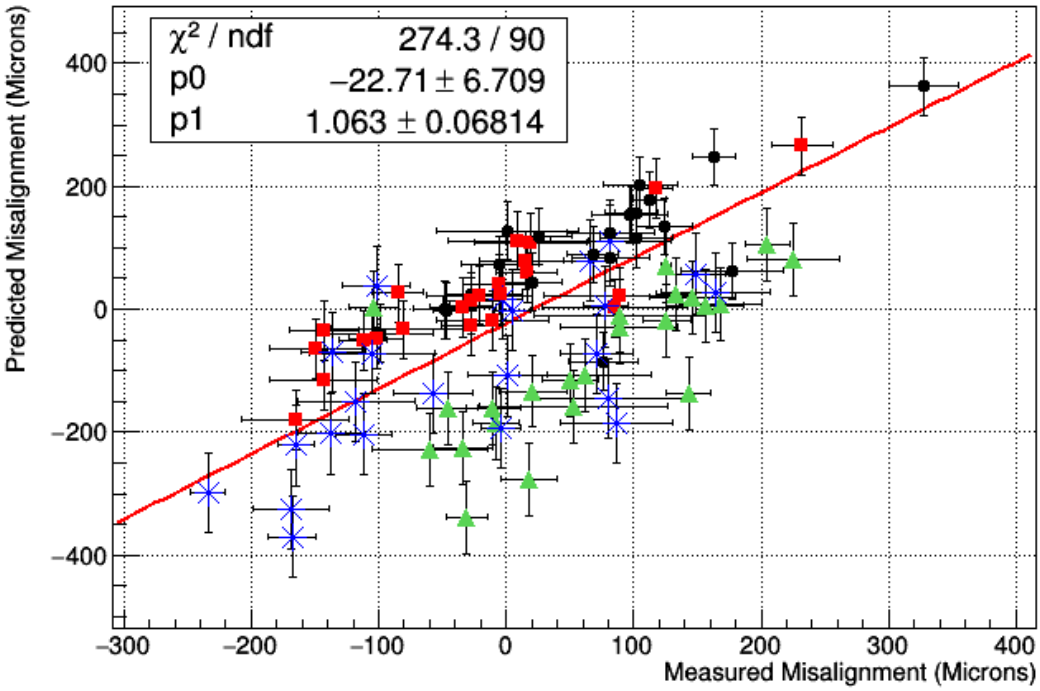

Figure 8.2: A linear fit of the misalignment predictions vs. the misalignments measured by the microscope. The data from point 1 is shown by the black circles. Point 2 is represented by the red squares, point 3 is shown by the green triangles, and point 4 is shown by the blue Xs.

tional fit for the total data set is shown in Figure 8.3. When fit with a proportional function, the slopes for Point 1, Point 3 and Point 4 are no longer consistent with a slope of one. This is a result of forcing the large intercept values from Table 8.1 to be zero. For the proportional fit, all of the χ^2 / n.d.f values are greater than one, meaning that the quality of the fit has declined. The fit on Figure 8.3 shows that although the proportional fit is consistent with a slope of one, the data is widely distributed about the line. This is reflected in the fact that the χ^2 / n.d.f. value is greater than 3 for the cumulative data set.

	Point 1	Point 2	Point 3	Point 4	Total
Slope	1.24 ± .11	0.9 ± .13	0.29 ± .15	1.3 ± .15	1.01 ± .06
χ^2 / n.d.f.	32.11 / 22	26.03 / 22	137.6 / 22	58.5 / 22	286 / 91

Table 8.2: A table of the proportional fit parameters of the microscope comparison, where the intercept of the fit has been forced to be zero.

The χ^2 values of the data when compared to a line of slope one and intercept zero are listed in Table 8.3. A plot of the data with this line overlaid is shown in Figure 8.4. The results of this comparison are mostly like the results from the proportional fit. The χ^2 values remain relatively close, except for Point 3, which increased by about 1 because the slope from the proportional fit was far off from one. Similarly to the proportional fit, Figure 8.4 shows that the data is widely distributed about the expected values.

	Point 1	Point 2	Point 3	Point 4	Total
χ^2 / n.d.f.	37.11 / 23	26.69 / 23	159.2 / 23	63.09 / 23	286.1 / 92

Table 8.3: A table of the χ^2 values of the fit to a line with a slope of one and an intercept of zero.

Overall, the predictions correlate well to the misalignment values measured by the microscope. This is especially true for the linear fit, where all of the slopes are consistent with one. However, the relatively large χ^2 values seen in Table 8.1 show that even with the intercept as a free parameter, the data is widely distributed about the best fit lines. The fact that the slopes are consistent with one but the intercepts are far from zero indicates that there is potentially a misalignment that is being systematically introduced by the construction method. This could arise from the gluing process, when the sTGC layers are pressed against the precision alignment

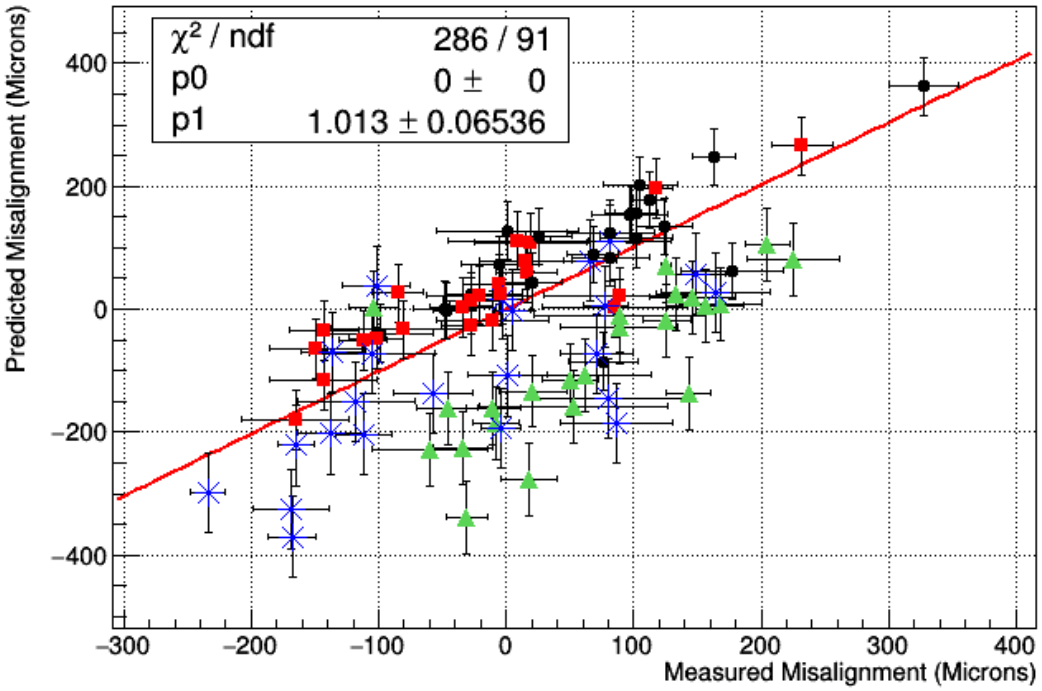

Figure 8.3: A proportional fit of the misalignment predictions vs. the misalignments measured by the microscope. The data from point 1 is shown by the black circles. Point 2 is represented by the red squares, point 3 is shown by the green triangles, and point 4 is shown by the blue Xs.

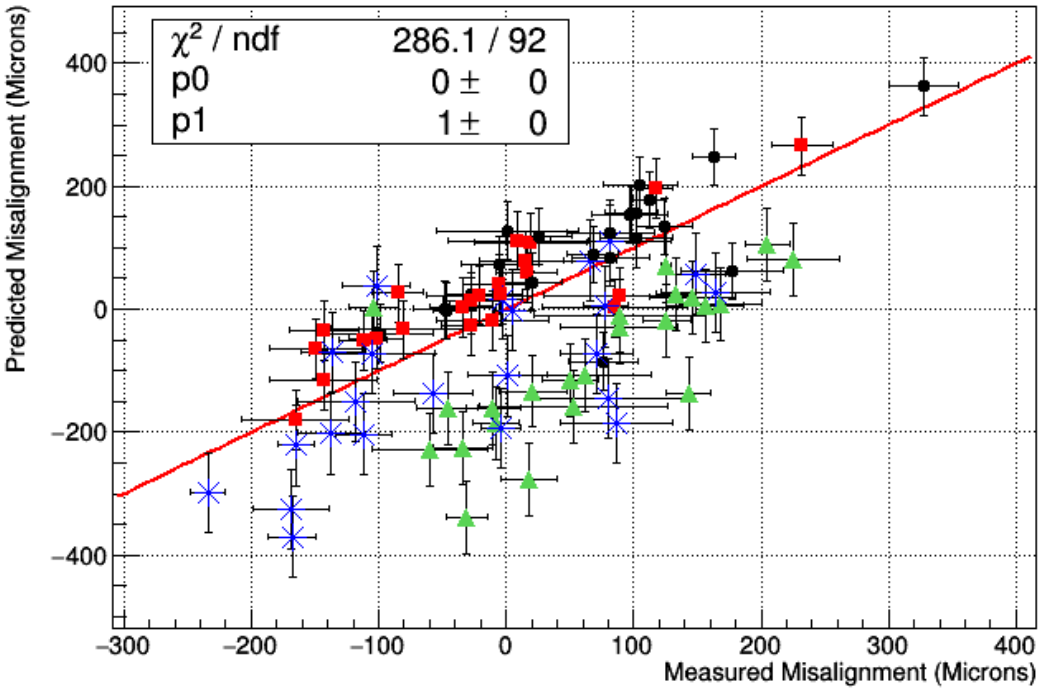

Figure 8.4: A plot of the misalignment predictions vs. the measured misalignment compared to a line of slope 1.0 and intercept 0. The data from point 1 is shown by the black circles. Point 2 is represented by the red squares, point 3 is shown by the green triangles, and point 4 is shown by the blue Xs.

pins. It is possible that the pins are not precisely vertical on the gluing table. If the pins were at an angle relative to the table, it could introduce offsets or rotations into the doublet assembly process. For example, if the pin at the long edge of the detector was vertical and the pin at the short edge was tilted in the x-direction, a rotation could be introduced that twists the top layer counter-clockwise relative to the bottom layer. A rotation such as this would cause small effects on the alignment side of the detector but large effects on the non-alignment side because the rotation has propagated over a large distance. However, the inconsistencies in the data do not appear to arise from a single phenomenon such as a rotation or translation. The wide distribution about the best fit line points to potentially larger errors than were accounted for in both the predictions and the microscope measurements.

8.3 Cosmic Alignment Results

Tables 8.4, 8.5 and 8.6 summarize the results of the cosmic ray misalignment comparison. A sample misalignment map produced by the as-built calculator is shown in Figure 8.5. The coordinate system for the misalignment map is the same coordinate system used in the transformation, with the center of the alignment pin serving as the origin (top-left corner). The misalignment map demonstrates the continuous behavior of the transform, where local variations in the misalignment are small.

Table 8.4 shows the results of the linear fits to the data, and Figure 8.6 shows the linear fit of the complete data set. Of the five slopes, only the slope of Point 1 is consistent with one. The slope of Point 4 has the greatest deviation from one, but each other point has a slope that is relatively close to the expected value. Each of the intercepts for the individual points is consistent with the expected intercept of zero, but the intercept for the total fit is not consistent with zero. Apart from Point 3, the low χ^2 values show that the data tends to be distributed relatively tightly around the best fit line. This is seen in Figure 8.6, which exhibits a much narrower distribution of the data than is seen in Figure 8.2.

	Point 1	Point 2	Point 3	Point 4	Total
Slope	1.0 ± .1	0.84 ± .05	0.83 ± .1	1.6 ± .3	0.90 ± .04
Intercept (μm)	-10 ± 17	-6 ± 17	-17 ± 23	-2 ± 26	-16 ± 10
χ^2 / n.d.f.	8.005 / 10	8.316 / 10	23.7 / 10	3.262 / 10	56.2 / 46

Table 8.4: A table of the linear fit parameters of the cosmic ray comparison.

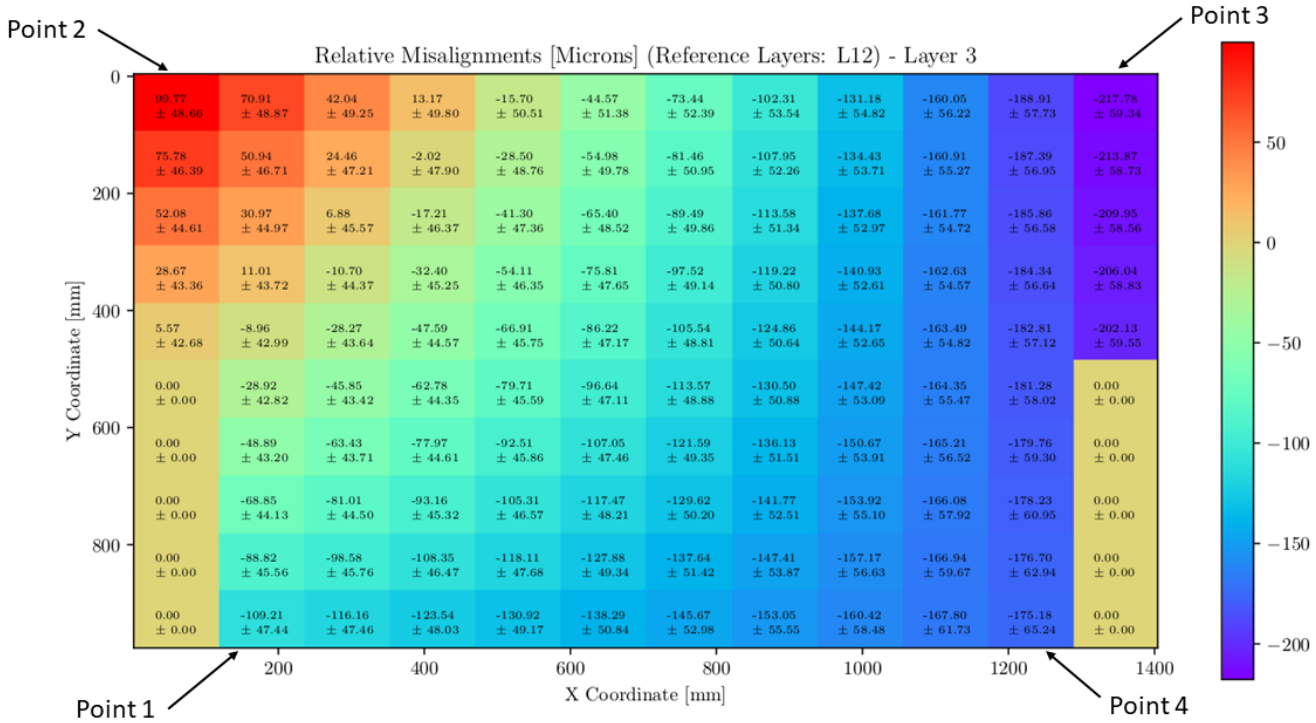

Figure 8.5: A plot of the misalignment predictions as a function of position for layer 3 of QS3.P.6. Layers 1 and 2 were used as the reference layers.

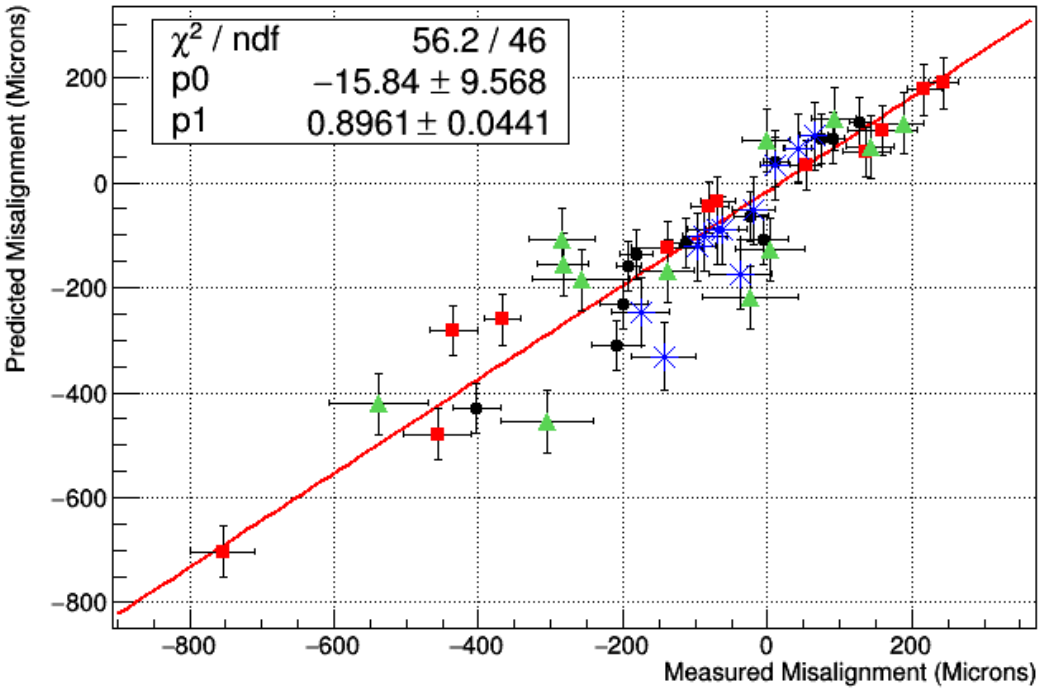

Figure 8.6: A linear fit of the misalignment predictions vs. the misalignments measured with cosmic rays. The data from point 1 is shown by the black circles. Point 2 is represented by the red squares, point 3 is shown by the green triangles, and point 4 is shown by the blue Xs.

Table 8.5 summarizes the results of the proportional fits to the data. The slopes remain relatively unchanged from those of the linear fit. This is expected, because each of the intercepts for the individual points was consistent with zero. Thus, forcing their value to be zero does not have a major impact on the fit. As a result, the χ^2 values of the fits are also largely similar, with small increases being seen for each fit. The slope of Point 1 is the only slope consistent with the expected value of one, but the slope of the cumulative fit is within two uncertainties of one, as is the slope of Point 3.

	Point 1	Point 2	Point 3	Point 4	Total
Slope	1.07 ± .09	0.84 ± .05	0.86 ± .09	1.7 ± .3	0.93 ± .04
χ^2 / n.d.f.	8.325 / 11	8.443 / 11	24.22 / 11	3.268 / 11	58.91 / 47

Table 8.5: A table of the proportional fit parameters of the cosmic ray comparison.

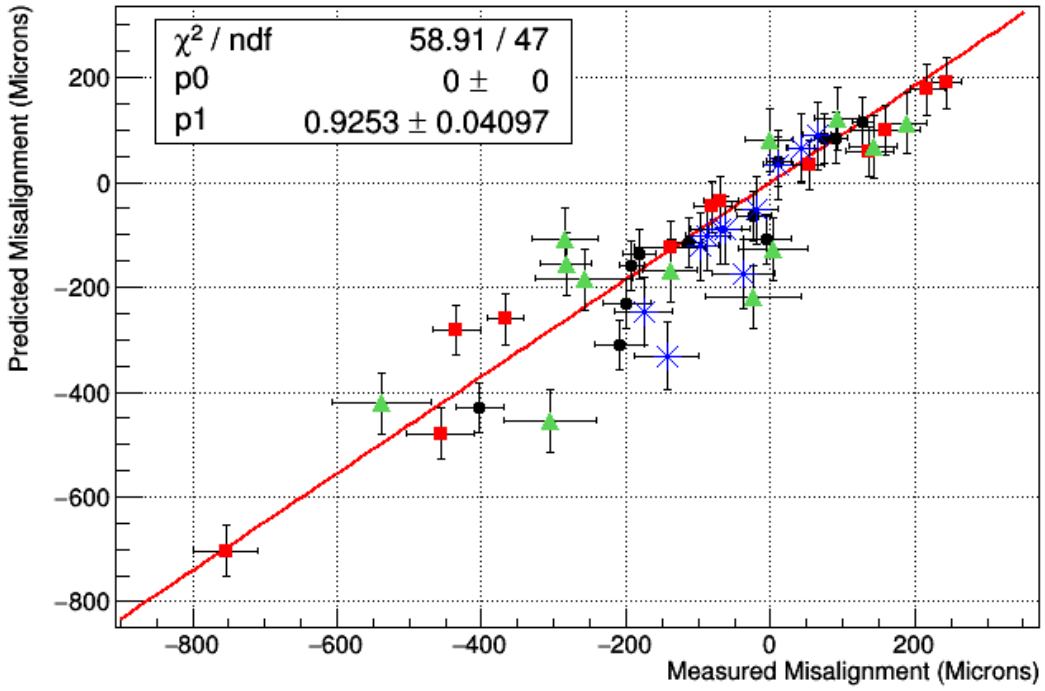

Figure 8.7: A proportional fit of the misalignment predictions vs. the misalignments measured with cosmic rays. The data from point 1 is shown by the black circles. Point 2 is represented by the red squares, point 3 is shown by the green triangles, and point 4 is shown by the blue Xs.

Table 8.6 shows the χ^2 values of the data when compared to a line of slope one and intercept zero. The full data set with the ideal fit superimposed is shown in Figure 8.8. The χ^2 values for each of the points are close to one overall, with Point 3 being the only data set that exceeds a χ^2 / n.d.f of 2. The χ^2 / n.d.f value of 1.3 for the cumulative data set is indicative that a line with a slope of one and an intercept of zero is an appropriate model for this comparison.

	Point 1	Point 2	Point 3	Point 4	Total
χ^2 / n.d.f.	8.94 / 12	16.35 / 12	26.12 / 12	10.65 / 12	62.06 / 48

Table 8.6: A table of the χ^2 values of the fit to a line with a slope of one and an intercept of zero.

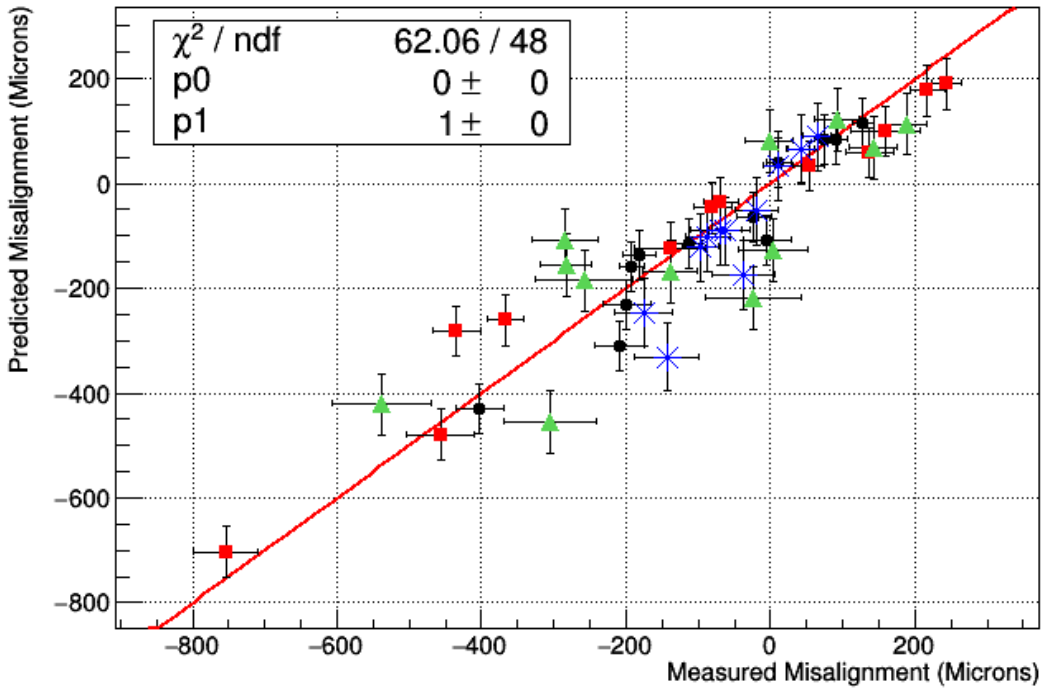

Figure 8.8: A plot of the misalignment predictions vs. the measured misalignment compared to a line of slope 1.0 and intercept 0. The data from point 1 is shown by the black circles. Point 2 is represented by the red squares, point 3 is shown by the green triangles, and point 4 is shown by the blue Xs.

The results of these three fits show that the predictions correlate very well with the measurements. The distribution about the best fit lines for all three cases is

much narrower than what was observed in the microscope alignment measurements. The linear fit intercepts being consistent with zero contradicts the data observed in the microscope pictures, where none of the intercepts were consistent with zero. Intercepts of zero point towards there being no translation or rotation of layers relative to each other. This initial analysis of the cosmic ray measurements indicates that the construction process is not producing large amounts of misalignment. It can be seen in Figure 8.8 that the data tends to lie below the fit line, indicating that the predictions tend to be below the value measured by the cosmic rays. This is also observed in the data from the microscope measurements, seen in Figure 8.4. It is possible that some aspect of the transform is systematically causing the predicted misalignment values to be lower than the measured values. If this behavior persists after analyzing the cosmic data from more quadruplets, it will be investigated further.

8.4 Uncertainties

Each of the three methods for measuring the misalignment between layers has its own uncertainty. For the microscope pictures, the uncertainty arises from the usage of the image software and the resolution of the image. The image analysis software requires the user to identify the edges of the strips with the mouse of the computer. Due to the resolution of the image and the inherent instability and imprecision of the input device, the points are unlikely to be representative of the true positions of the strip edges. A line of best fit is drawn through the top and bottom strip layers. These best fit lines have an associated uncertainty from the fitting process, that is then propagated to the measurements when the perpendicular lines are drawn from the top to the bottom layers. A more detailed explanation of the measurement process is in Section 6.4.1. The uncertainties from this method are included in the analysis in Section 8.2. Although the best fit lines have an uncertainty, the points indicated by the mouse do not have an uncertainty. If these points were to have an associated uncertainty, it would propagate through the process and lead to larger values of the uncertainty for the microscope measurements.

For the cosmic ray misalignment measurements, the uncertainty originates from the intrinsic position resolution of the detector. The y-positions of the passing particles are determined by fitting the PDO distribution deposited on the strips with a Gaussian distribution. The centroid of this Gaussian provides the y-position of the passing particle. The positions measured on the two reference layers are used to

predict the position that should be measured on the two alignment layers. The predicted position is then subtracted from the measured position on the alignment layers to obtain the residuals. These residuals are placed into a histogram which is fit with a Gaussian. The centroid of this Gaussian provides the misalignment measurement, and the width of the Gaussian provides the uncertainty on the misalignment. These are the uncertainties that are included on the cosmic ray measurements in Section 8.3. A more detailed discussion of these uncertainties can be found in Benoit Lefebvre's PhD dissertation [32].

The uncertainties of the as-built misalignment predictions are caused by the precision of the CMM used to do the quality control measurements of the cathode boards. At best, the CMM has a resolution of 20 μm. Because the best fit lines of the strips are generated from a collection of 20 points as described in Section 6.2.1, each best fit line will have uncertainties involved in the equation of the line. However, the raw data of the 20 points used to form the best fit lines has never been available to analyze, so an analysis to determine their uncertainties was not pursued. Thus, to get an estimate on the minimum uncertainty of each measurement, a precision of 20 μm was assumed for each point used in a measurement. Because the scale, nonparallelism and offset are all composed of the sum or difference of points, this 20 μm uncertainty was multiplied by $\sqrt{2}$ to get an uncertainty of approximately 30 μm for the scale, offset and nonparallelism measurements. Because the angle is measured between the centerline of the bottom strip and the axis between the two pins, it is necessary to have an idea of the uncertainties on these lines. This can't be accomplished without the raw data, so a flat value of 0.001° was assumed as the uncertainty on the angle measurement. This is equal to one tenth of the construction tolerance for the angle parameter.

These uncertainties for the quality control measurements were propagated through the transform function derived in Chapter 6 to provide uncertainty values for the as-built strip positions. For the microscope comparison, a difference was taken between two strip positions. The uncertainties in the strip endpoint position were propagated through the difference to produce the error bars that were used for the predicted misalignment values in Section 8.2. These same position uncertainties were used to calculate an uncertainty on the slope of the tracks that were used for the cosmic ray comparison. The uncertainty of the slope was propagated to the predicted positions of the track used to calculate the residual. Combined with the uncertainty on the position observed by the alignment layer, this yielded the uncertainties that were used

as the error bars for the predicted values in Section 8.3.

The uncertainties listed in the tables in Sections 8.2 and 8.3 are the result of fitting the data with the corresponding linear and proportional functions. These fits, calculated in ROOT, account for the error bars when determining the best fit parameters and their uncertainties. It is important to note that the uncertainties for the predicted values are a lower bound. The 20 μm position resolution of the CMM is an optimal value. The optimal performance of the CMM is dependent on factors such as the temperature of the measurement room and the range over which the CMM is operating. It is realistic that the resolution is greater than 20 μm. It is also likely that the microscope and cosmic ray measurements were not taken at the same temperature that the boards were measured at. The thermal expansion of the boards would cause the measurements for the scale, offset and nonparallelism to all change by a small amount, further affecting the accuracy of the predicted values.

Chapter 9

Conclusions

ATLAS is one of two general purpose particle detectors operating at CERN's Large Hadron Collider. After discovering the Higgs boson in 2012, the collaboration has pursued a wide physics program focused on searches for particles that exist beyond the Standard Model as well as precision measurements of phenomena within the Standard Model. Following the 2018 - 2021 shutdown of the LHC, the collider will produce more collisions inside of ATLAS than ever before. ATLAS must undergo extensive upgrades to cope with the increased number of collisions per bunch crossing.

The primary upgrades of Long Shutdown 2 are the New Small Wheels (NSWs), a replacement of the Small Wheel stations of the muon spectrometer's end-caps. The primary trigger chambers of the NSW are small-strip Thin Gap Chambers (sTGCs), a type of multiwire proportional chamber that is an improvement of the current ATLAS TGC technology. An sTGC detector consists of two cathode planes, one segmented into strips and the other segmented into pads, with a plane of anode wires strung between them.

Before the NSWs are implemented into ATLAS, it is important to fully understand the properties and behavior of the sTGC detectors. In order to characterize the sTGCs, a series of test beams were conducted in the fall of 2018 with the goal of measuring the efficiency, multiplicity and response of the chambers. The experimental setup of the test beams was described in Chapter 4 and the results were presented and summarized in Chapter 5. Two layers of the detector performed excellently, with the efficiency of the pads and wires meeting the performance requirements of the NSW at the operating voltages of 3.0 and 3.1 kV. The pads exhibited low multiplicity at all operating voltages, which is the desired result, as high multiplicity causes issues in localizing the regions of interest in the trigger system. The wires also exhibited

low overall multiplicity. The peak detector output profile also matched the expected Landau distribution for both the pads and the wires.

The analysis of the test beam data could be improved upon in a handful of ways. Though the wires data from layers 3 and 4 was not analyzed due to the firmware issue described in Section 5.4, the raw binary data does exist for those layers. If the raw data decoder was altered to decode this data, it could be analyzed to give a measurement of the efficiency and multiplicity of layers 3 and 4. An extension of the analysis that searches for correlations between high multiplicity events between layers would be helpful in understanding the cause of these events.

Since the test beam, extensive work has been done to reduce the noise of the detector electronics. In particular, a grounding scheme that involves connecting the grounding backplanes of the pad adapter boards to the strip cathodes and the grounding backplanes of the strip adapter boards to the pad cathodes has been developed. This grounding is in addition to the connection of the adapter boards to their corresponding cathodes. This grounding scheme has been retroactively added to every quadruplet to reduce their noise levels. On the electronics end, optimization studies have been done for the π-network capacitance values. These studies have helped to determine which capacitance values should be used for the different sized pads of the detector to attenuate the signals by the proper amount.

In order for the NSW to perform to its specifications, it is necessary to be able to precisely locate the detector elements of the sTGC chambers. To do this, ATLAS uses an optical alignment system to monitor the movement of NSW wedges. It is able to accurately determine the locations of the brass alignment features of the wedge as a function of time. From this information, the positions of the internal readout electrodes can be reconstructed. However, due to manufacturing imperfections, the strips of the sTGC detectors are not at their nominal positions and their as-built positions must be reconstructed. This reconstruction is accomplished through a transformation of each individual strip board based on quality control measurements taken at the manufacturer and the construction sites. These quality control measurements and the derivation of the transformation were detailed in Chapter 6.

To test this transformation, a Python calculator that predicts the as-built strip positions was developed. The calculator is capable of predicting the relative misalignment between layers. The predictions of this calculator were compared to misalignment measurements made with microscope pictures taken at Carleton University. The results of this comparison were presented in Chapter 8. The microscope data

comparison shows that the predictions correlate very well with the measured values of the misalignment, but the wide distribution of the data suggests that there are improvements to be made to the predictions of the software and to the microscope measurement process.

The as-built predictions were also compared against misalignment measurements obtained through cosmic ray tests of a Canadian quadruplet. The cosmic ray data taking and analysis process were detailed in Chapter 7, and the results of the comparison were presented in Chapter 8. The as-built predictions correlate very well with the measured values, and the cumulative data set from the cosmic ray measurements is consistent with a line with a slope of one and an intercept of zero. The as-built predictions do tend to be a small amount below the measured values. If this behavior persists through the analysis of more quadruplets, it will be investigated.

The alignment analysis that has been presented can be improved and expanded upon. A more extensive study of the uncertainties of the CMM measurements would help to provide a better understanding of the limitations of the as-built predictions. If possible, it would be ideal to obtain the raw CMM data from Triangle Labs so a better understanding of the uncertainties on the best fit lines could be developed and implemented into the analysis. For the microscope measurements, uncertainties that arise from the user input into the image processing software should be accounted for. Reanalyzing the data with updated uncertainties could provide more insight into the trends observed in this analysis. For improving the cosmic ray alignment comparison, the analysis should incorporate the results from more quadruplets. This data has been collected by the team at McGill and the data should be available for analysis soon. The initial results are promising, but an analysis of a larger collection of data should help to make errors in the transformation or the construction process more apparent. The alignment calculator used for the as-built predictions has been distributed to all of the sTGC construction sites for their use. It will be used to compare to microscope misalignment measurements similar to the measurements made at Carleton. More microscope alignment data will soon be available to analyze to assess the accuracy of the transformation and the construction process.

Currently, an alignment test is being developed at CERN that uses a collimated x-ray gun to measure the misalignments between the layers. This test will be an incredibly powerful tool, as it is being carried out on wedges that have the precision alignment platforms mounted onto them, as well as the precision alignment pins. This will allow for the strips to be located relative to the alignment pins, instead of relative

to other strips. The as-built alignment calculator will be expanded such that its predictions can be tested thoroughly against these x-ray measurements. Ultimately, the combination of the x-ray measurements and the as-built predictions will make it possible to perform the precision alignment necessary for the New Small Wheel.

Bibliography

[1] CERN: Our History. https://home.cern/about/who-we-are/our-history. Accessed: 2019-5-09.

[2] CERN: Our Research. https://home.cern/about/what-we-do/our-research. Accessed: 2019-5-09.

[3] The Accelerator Complex. https://home.cern/science/accelerators/accelerator-complex. Accessed: 2019-5-09.

[4] Pulling Together: Superconducting Electromagnets. https://home.cern/science/engineering/pulling-together-superconducting-electromagnets. Accessed: 2019-5-09.

[5] Esma Mobs. The CERN Accelerator Complex. https://cds.cern.ch/record/2197559, Jul 2016.

[6] The ATLAS Collaboration. The ATLAS experiment at the CERN large hadron collider. *Journal of Instrumentation*, 3(08):S08003, Aug 2008.

[7] Joao Pequenao and Paul Schaffner. How ATLAS Detects Particles: Diagram of Particle Paths in the Detector. https://cds.cern.ch/record/1505342, Jan 2013.

[8] Matthias Schott and Monica Dunford. Review of single vector boson production in pp collisions at $\sqrt{s} = 7$ TeV. Review of single vector boson production in pp collisions at $\sqrt{s} = 7$ TeV. *Eur. Phys. J. C*, 74(arXiv:1405.1160):60 p, May 2014. Comments: 60 pages, 64 figures, For Eur. Phys. J. C.

[9] Alessandro La Rosa. The ATLAS Insertable B-Layer: from construction to operation. *JINST*, 11(12):C12036, 2016.

[10] Ana Maria Henriques Correia. The ATLAS Tile Calorimeter. Technical Report ATL-TILECAL-PROC-2015-002, CERN, Geneva, Mar 2015.

[11] Henric Wilkens and the ATLAS LArg Collaboration. The ATLAS liquid argon calorimeter: An overview. *Journal of Physics: Conference Series*, 160:012043, apr 2009.

[12] A Artamonov, D Bailey, G Belanger, M Cadabeschi, T Y Chen, V Epshteyn, P Gorbounov, K K Joo, M Khakzad, V Khovanskiy, P Krieger, P Loch, J Mayer, E Neuheimer, F G Oakham, M O'Neill, R S Orr, M Qi, J Rutherfoord, A Savine, M Schram, P Shatalov, L Shaver, M Shupe, G Stairs, V Strickland, D Tompkins, I Tsukerman, and K Vincent. The ATLAS forward calorimeter. *Journal of Instrumentation*, 3(02):P02010, February 2008.

[13] ATLAS Magnet System Diagram. http://www.quantumdiaries.org/wp-content/uploads/2011/05/exp-magnets.png. Accessed: 2019-5-23.

[14] *ATLAS Muon Spectrometer: Technical Design Report*. Technical Design Report ATLAS. CERN, Geneva, 1997.

[15] T Kawamoto, S Vlachos, L Pontecorvo, J Dubbert, G Mikenberg, P Iengo, C Dallapiccola, C Amelung, L Levinson, R Richter, and D Lellouch. New Small Wheel Technical Design Report. Technical Report CERN-LHCC-2013-006. ATLAS-TDR-020, Jun 2013. ATLAS New Small Wheel Technical Design Report.

[16] The ATLAS Collaboration. Performance of the ATLAS Trigger System in 2015. *Eur. Phys. J.*, C77(5):317, 2017.

[17] W Buttinger. The ATLAS Level-1 Trigger System. Technical Report ATL-DAQ-PROC-2012-024, CERN, Geneva, Jun 2012.

[18] Aranzazu Ruiz-Martinez and the ATLAS Collaboration. The Run-2 ATLAS Trigger System. Technical Report ATL-DAQ-PROC-2016-003, CERN, Geneva, Feb 2016.

[19] Juan Cristóbal Rivera Vergara. Cosmic ray tests for the qs1 module of the new small wheel in the atlas experiment -and- prospects on the search for heavy vector triplet bosons in the leptonic decay channels with the atlas experiment at the hl-lhc, 2018.

[20] J Chapman, T Dai, E Diehl, H Feng, L Guan, G Mikenberg, V Smakhtin, J M Yu, B Zhou, J Zhu, and Z Zhao. Simulation for ATLAS nSW Thin Gap Chambers. *PoS*, EPS-HEP2013:093. 4 p, 2014.

[21] Benjamin Pasmantirer. Quadruplet Outer Small Pivot. https://edms5.cern.ch/cdd/plsql/c4w.display_details?cookie=2211101&p_drob_id=1100132&p_version=**. Accessed: 2019-5-09.

[22] Canada sTGC Collaboration. *sTGC Assembly Manual*, April 2018.

[23] Verena Martinez Outschoorn. Frontend and Backend Electronics for the ATLAS New Small Wheel Upgrade. Nov 2016.

[24] Panagiotis Gkountoumis. Level-1 Data Driver Card of the ATLAS New Small Wheel upgrade. Technical Report ATL-MUON-PROC-2015-019, CERN, Geneva, Nov 2015.

[25] Xilinx Kintex-7 FPGA KC705 Evaluation Kit. https://www.xilinx.com/products/boards-and-kits/ek-k7-kc705-g.html#overview. Accessed: 2019-5-22.

[26] Introduction to the use of the H8 beam. http://sba.web.cern.ch/sba/BeamsAndAreas/h8/H8manual.pdf. Accessed: 2019-5-13.

[27] Roberto Guida. GIF++: A new CERN Irradiation Facility to test large-area detectors for the HL-LHC program. *PoS*, ICHEP2016:260, 2016.

[28] About ROOT. https://root.cern.ch/about-root. Accessed: 2019-5-23.

[29] Peter K.F. Grieder. *Cosmic Rays at Earth*. Elsevier, Amsterdam, 2001.

[30] High energy cosmic rays striking atoms at the top of the atmosphere give the rise to showers of particles striking the Earth's surface. http://cds.cern.ch/record/40407, May 1999.

[31] M. Tanabashi et al. Review of particle physics. *Phys. Rev. D*, 98:030001, Aug 2018.

[32] Benoit Lefebvre. *Characterization studies of small-strip Thin Gap Chambers for the ATLAS Upgrade*. PhD thesis, McGill University, Aug 2018.